



2  
2006



This is to certify that the  
thesis entitled

An Experimental Study of Microwave Plasma-Enhanced  
Combustion

presented by

Chandra Lynn Romel

has been accepted towards fulfillment  
of the requirements for the

M.S. degree in Mechanical Engineering

Major Professor's Signature

May 11, 2006

Date

**PLACE IN RETURN BOX** to remove this checkout from your record.  
**TO AVOID FINES** return on or before date due.  
**MAY BE RECALLED** with earlier due date if requested.

<b>DATE DUE</b>	<b>DATE DUE</b>	<b>DATE DUE</b>

**AN EXPERIMENTAL STUDY OF MICROWAVE PLASMA-ENHANCED  
COMBUSTION**

**By**

**Chandra Lynn Romel**

**A THESIS**

**Submitted to  
Michigan State University  
in partial fulfillment of the requirements  
for the degree of**

**MASTER OF SCIENCE**

**Department of Mechanical Engineering**

**2006**

## **ABSTRACT**

### **AN EXPERIMENTAL STUDY OF MICROWAVE PLASMA-ENHANCED COMBUSTION**

**By**

**Chandra Lynn Romel**

Advantages of a hybrid flame, created by microwave power, include more efficient and stable combustion and a more concentrated, higher temperature flame/discharge, potentially useful for material synthesis, material cutting and welding, and various surface treatments. A compact torch has been designed and experimentally evaluated while operating in both plasma-only and plasma-assisted combustion modes. Operation of the torch in a hydrocarbon/oxygen combustion mode is investigated with microwave power applied to modify the combustion process. The objective of this investigation is to quantify the changes in the combustion process as microwave power is applied to intensify the discharge.

Diagnostic measurements performed include (1) gas temperatures by optical emission spectroscopy, (2) flame/discharge power densities calculated from flame geometries, and (3) flame species to show how the presence of microwaves affects the flame. These measurements are made using a brass nozzle and a ceramic nozzle.

## **ACKNOWLEDGMENTS**

I thank my mom for being my support for 26 years. I also thank the Man above for helping me through the tough times and for His love. I would also like to thank my advisor, Dr. Indrek Wichman, for challenging me and encouraging me.

Special thanks goes to the Electrical Engineering professors, Dr. Grotjohn and Dr. Asmussen, and Materials Science professor, Dr. Case, all of whom advised me throughout this project.

I also thank the electrical engineering students, Kadek Hemawan, Stanley Zuo, and Jeffri Narendra for their help and guidance. Thank you to Kadek who has given me permission to use select figures created by him.

## TABLE OF CONTENTS

LIST OF TABLES.....	vi
LIST OF FIGURES.....	vii
Chapter 1.....	1
1.1 Introduction.....	1
1.2 Literature on plasma-enhanced combustion.....	6
Chapter 2.....	8
2.1 Nomenclature.....	8
2.2 Single-step chemistry.....	9
2.3 Multi-step chemistry.....	27
Chapter 3.....	43
3.1 Introduction to equipment.....	43
3.2 Overall experimental setup.....	43
3.2.1 Torch.....	43
3.2.1.1 Introduction to torch.....	43
3.2.1.2 Torch design and dimensions.....	44
3.2.1.2.1 Ceramic nozzle design and fabrication.....	47
3.2.2 Electrical network and cavity.....	52
3.2.3 Gas system.....	55
3.3 Diagnostics and measurement techniques.....	57
3.3.1 Optical emission spectroscopy (OES).....	58
3.3.2 Infrared camera.....	60
3.3.3 Thermocouple.....	63
Chapter 4.....	66
4.1 Introduction.....	66
4.2 Rotational temperature theory.....	66
4.3 Gas temperature of N <sub>2</sub> .....	71
4.4 Gas temperature of C <sub>2</sub> .....	74
Chapter 5.....	78
5.1 Introduction.....	78
5.2 Flame/discharge photographs.....	78
5.3 Geometric analysis.....	88
5.4 Impact of microwaves on combustion.....	91
5.4.1 Optical emission spectroscopy (OES).....	93
5.5 Flame/discharge temperatures and profiles.....	105
5.5.1 Data collected from infrared (IR) camera.....	109
Chapter 6.....	113
6.1 Summary of results.....	113

6.2 Recommendations .....	115
APPENDICES.....	117
Appendix A .....	118
Appendix B .....	119
BIBLIOGRAPHY.....	121

## LIST OF TABLES

Table 3.1 Torch part dimensions in millimeters and inches.....	46
Table 3.2 Nozzle flow limits. Maximum flow rates for each type of nozzle, in sccm and m/s. Note the ceramic nozzle allows a higher maximum flow rate than the brass nozzle with the same diameter. ....	57
Table 4.1 Rotational constants for the electronic states of nitrogen and carbon.	67
Table 4.2 Values used for the N <sub>2</sub> rotational temperature calculations for the R branch of the (2,0) SPS.....	73
Table 5.1 Gas flow limitations for three nozzles with units in sccm and m/s.....	79
Table 5.2 Lengths of flames with varying flow rates, corresponding to Figure 5.1. The shaded cells highlight stoichiometric flow rates.....	81
Table 5.3 Flame speeds calculated for flames shown in Figure 5.7 as power decreases from 39 W to 33 W. Calculations are based on Equation (5.1). ....	88
Table A.1 Values for thermocouple temperature measurements.....	118
Table B.1 Values used for flame extinction plot in Chapter 5.....	119
Table B.2 Values found in temperature plots in Chapter 5.....	119

## LIST OF FIGURES

Figure 1.1 Schematic of experimental apparatus including the plasma/flame torch inside microwave cavity. The torch houses a gas line and water line, and microwave power is inputted midstream. A combustion flame is produced inside a cavity that creates an electric field pattern exciting a  $TM_{012}$  (transverse magnetic) mode. A window is present for observation and diagnostic measurements (optical emission spectroscopy (OES), for example) [3]. .....2

Figure 1.2 Species and radical concentration curves in regions  $\delta_I$ ,  $\delta_{II}$ , and  $\delta_{III}$  of the combustion process. With the addition of microwaves, the electron/ion concentration is possibly greater than with combustion alone. ....4

Figure 2.1 Temperature distribution in relation to flame front for the simple infinite-reaction-rate model described by Eq (2.3). Note the jump in temperature gradient across the flame front. 14

Figure 2.2 Schematic of reactant mass fraction distribution for the infinitesimally thin flame described by Eq (2.6) on either side of the flame, with  $r=0$  on either side. Note, once again as in Figure 2.1, the discontinuity in the gradient of  $Y_R$ ,  $[dY_R/dx]=Y_{RU}u_f/D$ . ....16

Figure 2.3 Schematic of stretching transformation in nondimensional scale. The inner coordinate  $\Xi$  is large and negative near  $\xi = 0^-$ , large and positive near  $\xi = 0^+$ , and of the order unity in the flame sheet.....21

Figure 2.4 Plot of anticipated solution after applying stretching transformation. .24

Figure 2.5 Curve representing a two-step combustion mechanism.....29

Figure 2.6 Curve representing fuel species behavior for a two-step mechanism. ....35

Figure 3.1 Left: photograph of disassembled PTB. Right: photograph of assembled torch demonstrating hand-held easiness..... 44

Figure 3.2 Internal structure schematic drawing of the PTB with the brass nozzle. This unit is also called the "torch applicator." Note the center conductor and the water cooling system. The inner conductor is adjustable to create an optimal electric field that is concentrated at or near the tip of the nozzle [18]. ..... 45

Figure 3.3 Left: cross section of nozzle with gas and water lines. The gas line is soldered to the wall of the nozzle. Water cooling is necessary to keep the solder from melting. Water enters the inside of the inner conductor near the tip of the

nozzle and circulates throughout, and exits near the base of the conductor. Right: cross-sectional drawing of the nozzle with dimensions in millimeters..... 47

Figure 3.4 Left: sketch of ceramic nozzle showing smoothly converging path from nozzle inlet to exit, including diameter dimensions. Right: photograph of ceramic nozzle attached to the inner conductor. Note the gold-sputtered coat on the ceramic. .... 48

Figure 3.5 Schematic of ceramic nozzle. Left: ceramic powder being pressed axially by two cylinders at 2000 psi inside a cylindrical metal die and shaped by a parabolic graphite mold. Right: nozzle after pressing and drilling of exit pathway. Note the outside corners of the nozzle are still square. Careful hand sanding rounds these corners (represented by dotted lines) so the flame does not sit on a radially-large surface. .... 50

Figure 3.6 Photographs of: (a) tumbler used for mixing powders and for shaping graphite, (b) axial press used for pressing powder in the die, and (c) digitally controlled furnace used for sintering specimens..... 51

Figure 3.7 Overall experimental setup, including electrical circuit, torch and cavity, gas system, and diagnostic setup [3]. .... 53

Figure 3.8 PTB and microwave cavity setup, including details of the cavity and the electrical field pattern and wave modes. The torch is placed vertically in the cavity and tuned so the flame interacts with the microwaves, creating a plasma-enhanced hybrid flame. The dimensions of the cavity-penetrated torch are given. .... 55

Figure 3.9 Schematic of the gas setup. Gas flows from the compressed tank, through MFCs. It is then premixed before entering the torch. Methane ( $\text{CH}_4$ ) and oxygen ( $\text{O}_2$ ) are the primary gases used in the experiments. The microwave power is fed through the side of the torch applicator ( $P_{\text{micro}}$ ) and the water cooling lines are also shown. .... 56

Figure 3.10 Schematic of OES system. Light is emitted from discharge, analyzed in the monochromator, and collected and organized in the computer..... 60

Figure 3.11 Left: photograph of the data acquisition system used to measure temperature with a Type K thermocouple. System is connected to a computer with a GPIB cable. Right: device built to sweep thermocouple through flame at a constant speed. Note the spherical thermocouple junction..... 65

Figure 4.1 Energy level diagram for a band with P, Q, and R branches, relative to wavelength ( $\lambda$ ), rotational energy levels ( $J$ ), and vibrational levels ( $\nu$ ) [27].....68

Figure 4.2 Laboratory process for temperature calculations: light is emitted from the flame/discharge and focused by a lens into the spectrometer, where intensities and wavelengths are recorded. ....71

Figure 4.3 Plot of intensity (or current since the units are arbitrary) versus wavelength for the N<sub>2</sub> spectrum, commonly used for rotational temperature calculations. R<sub>20</sub> - R<sub>30</sub> list the order of the rotational bands. ....72

Figure 4.4 Boltzmann plot for the bands R<sub>20</sub> – R<sub>30</sub> of the N<sub>2</sub> spectrum. ....74

Figure 4.5 C<sub>2</sub> spectrum of a Swan System, identifying the bands R<sub>25</sub> – R<sub>45</sub>. ....75

Figure 4.6 Boltzmann plot for the bands R<sub>25</sub> – R<sub>45</sub> of the C<sub>2</sub> spectrum, for the 180/60 sccm O<sub>2</sub>/CH<sub>4</sub> pure flame. ....77

Figure 5.1 Photographs of pure combustion flames with varying flow rates, measured in sccm. The 0.4 mm-diameter brass nozzle is used. ....80

Figure 5.2 Photographs of a pure plasma discharge, with a flow rate of 200 sccm argon and 30 W microwave power. Note that the torch is not confined within the cavity.....82

Figure 5.3 Photographs of flame/discharges inside the cavity as 40-100 W microwave power is added. The 0.2 mm-diameter brass nozzle is used. The flow rate for the top set of photos is 40/0 sccm O<sub>2</sub>/CH<sub>4</sub>, i.e. no fuel is present. The flow rate for the bottom set is 40/20 sccm O<sub>2</sub>/CH<sub>4</sub>, a stoichiometric ratio. Scales are provided for flame dimensions. Camera speed and aperture are 1.6 and 3.5, respectively. ....83

Figure 5.4 Photographs of flame/discharges inside the cavity as microwave power is added, 20-80 W. The 0.4 mm-diameter ceramic nozzle is used. The flow rate is 200/100 sccm O<sub>2</sub>/CH<sub>4</sub>, a stoichiometric ratio. A scale is provided for flame dimensions. Camera shutter speed and aperture are 1.6 s and 3.5, respectively. ....84

Figure 5.5 Photographs of flame/discharges inside the cavity with a ceramic nozzle comparing 0 W to 80 W of microwave power.....84

Figure 5.6 Photographs of flame/discharges inside the cavity as microwave power is added, 10-100 W. The 0.4 mm-diameter brass nozzle is used. The flow rate for the top set is 70/24 sccm O<sub>2</sub>/CH<sub>4</sub>. The flow rate for the bottom set is 153/70 sccm O<sub>2</sub>/CH<sub>4</sub>. A scale is provided for flame dimensions. Camera shutter speed and aperture are 1/30 s and 3.5, respectively. ....86

Figure 5.7 Additional photographs from Figure 5.6. The flow rate is 70/24 sccm O<sub>2</sub>/CH<sub>4</sub> and all other conditions are the same as listed in Figure 5.6. The top

sequence shows the flame/discharge as microwave power increases; the bottom sequence is power decreasing. This intermediate behavior gives rise to a hysteretic affect. ....87

Figure 5.8 Power density as a function of non-dimensional power, evaluated from flame/discharge geometries shown in Figure 5.6, with flow rates of 70/24 sccm O<sub>2</sub>/CH<sub>4</sub> and 153/70 sccm O<sub>2</sub>/CH<sub>4</sub>. The powers of combustion are provided: 15 W for the first flow and 44 W for the second flow. ....90

Figure 5.9 Flame height as a function of non-dimensional power, evaluated from flame/discharge geometries, shown in Figure 5.4, with flow rates of 70/24 sccm O<sub>2</sub>/CH<sub>4</sub> and 153/70 sccm O<sub>2</sub>/CH<sub>4</sub>. ....90

Figure 5.10 Flame extinction or blow-out plot of equivalence ratio versus total volumetric flow rate, V<sub>TOT</sub>. Each data point is provided with the combustion power of the flame at a particular flow rate, where fuel is present. Note that a discharge is maintained with no fuel when 20-100 W of microwave power is added. A spreadsheet of raw data can be seen in Appendix B. ....93

Figure 5.11 OES scan of C<sub>2</sub> in a stoichiometric (200/100 sccm O<sub>2</sub>/CH<sub>4</sub>) combustion flame and hybrid (combustion plus 40 W microwave power) discharge using a 0.4 mm-diameter ceramic nozzle. ....95

Figure 5.12 OES scan of N<sub>2</sub> in a stoichiometric (160/80 sccm O<sub>2</sub>/CH<sub>4</sub>) combustion flame and hybrid (combustion plus 40, 50, 100 W microwave power) discharge using the 0.4 mm-diameter brass nozzle. "Fuel lean" is a flow rate of 160/54 sccm O<sub>2</sub>/CH<sub>4</sub>. The last set of data is from a discharge of only 160 sccm O<sub>2</sub> and 50 W of microwave power (no fuel is present). Data from 30 W of microwave power and below show no N<sub>2</sub> signal, similar to the combustion-only case, and therefore are excluded from the plot. ....96

Figure 5.13 Second set of data: OES scan of N<sub>2</sub> in a hybrid (160/80 sccm O<sub>2</sub>/CH<sub>4</sub> combustion plus 10-80 W microwave power) flame/discharge using the 0.4 mm-diameter brass nozzle. ....97

Figure 5.14 OES scan of N<sub>2</sub> in a hybrid flame/discharge with a flow rate of 160/80/10 sccm O<sub>2</sub>/CH<sub>4</sub>/N<sub>2</sub> with varying microwave power, 30-80 W. Note that N<sub>2</sub> is injected upstream into the flow of gases, CH<sub>4</sub> and O<sub>2</sub>. ....97

Figure 5.15 OES scan of C<sub>2</sub> in a stoichiometric (160/80 sccm O<sub>2</sub>/CH<sub>4</sub>) combustion flame and hybrid (combustion plus 10-100 W microwave power) discharge using the 0.4 mm-diameter brass nozzle. "Fuel lean" has a flow rate of 160/54 sccm O<sub>2</sub>/CH<sub>4</sub>. ....98

Figure 5.16 Second set of data: OES scan of C<sub>2</sub> in a combustion (160/80 sccm O<sub>2</sub>/CH<sub>4</sub>) and hybrid (combustion plus 10-80 W microwave power) flame/discharge using the 0.4 mm-diameter brass nozzle. ....99

Figure 5.17 OES scan of O<sub>2</sub> in a stoichiometric (160/80 sccm O<sub>2</sub>/CH<sub>4</sub>) combustion flame and hybrid (combustion plus 40, 50, 100 W microwave power) discharge using the 0.4 mm-diameter brass nozzle. "Fuel lean" is a flow rate of 160/54 sccm O<sub>2</sub>/CH<sub>4</sub>. The last set of data is from a discharge of only 160 sccm O<sub>2</sub> and 50 W of microwave power (no fuel is present). Data from 30 W of microwave power and below show no O<sub>2</sub> signal, similar to the combustion-only case, and therefore are excluded from the plot. ....100

Figure 5.18 OES scan of OH in a stoichiometric (160/80 sccm O<sub>2</sub>/CH<sub>4</sub>) combustion flame and hybrid (combustion plus 40, 50, 100 W microwave power) discharge using the 0.4 mm-diameter brass nozzle. "Fuel lean" is a flow rate of 160/54 sccm O<sub>2</sub>/CH<sub>4</sub>. Data from 30 W of microwave power and below show no OH signal, similar to the combustion-only case, and therefore are excluded from the plot. ....101

Figure 5.19 OES scan of CH in a stoichiometric (160/80 sccm O<sub>2</sub>/CH<sub>4</sub>) combustion flame and hybrid (combustion plus 10-100 W microwave power) discharge using the 0.4 mm-diameter brass nozzle. "Fuel lean" is a flow rate of 160/54 sccm O<sub>2</sub>/CH<sub>4</sub>. ....101

Figure 5.20 Relative intensities of N<sub>2</sub> emissions as a function of absorbed microwave power, measured from flame/discharges with flow rates of 160/80 sccm, 160/54 sccm, and 160/0 sccm O<sub>2</sub>/CH<sub>4</sub>, and also a flow rate of 160/80/10 sccm O<sub>2</sub>/CH<sub>4</sub>/N<sub>2</sub> with N<sub>2</sub> injection. Intensities are recorded from four sets of experiments to show consistency, and values are recorded from peak intensities, at a wavelength of ~ 3769 Å. ....102

Figure 5.21 Relative intensities of C<sub>2</sub> emission as a function of absorbed microwave power, measured from a stoichiometric flame/discharge with a flow rate of 160/80 sccm O<sub>2</sub>/CH<sub>4</sub>. Intensities are recorded from three sets of experiments to show consistency, and values are recorded from peak intensities, at a wavelength of ~ 5130 Å. ....103

Figure 5.22 Relative intensities of O<sub>2</sub> emission as a function of absorbed microwave power, measured from flame/discharges with flow rates of 160/80 sccm O<sub>2</sub>/CH<sub>4</sub> and 160/54 sccm O<sub>2</sub>/CH<sub>4</sub>. Intensities are recorded from one set of experiments, and values are recorded from peak intensities, at a wavelength of ~ 3340 Å. ....103

Figure 5.23 Relative intensities of CH emission as a function of absorbed microwave power, measured from flame/discharges with flow rates of 160/80 sccm O<sub>2</sub>/CH<sub>4</sub> and 160/54 sccm O<sub>2</sub>/CH<sub>4</sub>. Intensities are recorded from one set of

experiments, and values are recorded from peak intensities, at a wavelength of  $\sim 4270 \text{ \AA}$ .....104

Figure 5.24 OES scan of combustion flame (160/80 sccm  $\text{O}_2/\text{CH}_4$ ) and hybrid flame/discharge (addition of 40 W microwave power) for an entire range of visible emission spectra. The wavelength and relative intensities are given at the peak ( $\lambda = 4280 \text{ \AA}$ ) for each set of data. Molecules and radicals are listed next to their visible spectra. A 0.4 mm-diameter *ceramic* nozzle is used for this data. ....105

Figure 5.25 Temperature profile of a stoichiometric  $\text{CH}_4/\text{O}_2$  flame from a type K thermocouple. Photograph of the flame shows where the thermocouple scans the flame. The plot provides experimental data and also displays a qualitative example of a theoretical temperature distribution with an adiabatic flame temperature of 3000 K, taken as an average temperature.....106

Figure 5.26  $\text{N}_2$  rotational temperature of a flame/discharge as a function of absorbed microwave power for data for three different flow rates: 160/80/10 sccm, 100/50/3.6 sccm, and 60/30/2 sccm  $\text{O}_2/\text{CH}_4/\text{N}_2$ .....107

Figure 5.27  $\text{N}_2$  and  $\text{C}_2$  rotational temperatures of flame/discharges as a function of absorbed microwave power, for four sets of data (independent experiments). The flow rate for the first three sets is 160/80 sccm  $\text{O}_2/\text{CH}_4$ , and 160/80/10  $\text{O}_2/\text{CH}_4/\text{N}_2$  for the fourth set. Tables of raw data are found in Appendix B. ....108

Figure 5.28 Temperature profile images from the IR camera of a flame as it is modified by microwave power, 40 W and 60 W. The flame is not confined within the cavity. The temperature scale is provided, but does not provide an accurate temperature reading. The gas flow rate is 200/100 sccm  $\text{O}_2/\text{CH}_4$ . ....110

Figure 5.29 Temperature profiles sketched from the IR camera images (from Figure 5.28) for both a combustion flame (represented by the solid lines) and a hybrid flame/discharge with 40 W microwave power added (dashed lines). ....110

Figure 5.30 Temperature profile images from the IR camera for a plasma-only discharge: 200 sccm argon excited by 40 W microwave power. Each image is recorded with a different filter. The image in the bottom right corner shows the temperature profiles of the hot gases beyond the plasma.....111

Figure 5.31 Temperature profile images from the IR camera for a stoichiometric combustion flame formed by a ceramic nozzle. Different camera filters are used to highlight different sections of the flame. The temperature profiles of the nozzle are also illustrated.....112

## Chapter 1

### Introduction and Literature Review

#### 1.1 Introduction

Plasma-assisted combustion is an area of research that has been studied for several decades. Thoroughly understanding the physics of this coupled phenomenon and optimizing it have yet to be accomplished. The motivation behind the current research at MSU is to improve the combustion process, to conserve energy required for combustion, and to design and build an efficient, small-scale, plasma-enhanced, premixed-flame, combustion torch. Increased power, combustion efficiency, and flame stability are all advantages of combining a non-thermal plasma (NTP) with combustible gases [1].

Experimental data are gathered and theoretical calculations are performed in order to define the flame characteristics and behaviors; flame temperature and flame dimensions (height, width) are measured, *relative* specie concentrations are observed, stoichiometric mass flow rates are calculated for three fuels, the premixed flame theory is reviewed, and a ceramic-flow nozzle is fabricated.

The flame configuration employed in this project is, similar to other studies [1, 2], a circular premixed flame burner in which the premixed gases are combusted as they exit a nozzle into ambient air. The nozzle is enclosed in a microwave cavity, which houses the microwaves, producing the flame/plasma interaction. It is hoped that the experiments can demonstrate a quantitative difference between a pure fuel/oxygen flame and a flame that has been enhanced by microwave plasma. Varying levels of microwave power (measured

in Watts) and premixed reactant flow rates (and mixture ratios) are examined. A schematic diagram of the experimental configuration is shown in Figure 1.1.

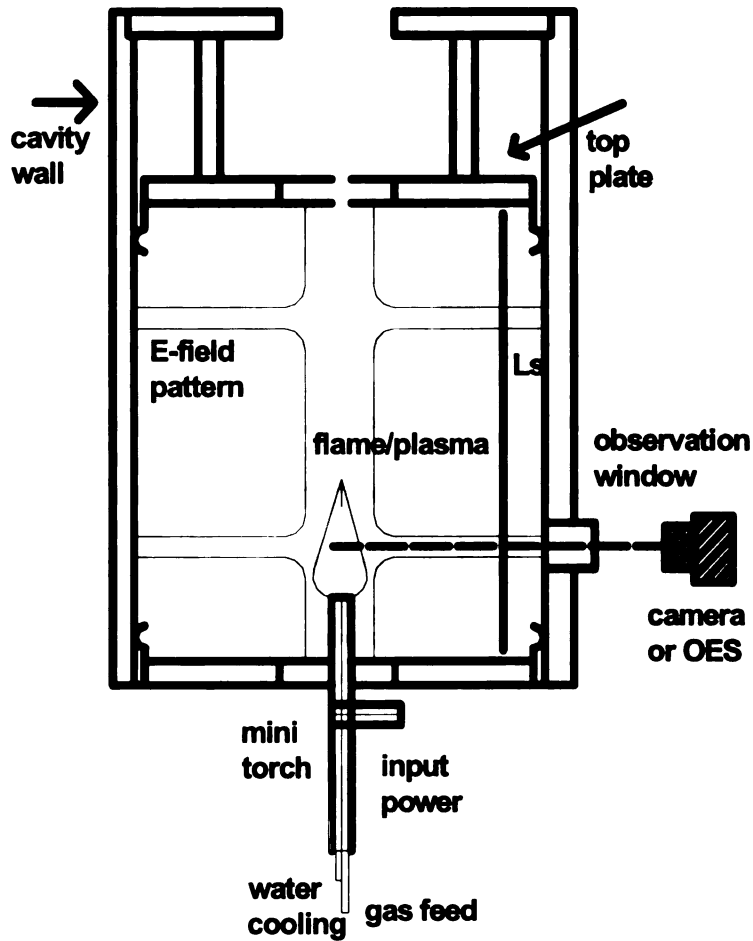


Figure 1.1 Schematic of experimental apparatus including the plasma/flame torch inside microwave cavity. The torch houses a gas line and water line, and microwave power is inputted midstream. A combustion flame is produced inside a cavity that creates an electric field pattern exciting a  $TM_{012}$  (transverse magnetic) mode. A window is present for observation and diagnostic measurements (optical emission spectroscopy (OES), for example) [3].

Flame stability, flame propagation speed, and combustion chemistry of premixed, laminar flames are all affected by inducing an electric current in the flow of gases. It is believed that the plasma assists in breaking down the

combustion fuel thereby producing free radicals (e.g. H, OH, O), which are chemically unstable and therefore highly reactive. By using the plasma to convert gaseous fuels into reactive species, the ensuing combustion process does not rely on the self-generation of reactive species, and therefore hotter flames may be produced. Plasma also yields a potentially more concentrated flame.

A possible mechanism for flame power augmentation is the acceleration of the reaction by enhanced radical concentration levels. Thus, if the microwave power is suitably and optimally “focused” it may produce, in the upstream gases (prior to the flame sheet), a larger concentration of free radicals, H, OH, O, that can accelerate the combustion reaction (see Figure 1.2). The accelerated reaction may produce a narrow, more spatially concentrated flame, thereby making a flame/plasma with a high power density. The practical goal is to employ this enhanced power density to perform some kinds of cutting, machining, material conditioning, localized heating, or other applications.

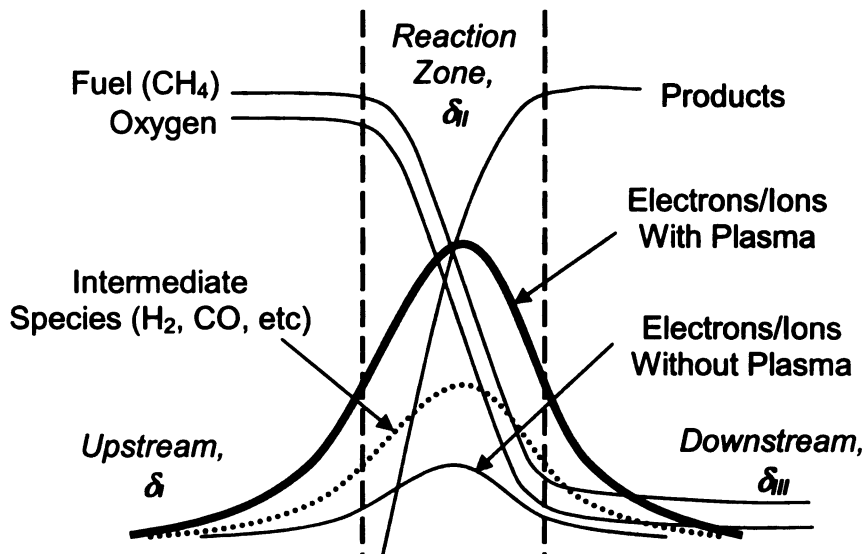


Figure 1.2 Species and radical concentration curves in regions  $\delta_I$ ,  $\delta_{II}$ , and  $\delta_{III}$  of the combustion process. With the addition of microwaves, the electron/ion concentration is possibly greater than with combustion alone.

Microwaves are the type of electric field induced in the MSU torch. Microwave power produces a clean discharge and has been studied by researchers at MSU for many years [4]. Microwave plasmas are also referred to as non-thermal plasmas (NTPs), meaning these plasmas are not produced by extremely high temperatures but by some other means. NTPs have several advantages over thermal plasmas. High gas and ion temperatures are produced by thermal plasmas, whereas NTPs diminish the effects of high gas temperatures, while still producing energetic electrons and other reactive molecules (H, OH, O, etc). As a result, with a microwave plasma it is possible to consider a gas mixture with multiple temperatures. When only a select number of molecules are excited, this results in little waste enthalpy associated with a gas stream [1]. The MSU apparatus currently operates with a non-thermal plasma.

In addition to combustion and plasma considerations, there is the important issue of nozzle design, materials, and construction. The nozzle must channel the reactants into the flame; hence it must accommodate a controlled flow of the gases in the design range of flow rate. The nozzle must also allow the microwaves to concentrate in the appropriate locations so that the beneficial flame/plasma interaction will in fact occur. Whether this concentration (of microwaves) location is immediately in front of the flame or further upstream (in the nozzle, for example) is a matter of research and study. Finally, the nozzle material must allow the microwaves to concentrate without being absorbed, and thereby rendered ineffective.

A plasma-enhanced torch is desirable for practical purposes. Industry is interested in such a torch for cutting and metal forming. The small, concentrated flame allows precision cutting. A plasma welder eliminates the mess that many combustion-based welders create. Applications may even be designed for outer space. Buoyancy does not play a role in the flame produced by the torch because it is so small and concentrated. In addition, the torch is easy to handle because of its small size.

To further develop this ongoing plasma-enhanced combustion research, experiments are conducted and theoretical calculations are studied. A mini torch was built that allows combustible gases to flow through and be activated by an electric field, producing free electrons, a current, and a plasma discharge. Temperatures are measured using an IR camera, an optical emission spectrometer (OES) for specific gas temperatures, and a thermocouple. Power

density is calculated based on flame/discharge geometry and absorbed microwave power. In addition, a ceramic nozzle was designed and implemented for experiments.

## **1.2 Literature on plasma-enhanced combustion**

There has been no systematic and prolonged effort to study plasma-enhanced combustion, but over the past several decades isolated attempts have been made to enhance combustion with an electric field. A short account follows.

Plasma-induced combustion research was conducted at Los Alamos National Laboratory in the past five years or so in an attempt to improve the combustion process. More stable and efficient combustion was desired and thought to be achieved by introducing a supplemented electric field [1].

The experimental setup consisted of a coaxial silent discharge reactor, producing a dielectrical barrier discharge (DBD), or silent discharge. The propane and air mix just before ignition and no converging nozzle is used to form a flame. The gases are pre-treated by NTP prior to ignition. Rosocha *et al.* argue that NTPs have advantages over thermal plasmas, as discussed in Section 1.1. NTPs promote efficient combustion by increasing flame speed, decreasing flame length, reducing soot formation, and reducing  $\text{NO}_x$  and other combustion by-product emissions.

The Los Alamos team found that with an NTP system, plasma increases flame blow-out limits, but at a relatively low propane flow rate. The partial pressures of common hydrocarbon combustion products (water and carbon dioxide) increased while propane fragments decreased when the plasma was

added, which suggests that the propane is being burned more completely. The flame propagation speed increased with an increase in electric field intensity.

Experimental work done by Chintala *et al.* at Ohio State University shows that non-equilibrium RF plasma-assisted ignition and combustion achieves large-volume ignition in premixed flows. At higher reactant flow rates and lower temperatures, the RF discharge allowed ignition to occur, as compared with no discharge. Leaner combustng fuel flows were achieved with the RF discharge. Radical species such as CN, CH, C<sub>2</sub>, OH, and O atoms, measured by visible emission spectroscopy, were detected in the hydrocarbon air flow [2].

Much experimental work has been performed by Starikovskii *et al.* in Russia, quantifying pulsed nanosecond plasma-assisted combustion. They found that the plasma discharge significantly decreases the ignition temperature and that the flame's blow-off velocity increased significantly for a low discharge energy input. An increase in the flame propagation velocity can be explained by the production of atomic oxygen in a discharge by the quenching of electronically excited N<sub>2</sub> and the dissociation of molecular oxygen on electron impact ( $O_2 + e^- \rightarrow O + O + e^-$ ). A numerical model was developed to describe the influence of the pulsed discharges on the combustion process [5, 6].

Experiments that were performed by Whitehair *et al.* at Michigan State University use a high-temperature nozzle and discharge chamber materials for the development of a microwave electrothermal thruster. It was shown that regenerative cooling and flow stabilization improved thruster performance [4].

## Chapter 2

### Premixed Flame Theory

#### 2.1 Nomenclature

a	Integration constant
A	Pre-exponential factor ( $\text{cm}^3/\text{gmol}\cdot\text{s}$ )
B	Species parameter, $c_p T/Q + Y_R$
$c_p$	Constant-pressure specific heat ( $\text{J}/\text{kg}\cdot\text{K}$ or $\text{J}/\text{kmol}\cdot\text{K}$ )
C	Arbitrary coefficients
D	Binary diffusion coefficient ( $\text{m}^2/\text{s}$ )
$\mathcal{D}$	Damköhler number
E	Activation energy ( $\text{J}/\text{kmol}$ )
F	Fuel
k	Thermal conductivity ( $\text{W}/\text{m}\cdot\text{K}$ ) or Rate constant ( $\text{cm}^3/\text{gmol}\cdot\text{s}$ )
K	Damköhler number
$\ell$	Loss term ( $\text{J}/\text{m}^3\cdot\text{s}$ )
L	Normalized heat loss term
Le	Lewis number
m	Flame thickness (m)
M	Third body
n	Reaction order or integer in gamma function
P	Products
$\dot{q}$	Heat release rate ( $\text{J}/\text{s}$ )
Q	Energy per unit mass ( $\text{J}/\text{kg}$ )
$\overline{Q}$	Normalized heat release
r	Reaction rate function
$\dot{r}$	Mass generation rate ( $1/\text{s}$ )
$R_u$	Universal gas constant ( $\text{J}/\text{kmol}\cdot\text{K}$ )
$\bar{s}$	Normalized flame speed
S	Flame speed ( $\text{m}/\text{s}$ )
t	Time (s)
T	Temperature (K)
u	Velocity ( $\text{m}/\text{s}$ )
W	Mean molecular weight ( $\text{kg}/\text{mol}$ )
x	Distance in dimensional system (m)
y	Normalized mass fraction
Y	Mass fraction ( $\text{kg}/\text{kg}$ )
Z	Radical

## **Greek Symbols**

$\alpha$	Thermal diffusivity, $k/\rho c_p$ ( $m^2/s$ ) or exponential coefficient
A	Enthalpy ratio, $(T_b - T_u)/T_b$
$\beta$	Zeldovich number, $-E(T_b - T_u)/(R_u T_b^2)$
$\delta$	Laminar flame thickness (m)
$\theta$	Normalized temperature, $(T - T_u)/(T_b - T_u)$
$\Theta$	Normalized temperature after stretching, $\beta(1 - \theta)$
$\Lambda$	Burning rate eigenvalue
$\mu$	Exponential coefficient
$\rho$	Constant density ( $kg/m^3$ )
$\xi$	Nondimensional length scaling, $x'/(u_f \alpha)$
$\Xi$	Normalized length after stretching, $\xi/\delta$
$\tau$	Normalized temperature
$\omega$	Molar consumption rate ( $mol/m^3 \cdot s$ )

## **Subscripts**

C	Consumed
b	Burned gas
B	Burned
f	Flame
F	Fuel
H	Homogeneous
L	Laminar
u	Unburned gas
P	Particular
R	Reactant
RB	Burned reactant
RU	Unburned reactant
Z	Radical

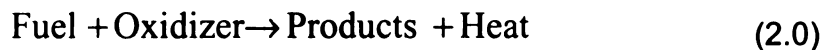
## **2.2 Single-step chemistry**

One-dimensional, premixed-flame theory for single-step chemistry has been studied for decades and is well understood [7]. Reactants combust and form products and heat energy, as shown in expression (2.0). Equation (2.1) is the governing energy equation for the transient propagation of a reaction front into a traveling gas. The first term represents the rate of change of temperature at position  $x$ ; the second term represents convection in the gas moving with

velocity,  $u$ ; the diffusion and reaction terms follow. The source/sink term, in the simplified model of Equation (2.1), is replaced by boundary conditions on the temperature and is redefined in Equation (2.5) as  $p q$ . Assumptions to be made are: complete combustion; constant pressure and density; inviscid flow; and a laminar and infinitesimally thin flame front. The analysis derived in this chapter is referenced from [7] and also from notes of an independent study course taken from the advisor of this thesis, Dr. Indrek Wichman.

Although the assumptions seem drastic, they provide simple mathematical models while proving remarkable success in laying the foundations for understanding the structure, properties, stability, and dynamics of many combustion phenomena. For example, the density changes can be neglected when considering the diffusive transport [1]. Explicit and asymptotic solutions are found by making difficult problems tractable to mathematical analysis [8,9,10,11,12,13,14,15]. provide examples of explorations of various types of flames with a single-step chemistry model. An asymptotic approach, based on high activation energy, is used in one-step chemistry analysis.

The temperature far upstream is given by a constant unburned value,  $T_u$ , and the temperature far downstream is a constant burned value,  $T_b$ . Figure 2.1 schematically represents the temperature distribution for this idealized premixed flame (PF).



$$\frac{\partial T}{\partial t} + u \frac{\partial T}{\partial x} = \alpha \frac{\partial^2 T}{\partial x^2} + \text{source/sink} \quad (2.1)$$

Equation (2.1) is invariant under the application of a Galilean transformation according to the following definitions:

$$x' = x + u_f t$$

$$u' = u + u_f$$

$$t' = t$$

Essentially, the new  $x$ -coordinate follows the flame front since  $dx'/dt = dx/dt + u_f$  and  $dx/dt = -u_f$  at the flame; therefore,  $dx'/dt = 0$  at the flame. The velocity,  $u$ , is the flow speed entering the flame front from the upstream direction. Note also that it is assumed that the flame front propagates at a constant speed,  $u_f$ . Without this assumption a Galilean transformation is not useful. The transformation yields the governing equation in (2.2) for the gas temperature on either side of the flame.

$$\frac{\partial T}{\partial t'} + u' \frac{\partial T}{\partial x'} = \alpha \frac{\partial^2 T}{\partial x'^2} \quad (2.2)$$

The location of the origin is arbitrary since  $x' \rightarrow x' + \text{constant}$  produces exactly the same equation as in (2.2); as a result, it is convenient to let the flame front sit at

$x' = 0$ . The flame front is not affected by  $t = t'$ ; therefore, in the coordinate system attached to the steadily propagating flame front, the unsteady term in Equation (2.2) vanishes ( $\partial(\cdot)/\partial t' = 0$ ). When the flow velocity is zero ( $u = 0$ ), the transformed velocity is constant ( $u' = u_f$ ), and Equation (2.2) reduces to a simple ODE, shown in Equation (2.3), in which the coefficients,  $u_f$  and  $\alpha$ , are constant:

$$u_f \frac{dT}{dx'} = \alpha \frac{d^2T}{dx'^2} \quad (2.3)$$

The solution to Equation (2.3) is as follows:

$$T = C_1 + C_2 e^{x' / (\alpha / u_f)}$$

The physical domain is divided into two regions: one upstream of the flame sheet ( $-\infty < x < 0$ ); the other downstream of the flame sheet ( $0 < x < \infty$ ). In the upstream region, the two following boundary conditions are imposed:

$$T(-\infty) = T_u \quad \text{and} \quad \lim_{x \rightarrow 0^-} T = T_b$$

These boundary conditions yield Equation (2.4), also seen in Figure 2.1:

$$T = T_u + (T_b - T_u)e^{x/(\alpha/u_f)} \quad (2.4)$$

The following boundary conditions are imposed for the downstream region to find  $T=T_b$  as the downstream solution:

$$T < \infty, \text{ as } x \rightarrow \infty \quad \text{and} \quad T = T_b, \text{ as } x \rightarrow 0^+$$

Across the PF the temperature gradient is discontinuous:

$$\left[ \frac{\partial T}{\partial x} \right]_{flame} \equiv \left( \frac{\partial T}{\partial x} \right)_{x \rightarrow 0^-} - \left( \frac{\partial T}{\partial x} \right)_{x \rightarrow 0^+} = 0 - (T_b - T_u)/(\alpha/u_f)$$

It will be shown later that this jump in temperature gradient is proportional to the combustion heat release by the flame.

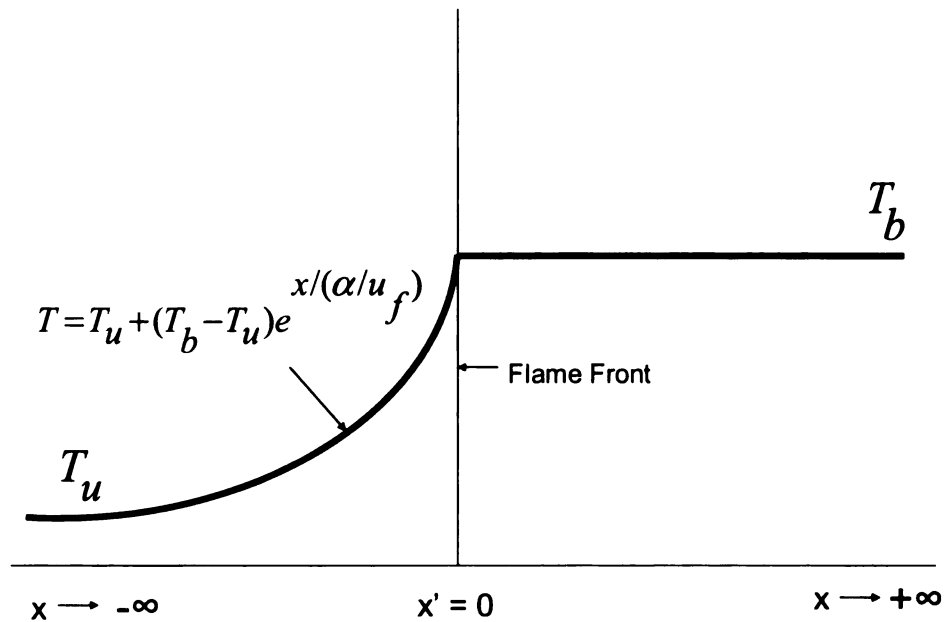


Figure 2.1 Temperature distribution in relation to flame front for the simple infinite-reaction-rate model described by Eq (2.3). Note the jump in temperature gradient across the flame front.

In this work, consider that the coordinate system is fixed to the PF, and that the flame has a steady speed,  $S_L$  ( $S_L = u_f$ ). In this case, the Galilean transformation from the laboratory to flame-fixed coordinates works. In contrast to the infinitesimally thin flame described on either side of the flame by Equation (2.3), the energy equation is now written in the form shown in Equation (2.5). This equation is valid everywhere in the gas! In the following expressions,  $Q$  is the energy per unit mass,  $\rho$  is the density, the heat release rate (J/s) is  $\dot{q}$ , and  $\dot{r}$  is the mass generation rate (kg/s) :

$$\rho u c_p \frac{dT}{dx'} = \lambda \frac{d^2T}{dx'^2} + \rho \dot{q} \quad (2.5)$$

$$\rho \dot{q} \equiv \rho Q \dot{r}$$

$$\dot{r} = A Y_R^n e^{-E/R_u T}$$

The species equation is given in Equation (2.6). The first term represents convection, and the second and third terms represent diffusion and reaction, respectively. Figure 2.2 schematically illustrates the mass fraction ( $Y_R$ ) distribution of reactants in the combustion process for the infinitesimally thin flame.

$$\rho u_f \frac{dY_R}{dx'} = \rho D \frac{d^2Y_R}{dx'^2} - \rho \dot{r} \quad (2.6)$$

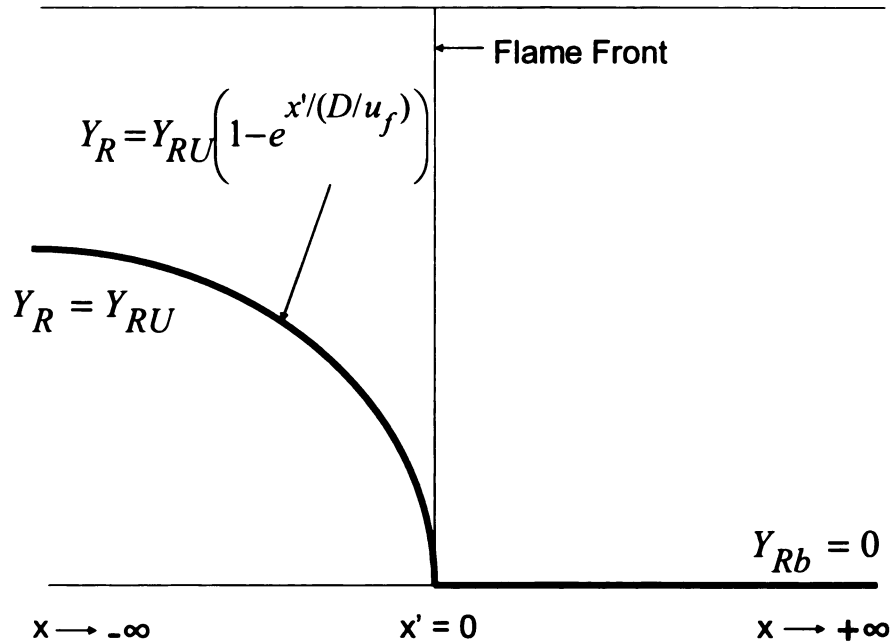


Figure 2.2 Schematic of reactant mass fraction distribution for the infinitesimally thin flame described by Eq (2.6) on either side of the flame, with  $r=0$  on either side. Note, once again as in Figure 2.1, the discontinuity in the gradient of  $Y_R$ ,  $[dY_R/dx]=Y_{RU}u_f/D$ .

Equations (2.5) and (2.6), along with the specification of  $r = f(T, Y_R)$ , serve to complete the specification of the PF problem. The two unknown dependent variables are  $T$  and  $Y_R$ . The number of unknown variables (and equations) can be reduced to one by forming a coupling function defined by the sum,  $B = c_p T/Q + Y_R$ , and by assuming  $\rho D = k/c_p$  (Lewis number of unity). As a result, Equations (2.5) and (2.6) yield the following homogeneous equation and its solution:

$$u_f \frac{dB}{dx} = D \frac{d^2B}{dx^2}$$

$$B = C_0 + C_1 e^{(u_f x / D)}$$

Since  $B$  must be bounded at  $x = +\infty$ , it is required that  $C_1 = 0$ . Thus,  $B = C_0$ , which is evaluated at  $x = -\infty$ , where  $T = T_\infty$  and  $Y_R = Y_{RU}$ . This provides the following expression:

$$\frac{c_p T}{Q} + Y_R = \frac{c_p T_u}{Q} + Y_{RU}$$

The above relationship is exact, and it applies everywhere between  $-\infty < x < +\infty$ , even inside the flame. At  $x = +\infty$ ,  $T = T_b$  and  $Y_R = 0$  to find  $T_b = T_u + QY_{RU}/c_p$  as the expression for the burned gas temperature. The relation for  $B$  gives  $Y_R$  in terms of  $T$ , as follows:

$$Y_R = Y_{RU} - \frac{c_p}{Q}(T - T_u) \quad (2.7)$$

By substituting Equation (2.7) into  $r(T, Y_R)$ , the mathematical problem can be reduced to the solution of the energy equation only (Equation 2.8), subject to  $T(-\infty) = T_u$  and  $T(+\infty) = T_b$ :

$$u_f \frac{dT}{dx} = D \frac{d^2T}{dx^2} + \frac{Q}{\rho c_p} A \left[ Y_{RU} - \frac{c_p}{Q} (T - T_u) \right]^n e^{-E/R_u T} \quad (2.8)$$

Prior to solving for  $T(x)$ , however, normalized dependent and independent variables are introduced as follows:

Dependent:  $\theta \equiv \frac{T - T_u}{T_b - T_u}$

Independent:  $\xi \equiv u_f \frac{x'}{\alpha}$

The following dimensionless parameters are also defined:

Damköhler number:  $\mathbb{D} \equiv \frac{\alpha}{u_f^2} A Y_{RU}^{n-1} e^{-E/R_u T_b}$

Zeldovich number:  $\beta \equiv \frac{-E}{R_u T_b^2} (T_b - T_u)$

Enthalpy ratio:  $A \equiv \frac{T_b - T_u}{T_b}$

Substituting these definitions into Equation (2.8) leads to the following equation for  $\theta(\xi)$ , subject to  $\theta(-\infty) = 0$  and  $\theta(+\infty) = 1$ :

$$\frac{d\theta}{d\xi} = \frac{d^2\theta}{d\xi^2} + \mathcal{D}(1-\theta)^n e^{\frac{-\beta(1-\theta)}{1-A(1-\theta)}} \quad (2.9)$$

Equation (2.9) is solved in three zones that are subsequently matched. The upstream-zone solution, already obtained in Figure 2.1, is shown in Equation (2.4) and is also given by  $\theta = e^\xi$  for  $\xi < 0$ . The downstream solution in Figure 2.1 is  $T = T_b$ , or  $\theta = 1$ . The solution for  $\theta(\xi)$  in the reaction zone remains to be found. The reaction zone connects the upstream “preheat” zone to the downstream “reacted gas” zone.

In the “inner” or reaction zone near  $\xi = 0$ , it can be shown that the diffusion and reaction terms dominate over the convection term [15]. Applying a stretching transformation demonstrates this.

A stretching transformation, or reaction zone scaling, utilizes the following definitions:

Rescaled, nondimensional temperature:

$$\Theta \equiv \beta(1 - \theta)$$

Rescaled Damköhler number:

$$\mathcal{D} \equiv \Lambda \beta^{n+1}$$

Rescaled special coordinate:

$$\Xi \equiv \frac{\xi}{\delta}$$

Here  $\delta$  is an as-yet-undefined nondimensional scaling of the coordinate,  $\xi$ , in the reaction zone, and is a measure of the nondimensional reaction zone thickness.

It is noted that the following expression is defined for convenience:

$$\xi = \pm \frac{\delta}{2} \Rightarrow \Xi = \pm \frac{1}{2}$$

Integrating Equation (2.9) from  $-\infty$  to  $+\infty$ , or  $-\delta/2$  to  $+\delta/2$ , suggests that it is reasonable to define the quantity,  $\delta\mathfrak{D}/\beta^n$  as of the order of unity. Therefore, the characteristic flame width is approximated by Equation (2.10) below. Note that the nondimensional characteristic flame width is of the order  $1/\beta$ , so that for large  $\beta$  the reaction zone becomes very thin [15]. Thus  $\Xi = \beta\xi$  is defined.

$$\delta \approx \frac{\beta^n}{\mathfrak{D}} = \frac{\beta^n}{\Lambda\beta^{n+1}} \approx \frac{1}{\beta} \quad (2.10)$$

Equation (2.9) reduces to Equation (2.11) below, after applying reaction-zone scaling factors,  $\Theta$ ,  $\mathfrak{D}$ , and  $\Xi$ :

$$-\frac{1}{\beta} \frac{d\Theta}{d\Xi} = -\frac{d^2\Theta}{d\Xi^2} + \Lambda\Theta^n e^{-\Theta/(1-\Lambda\Theta/\beta)} \quad (2.11)$$

The convection term is of the order  $1/\beta$  which is significantly smaller than the diffusion and reaction terms which are of the order unity. As a result, in the limit of large  $\beta$ , the convection term is neglected to lowest order. Figure 2.3 illustrates the normalized temperature distribution after the stretching transformation.

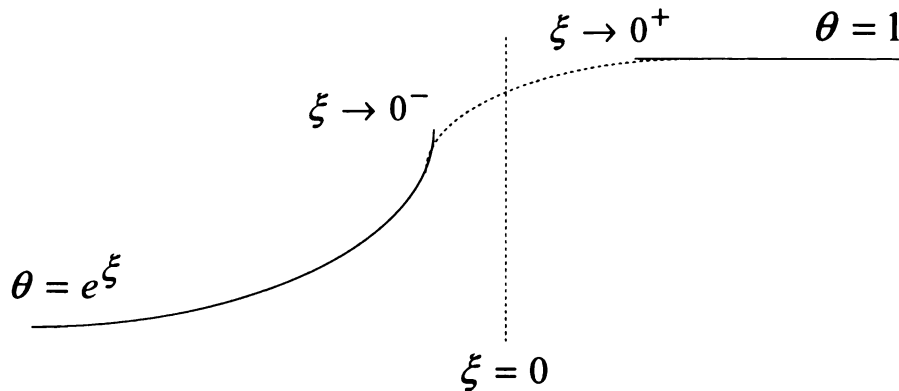


Figure 2.3 Schematic of stretching transformation in nondimensional scale. The inner coordinate  $\Xi$  is large and negative near  $\xi = 0^-$ , large and positive near  $\xi = 0^+$ , and of the order unity in the flame sheet.

It is presently impossible to analytically solve the nondimensional ODE in Equation (2.11). Rather, an approximate solution is found. Perturbation expansions of the normalized temperature and eigenvalue,  $\Theta$  and  $\Lambda$ , respectively, are performed. The following perturbation expansions are substituted into Equation (2.11).

$$\Theta = \Theta_0 + \beta^{-1}\Theta_1 + \beta^{-2}\Theta_2 + \dots$$

$$\Lambda = \Lambda_0 + \beta^{-1}\Lambda_1 + \beta^{-2}\Lambda_2 + \dots$$

This substitution results in the Equations (2.12) and (2.13) below for the zeroth and first order problems:

$$\Theta_0'' = \Lambda_0 \Theta_0^n e^{-\Theta_0} \quad (2.12)$$

$$\Theta_1'' - \Theta_0'' \left( \frac{n}{\Theta_0} - 1 \right) \Theta_1 = \Theta_0' + \Theta_0'' \left( \frac{\Lambda_1}{\Lambda_0} - \Lambda \Theta_0^2 \right) \quad (2.13)$$

The boundary conditions for Equations (2.12) and (2.13) are obtained from the outer solution in the following way. First, the upstream solution is analyzed and provides the following two expressions, as  $\xi \rightarrow 0^-$ :

$$\theta = e^\xi = 1 + \xi + \frac{\xi^2}{2!} + \frac{\xi^3}{3!} + \dots$$

$$\frac{d\theta}{d\xi} = 1 + \xi + \frac{\xi^2}{2} + \dots$$

Then, applying the relationships,  $\theta = 1 - \Theta/\beta$  and  $\xi = \Xi/\beta$ , yields the following:

$$\Theta = -\Xi - \frac{\Xi^2}{2\beta} + \dots$$

$$\frac{d\Theta}{d\Xi} = -1 - \frac{\Xi}{\beta} + \dots$$

From the perturbation expansion, letting  $\Theta = \Theta_0 + \Theta_1/\beta + \dots$  gives the following boundary conditions, and so on for the higher values:

$$\Theta_0 \rightarrow -\Xi \quad \text{and} \quad \frac{d\Theta_0}{d\Xi} \rightarrow -1 \quad \text{as} \quad \Xi \rightarrow -\infty \quad (2.14)$$

$$\Theta_1 \rightarrow -\frac{\Xi^2}{2} \quad \text{and} \quad \frac{d\Theta_1}{d\Xi} \rightarrow -\Xi \quad \text{as} \quad \Xi \rightarrow -\infty \quad (2.15)$$

For the downstream solution, as  $\xi \rightarrow 0^+$ , the following distributions are found:

$$\theta = 1$$

$$\frac{d\theta}{d\xi} = 0$$



Once again, applying  $\theta = 1 - \Theta/\beta$  and  $\xi = \Xi/\beta$  gives  $\Theta = 0$  and  $d\Theta/d\Xi = 0$ , so that, along with  $\Theta = \Theta_0 + \Theta_1/\beta + \dots$ , the following boundary conditions are found and are displayed in Figure 2.4:

$$\Theta_0 = 0 \quad \text{and} \quad \frac{d\Theta_0}{d\Xi} = 0 \quad \text{as} \quad \Xi \rightarrow +\infty \quad (2.16)$$

$$\Theta_1 = 0 \quad \text{and} \quad \frac{d\Theta_1}{d\Xi} = 0 \quad \text{as} \quad \Xi \rightarrow +\infty \quad (2.17)$$

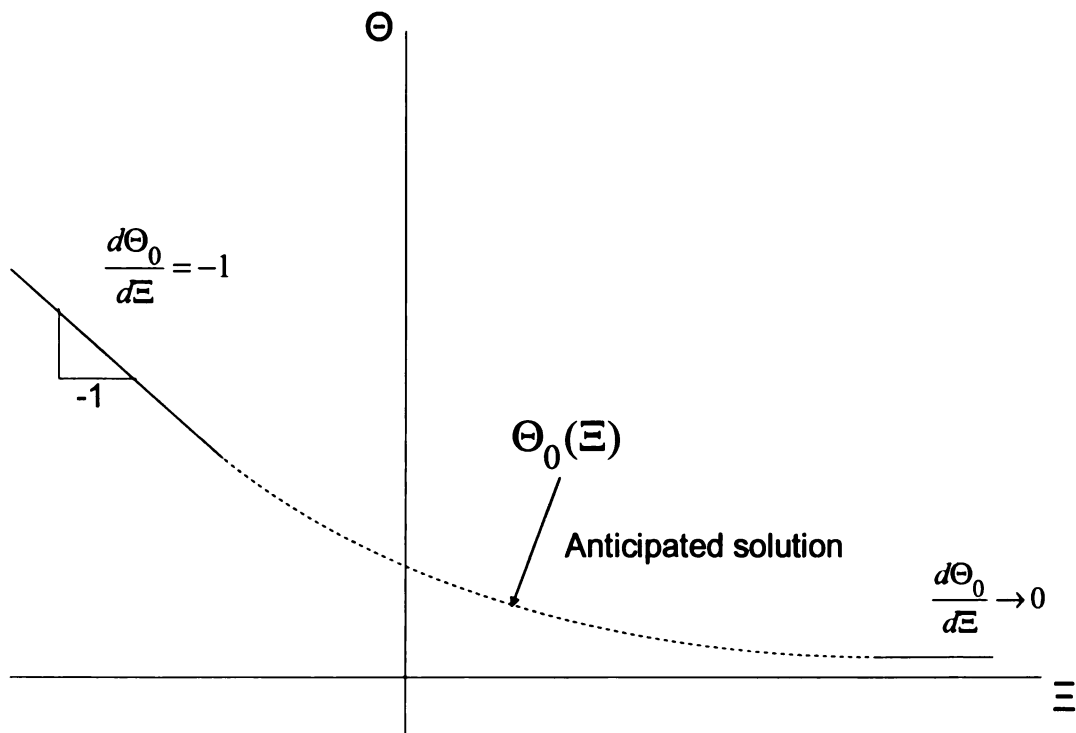


Figure 2.4 Plot of anticipated solution after applying stretching transformation.

The lowest-order problem consists of Equation (2.12) and BCs (2.14) and (2.16). The first-order problem consists of Equation (2.13) and BCs (2.15) and (2.17). Both problems are over-determined and thus each solution will also produce a result for the various eigenvalues,  $\Lambda_0, \Lambda_1$ , etc.

To solve the lowest-order problem, first the eigenvalue is calculated by integrating Equation (2.12) from  $\Xi = -\infty$  to  $\Xi = +\infty$  and imposing the conditions given by Equations (2.14) and (2.16). Therefore, the following computes:

$$\begin{aligned} \int_{-\infty}^{+\infty} \frac{d^2\Theta_0}{d\Xi^2} d\Xi &= \int_{\Xi=-\infty}^{\Xi=+\infty} \frac{1}{2} \frac{d}{d\Theta} \left( \frac{d\Theta}{d\Xi} \right)^2 \frac{d\Theta}{d\Xi} d\Xi = \int_{\Theta_0 \rightarrow -\infty}^{\Theta_0 \rightarrow 0} \frac{1}{2} d \left( \frac{d\Theta_0}{d\Xi} \right)^2 \\ &= \frac{1}{2} \left[ \frac{d\Theta_0}{d\Xi} \right]_{\Theta_0 \rightarrow 0}^2 - \frac{1}{2} \left[ \frac{d\Theta_0}{d\Xi} \right]_{\Theta_0 \rightarrow -\infty}^2 \\ &= \frac{1}{2} [0 - 1] = -\frac{1}{2} \end{aligned}$$

$$= \int_{\Theta_0(\Xi=-\infty)}^{\Theta_0(\Xi=+\infty)} \Lambda_0 \Theta_0^n e^{-\Theta_0} d\Theta_0 = \Lambda_0 \int_{\infty}^0 \Theta_0^n e^{-\Theta_0} d\Theta_0 = -\Lambda_0 \Gamma(n+1)$$

Thus,  $\Lambda_0 = \frac{1}{2} \Gamma(n+1)$  gives the lowest-order flame speed eigenvalue. The procedure above is replicated, but integrated from  $\Xi = -\infty$  only, to a finite (and unspecific) value, where  $\Theta_0 = \Theta_0(\Xi)$ . The result is as follows:

$$\left(\frac{d\Theta_0}{d\Xi}\right)^2 = 1 - \frac{\int_0^{\Theta_0} s^n e^{-s} ds}{\int_0^{\infty} s^n e^{-s} ds} = 1 - \frac{Q(n+1, \Theta_0)}{\Gamma(n+1)} \equiv P(n+1, \Theta_0)$$

$$P(n+1, \Theta_0) = \frac{Q}{\Gamma} = \frac{\int_0^{\Theta_0} s^n e^{-s} ds}{\int_0^{\infty} s^n e^{-s} ds} \leq 1 \quad (2.18)$$

Equation (2.20) is obtained below by taking the square root of Equation (2.18) and rewriting it as Equation (2.19). Equation (2.20) is solved numerically.

$$\frac{d\Theta_0}{d\Xi} = -\sqrt{P(n+1, \Theta_0)} \equiv -g(n, \Theta_0) \quad (2.19)$$

$$-\Xi = \int_a^{\Theta_0} \frac{ds}{g(n, s)} \quad (2.20)$$

The integration constant,  $a$ , is found by integrating Equation (2.20) while applying upstream boundary conditions on  $\Theta_0(\Xi)$ . A transcendental equation forces a numerical solution for  $\Theta_0(\Xi)$ , which is then used to deduce  $\theta$  and thus  $T$ , and finally  $Y_R$  from Equation (2.7).

The expressions for  $\Theta_1$  and  $\Lambda_1$  can be found by introducing a variable change in the form of  $g$ , as follows:

$$-g \equiv \frac{d\Theta_0}{d\Xi}$$

$$\Theta_1 = -\frac{\Theta_0^2}{2} \quad (2.21)$$

By a similar procedure (by integrating the first-order problem from the far upstream ( $\Xi = -\infty$ ) to the far downstream ( $\Xi = +\infty$ )), it is relatively straight forward to find, for the first-order eigenvalues correction, the following expression in Equation (2.22):

$$\frac{\Lambda_1}{\Lambda_0} = (n+2)(n+1) - 2 \int_0^{\infty} (1-g) ds \quad (2.22)$$

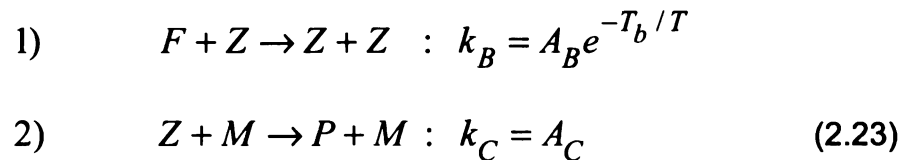
The first-order analysis will not be pursued any further. The interested reader may consult Chapter 5 of [16].

### 2.3 Multi-step chemistry

The analysis of a single-step chemical reaction does have limitations in describing combustion behavior. For example, the Zeldovich number ( $\beta$ ) for a

satisfactory description of stable flame balls must be about three times the actual value found in typical hydrocarbon reactions [7].

Realistic Zeldovich numbers are invoked in the two-step mechanism shown in expression (2.23). This expression describes how a radical species  $Z$  attacks a fuel species  $F$  to produce more radical in the form of chain branching, until all the fuel particles are consumed. A third body, denoted by  $M$ , represents any type of molecule. In reaction 2 the radical collides with  $M$  to produce product  $P$  and leftover  $M$ . The rate constant,  $k_B$ , in the first reaction varies with temperature; however, the rate constant,  $k_C$ , for the second reaction does not. The chain-branching reaction requires energy from the flame to generate radicals,  $T_B = E_B/R_u$  (heat release step). The second reaction has zero activation energy, and is therefore independent of  $T$ . Thus,  $T_C = 0$  (heat absorption step).



schematically represents the first step in the above mechanism.

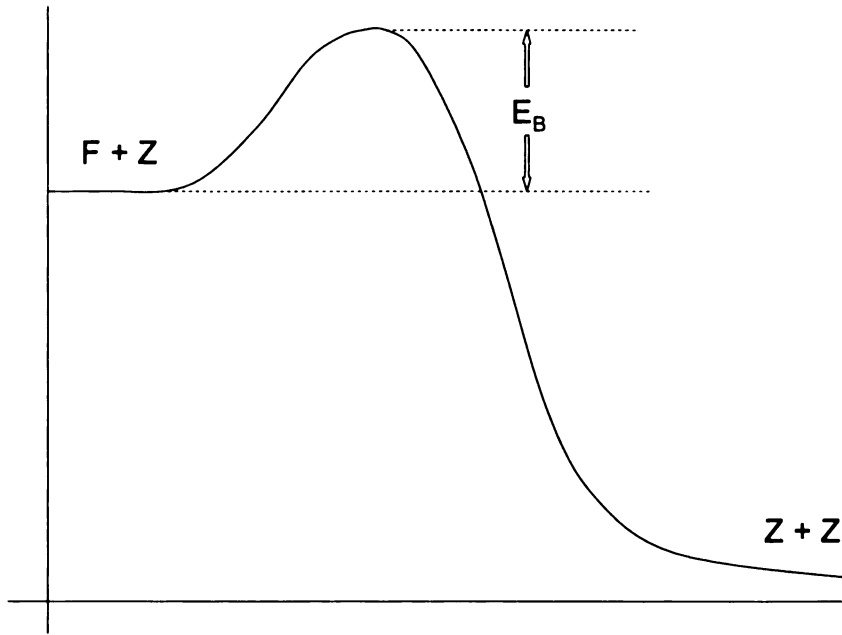


Figure 2.5 Curve representing a two-step combustion mechanism.

The governing equations for the two-step mechanism include the fuel species equation, the radical species equation, and the energy equation, shown in Equations (2.24), (2.25), and (2.26), respectively. The primes imply differentiation with respect to  $x$ .

$$\rho S Y_F' = \rho D_F Y_F'' - W_F \omega_B \quad (2.24)$$

$$\rho S Y_Z' = \rho D_Z Y_Z'' - W_Z \omega_F - W_Z \omega_C \quad (2.25)$$

$$\rho c_p S T' = k T'' + Q \omega_C - \ell \quad (2.26)$$

The laminar flame speed is denoted by  $S$ ,  $W$  is the mean molecular weight, and  $\omega_B$  and  $\omega_C$  are defined as follows:

$$\omega_B = A_B \left( \frac{\rho Y_F}{W_F} \right) \left( \frac{\rho Y_Z}{W_Z} \right) e^{-T_B / T}$$

$$\omega_C = A_C \left( \frac{\rho Y_Z}{W} \right) \left( \frac{\rho}{W} \right)$$

In Equation (2.26), the quantity  $\ell$  refers to a heat loss term that can be used to represent the rate of bulk heat loss (through radiation, for example).

For simplification, the equations are normalized using the following definitions for the independent ( $x \rightarrow \xi$ ) and dependent ( $Y_Z, Y_F, T$ ) variables:

$$x = x_s \xi \quad (x_s \text{ is chosen for convenience, } x_s = \frac{\alpha}{u})$$

$$Y_Z = y_Z Y_{ZS} \quad (Y_{ZS} \text{ is chosen for convenience, } Y_{ZS} = Y_{FO} \frac{W_Z Le_Z}{W_f Le_F})$$

$$\bar{s} = \frac{S}{u} \quad (u \text{ is chosen for convenience later in the analysis})$$

$$\tau = \frac{T - T_0}{T_f - T_0} \quad (\text{normalized temperature field})$$

$$Y_F = y_F Y_{FO} \quad (\text{normalized fuel mass fraction})$$

The fuel, radical, and energy equations are now reduced to the following nondimensional equations:

$$Le_F \bar{s} \frac{dy_F}{d\xi} = \frac{d^2 y_F}{d\xi^2} - Kr \quad (2.27)$$

$$Le_Z \bar{s} \frac{dy_Z}{d\xi} = \frac{d^2 y_Z}{d\xi^2} + Kr - y_Z \quad (2.28)$$

$$\bar{s} \frac{d\tau}{d\xi} = \frac{d^2\tau}{d\xi^2} + \frac{\bar{Q}}{Le_F} y_z - L \quad (2.29)$$

Note the similarity of these equations to Equations (2.5) and (2.6). Select variables that are included in Equations (2.27), (2.28), and (2.29) are defined below:

Lewis number:  $Le = \frac{\alpha}{D}$

Damköhler number:  $K = \frac{x_s^2}{\rho D_F Y_{FO}} W_F A_B \frac{\rho Y_{FO}}{W_F} \frac{\rho Y_{ZS}}{W_Z} e^{-T_B/T_f}$

Reaction rate function:  $r = y_F y_Z e^{\left[ \frac{T_B}{T_f} - \frac{T_B}{T} \right]}$

Heat release:  $\bar{Q} = \frac{Q Y_{FO}}{c_p (T_f - T_0) W_F}$

Heat loss term:  $L = \frac{\ell x_s^2}{k(T_f - T_0)}$

The quantity  $r$  is redefined in terms of the Arrhenius rate expression  $k(T)$ , as follows:

$$k(T) = e^{T_B \left( \frac{1}{T_f} - \frac{1}{T_0 + \tau(T_f - T_0)} \right)}$$

The expression for  $k(T)$  is rearranged after some algebra to give the expression as shown below, where  $\alpha = 1 - T_0/T_f$  and  $\beta = T_B(T_f - T_0)/T_f^2$ .

$$k(T) = e^{-\beta \left( \frac{1-\tau}{1-\alpha(1-\tau)} \right)}$$

To solve the fuel species equation, the reaction zone is assumed to be very thin. Upstream ( $\xi < 0^-$ ) the flame, the reaction rate  $r$  is zero. Therefore, Equation (2.27) becomes Equation (2.30).

$$Le_F \bar{s} y_F' = y_F'' \quad (2.30)$$

Letting  $y_F' = \exp(m\xi)$ , it can be shown that the characteristic equation gives  $Le_F \bar{s} m = m^2$ , so that the two roots are  $m = 0$  and  $m = Le_F \bar{s}$  for the homogeneous solution. The solution to Equation (2.27) is written below:

$$y_F = C_1 e^{0\xi} + C_2 e^{(Le_F \bar{s})\xi} \quad (2.31)$$

The boundary conditions are as follows:

Far upstream:  $y_F = 1$  as  $\xi \rightarrow -\infty$

On upstream side of  
flame front:  $y_F = 0$  as  $\xi \rightarrow 0^-$

The values for  $C_1$  and  $C_2$  in Equation (2.31) are computed, and the fuel species upstream solution is given below:

$$y_F = 1 - e^{(Le_F \bar{s})\xi} \quad \text{for } \xi < 0^- \quad (2.32)$$

The downstream ( $\xi > 0^+$ ) solution uses the same solution (Equation (2.31)) as the upstream solution. Equation (2.33) and the boundary conditions that follow lead to the solution given below by Equation (2.34):

$$y_F = C_3 + C_4 e^{(Le_F \bar{s})\xi} \quad (2.33)$$

Far downstream:  $y_F < 1$  as  $\xi \rightarrow +\infty$

At downstream side  
of flame front:  $y_F = 0$  as  $\xi \rightarrow 0^+$

$$\text{Solution: } y_F = 0 \quad \text{for } \xi > 0^+ \quad (2.34)$$

A curve demonstrating this behavior for the fuel species is shown in Figure 2.6.

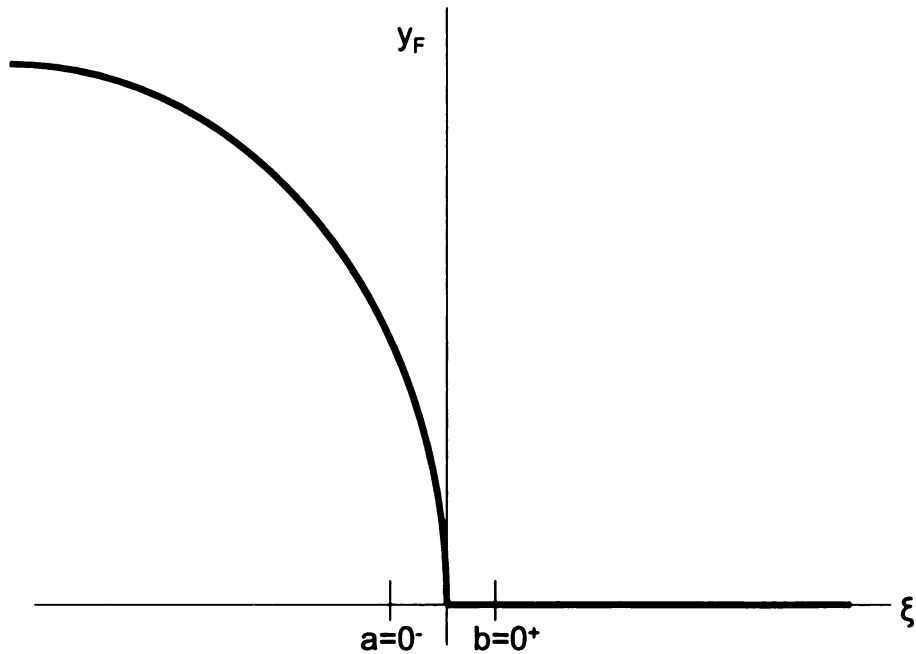


Figure 2.6 Curve representing fuel species behavior for a two-step mechanism.

Equation (2.27) can also be integrated, from  $a$  to  $b$ , to show that  $y_F$  is continuous, or that the jump of  $y_F$  across the flame is zero [7].

The radical species equation, given in Equation (2.28), is solved by implementing similar methods as the fuel equation. By integrating from  $a$  to  $b$  in the above Figure 2.6, when  $a = 0^-$  and  $b = 0^+$  are  $\xi$ -locations that straddle the

reaction front, the result,  $\int_a^b K r d\xi = -\bar{s} L e_F$ , is found. Then following expression

is deduced, which yields the jump condition on the gradient of  $y_Z$ :

$$\left[ y_Z' \right] \equiv y_Z' \Big|_{0^+} - y_Z' \Big|_{0^-} = -\bar{s} Le_F \quad (2.35)$$

Letting  $y_Z = \exp(\alpha\xi)$ , the characteristic equation obtained from Equation (2.28) with  $r = 0$  is  $Le_Z \bar{s} \alpha = \alpha^2 - 1$ , whose solution gives the two roots  $\alpha_{1,2}$ , seen below:

$$\alpha_{1,2} = \frac{Le_Z \bar{s}}{2} \pm \frac{1}{2} \sqrt{(Le_Z \bar{s})^2 + 4}$$

Solutions are found both upstream ( $\xi < 0$ ) and downstream ( $\xi > 0$ ) of the flame; the unknown coefficients are set equal to each other because  $y_Z$  is continuous across the flame front. The one unknown coefficient is then solved for using the jump condition from Equation (2.35). The solutions are written below:

$$y_Z = \frac{Le_F \bar{s}}{\alpha_1 - \alpha_2} e^{\alpha_1 \xi} \quad \text{for } \xi < 0$$

$$y_Z = \frac{Le_F \bar{s}}{\alpha_1 - \alpha_2} e^{\alpha_2 \xi} \quad \text{for } \xi > 0$$

Equation (2.29), the energy equation, is solved using a coupled homogeneous and non-homogeneous solution. Equation (2.29) is rearranged into Equation (2.36), where  $L = a^2 \tau$ , assuming  $\ell$  is linear in temperature.

$$\frac{d^2\tau}{d\xi^2} - \bar{s} \frac{d\tau}{d\xi} - a^2\tau = \frac{\bar{Q}}{Le_F} y_z \quad (2.36)$$

Using the results from the species solution, Equation (2.36) can be written as Equation (2.37):

$$\frac{d^2\tau}{d\xi^2} - \bar{s} \frac{d\tau}{d\xi} - a^2\tau = \frac{\bar{Q}}{Le_F} y_z = \frac{\bar{Q}}{Le_F} \frac{Le_F \bar{s}}{(\alpha_1 - \alpha_2)} \begin{cases} e^{\alpha_1}, \xi < 0 \\ e^{\alpha_2}, \xi > 0 \end{cases} \quad (2.37)$$

The upstream solution ( $\xi < 0$ ) is found from a homogeneous and particular solution where  $\tau = \tau_H + \tau_P$ . The homogenous equation for  $\tau$  is as follows:

$$\tau_H = e^{\mu\xi} : \mu^2 - \mu\bar{s} - a^2 = 0$$

The two roots of  $\mu$  are written below:

$$\mu_{1,2} = \frac{\bar{s}}{2} \pm \frac{1}{2} \sqrt{4a^2 + \bar{s}^2}$$

The following roots for  $\alpha$  and  $\mu$  are redefined below, for convenience, noting that  $\mu_{(1)}$  and  $\mu_{(2)}$  are always positive:

$$\alpha_{(1)} = \frac{1}{2} \sqrt{(Le_Z \bar{s})^2 + 4} + \frac{Le_Z \bar{s}}{2} = \alpha_1$$

$$\alpha_{(2)} = \frac{1}{2} \sqrt{(Le_Z \bar{s})^2 + 4} - \frac{Le_Z \bar{s}}{2} = -\alpha_2$$

$$\mu_{(1)} = \frac{1}{2} \sqrt{4a^2 + \bar{s}^2} + \frac{\bar{s}}{2} = \mu_1$$

$$\mu_{(2)} = \frac{1}{2} \sqrt{4a^2 + \bar{s}^2} - \frac{\bar{s}}{2} = -\mu_2$$

These roots yield the homogenous solution for the normalized energy equation, as seen in Equation in (2.38):

$$\tau_H = C_1 e^{\mu_{(1)} \xi} + C_2 e^{-\mu_{(2)} \xi} \quad (2.38)$$

The particular solution is found from Equation (2.37) for the upstream ( $\xi < 0$ ) case:

$$\frac{d^2 \tau_p}{d\xi^2} - \bar{s} \frac{d\tau_p}{d\xi} - a^2 \tau_p = \frac{\bar{Q}}{Le_F} \frac{Le_F \bar{s}}{(\alpha_{(1)} + \alpha_{(2)})} e^{\alpha_{(1)} \xi}$$

Letting  $\tau_p = A \exp\{\mu_{(1)} \xi\}$ , the following algebraic expression is found:

$$A(\alpha_{(1)}^2 - \bar{s}\alpha_{(1)} - a^2) = A(\alpha_{(1)} - \mu_{(1)})(\alpha_{(1)} + \mu_{(2)}) = -\frac{\bar{Q}}{Le_F} \frac{Le_F \bar{s}}{(\alpha_{(1)} + \alpha_{(2)})}$$

where

$$A = -\frac{\bar{Q}}{Le_F} \frac{Le_F \bar{s}}{(\alpha_{(1)} + \alpha_{(2)})(\alpha_{(1)} - \mu_{(1)})(\alpha_{(1)} + \mu_{(2)})}$$

The total solution for the upstream energy equation is written in Equation (2.39).

$$\tau = \tau_H + \tau_P =$$

$$C_1 e^{\mu_{(1)}\xi} + C_2 e^{-\mu_{(2)}\xi} - \frac{\bar{Q}}{Le_F} \frac{Le_F \bar{s} e^{\alpha_{(1)}\xi}}{(\alpha_{(1)} + \alpha_{(2)})(\alpha_{(1)} - \mu_{(1)})(\alpha_{(1)} + \mu_{(2)})} \quad (2.39)$$

The coefficient  $C_2$  is zero because  $\tau < \infty$  and  $\xi \rightarrow -\infty$ ; therefore the second term goes to zero. As  $\xi \rightarrow 0^-$ , the following expressions are obtained:

$$\tau_{0^-} = C_1 - K_1 \quad \text{and} \quad \left(\frac{d\tau}{d\xi}\right)_{0^-} = \mu_{(1)}C_1 - \alpha_{(1)}K_1$$

where

$$K_1 = \frac{\bar{Q}}{Le_F} \frac{Le_F \bar{s}}{(\alpha_{(1)} + \alpha_{(2)})(\alpha_{(1)} - \mu_{(1)})(\alpha_{(1)} + \mu_{(2)})}$$

Downstream of the flame ( $\xi > 0$ ),  $\tau < \infty$  as  $\xi \rightarrow +\infty$ ; therefore,  $C_1$  must be zero and the first term in Equation (2.39) disappears. As  $\xi \rightarrow 0^+$ , the following expressions are found:

$$\tau_{0+} = C_2 - K_2 \quad \text{and} \quad \left( \frac{d\tau}{d\xi} \right)_{0+} = -\mu_{(2)}C_2 + \alpha_{(2)}K_2$$

where

$$K_2 = \frac{\bar{Q}}{Le_F} \frac{\bar{s}}{(\alpha_{(1)} + \alpha_{(2)})(\alpha_{(2)} + \mu_{(1)})(\alpha_{(2)} - \mu_{(2)})}$$

Applying the jump condition leads to expressions for  $C_1$  and  $C_2$ . The solutions are shown below:

$$\tau = \frac{\bar{Q}\bar{s}}{\alpha_1 - \alpha_2} \left\{ \frac{\alpha_1 - \alpha_2}{\mu_1 - \mu_2} \frac{e^{\mu_1 \xi}}{(\alpha_1 - \mu_1)(-\alpha_2 + \mu_1)} - \frac{e^{\alpha_1 \xi}}{(\alpha_1 - \mu_1)(\alpha_1 - \mu_2)} \right\} \quad (\xi < 0)$$

$$\tau = \frac{\bar{Q}\bar{s}}{\alpha_1 - \alpha_2} \left\{ \frac{\alpha_1 - \alpha_2}{\mu_1 - \mu_2} \frac{e^{\mu_2 \xi}}{(-\alpha_2 - \mu_2)(\alpha_1 - \mu_2)} - \frac{e^{\alpha_2 \xi}}{(-\alpha_2 + \mu_2)(-\alpha_2 + \mu_1)} \right\} \quad (\xi > 0)$$

The definition for  $K$  was seen earlier as the following:

$$K = \frac{x_s^2}{\rho D_F Y_{FO}} W_F A_B \frac{\rho Y_{FO}}{W_F} \frac{\rho Y_{ZS}}{W_Z} e^{-T_B/T_f}$$

This expression can be simplified into the following:

$$K = \frac{A_B}{A_C} \frac{W}{W_F} Y_{FO} e^{-T_B/T_f}$$

The asymptotic analysis for a second order reaction shows that  $K = \beta^2$  [7].

Therefore,  $T_f$  is defined by Equation (2.40).

$$K = \frac{A_B}{A_C} \frac{W}{W_F} Y_{FO} e^{-T_B/T_f} = \left( \frac{T_B}{T_f} \right)^2 \left( 1 - \frac{T_0}{T_f} \right)^2 \quad (2.40)$$

For various parameter choices the equations of this subsection can be solved (and have been solved [7]). The solutions plot the flame speed,  $\bar{s}$ , versus the parameters  $a^2/(\bar{Q}-1)$  for fixed  $Le_z$  and  $Le_z^{1/2}a^2$  for fixed  $\bar{Q}$ , showing that for each parameter value ( $a^2/(\bar{Q}-1)$  and  $Le_z^{1/2}a^2$ ) there are either two values of the flame speed  $\bar{s}$ , or none (see Figure 3 of [7]). It is believed, consistent with several decades of premixed flame stability analysis, that the lower branch is unstable whereas the upper branch is stable.

The influence of the radicals enters through the pre-exponential factor,  $A$ . As this increases (or decreases) the parameter containing  $A$  changes and the influence of the radicals is modified. The influence of the plasma, it is believed, can be examined by varying the reaction rate  $A$ , which is altered by the level of the applied electric field. This influence is not examined in this thesis. Another strategy, which also is not examined, is to postulate that in front of the main reaction zone a radical formation region is produced by the plasma. Thus, at a certain distance  $\delta_p$  upstream of the reaction front the radical mass fraction takes

the fixed value  $y_{zp}$ . The remainder of the solution is of course dictated by the conservation equations. This solution, however, in preliminary calculations becomes algebraically extremely complicated and it is not clear that a simpler approach, based on scaling analysis, would not be more feasible.

## **Chapter 3**

### **Equipment and Experimental Methods**

#### **3.1 Introduction to equipment**

The test bed used to study the microwave/flame interaction consists of a miniature microwave plasma torch/burner (PTB) that operates inside a cylindrical cavity. The experimental conditions that occur can be divided into three distinct groups of flames/discharges: 1) pure microwave plasma discharge; 2) pure combustion; and 3) hybrid plasma/combustion discharge. Discussed in this chapter are the overall setup, including the torch, cavity, electrical network, and gas flow, along with the experimental methods employed for data collection and analysis. Images in this thesis are presented in color.

#### **3.2 Overall experimental setup**

##### **3.2.1 Torch**

###### **3.2.1.1 Introduction to torch**

The PTB used for this research was designed and built by researchers in the MSU Electrical and Computer Engineering (ECE) department <sup>1</sup>. It was originally designed for the formation of plasma (argon, helium) in order to study micro-scale plasmas (plasma diameter and height of 1mm and 3mm, respectively) [17, 18]. It operates under atmospheric pressure, but has the capabilities of operating in low pressures down to  $O(10^{-1}$  atm) also. This pure microwave plasma discharge produces relatively low temperatures (1600 K-1800 K) which limits it to cutting paper and melting plastics. As a cutting tool, the torch's discharge must cut plastics and metals with precision; therefore,

<sup>1</sup> Under review for U.S. Patent in 2005

combustion is introduced to produce a high-temperature, hybrid flame/discharge that consists of a plasma discharge coupled with a flame [19].

### 3.2.1.2 Torch design and dimensions

The torch is considered “small-scale” because of the flame/discharge size it produces, which is of the several millimeter scale. Photographs of the brass PTB are shown in Figure 3.1. It is a simple hand-held torch comprising coaxial inner and outer conductors, with inlet/outlets for microwave power, gases, and water (used for cooling). The photograph to the left in Figure 3.1 shows the torch before assembly. It includes, from bottom to top, the outer conductor, the fine-tuning adjuster (which is placed inside the outer conductor and controls the placement of the inner conductor, with the help of a teflon spacer used for centering), the inner conductor, and the microwave coupling unit; the finger stock, allen wrench, and bolts are also shown.

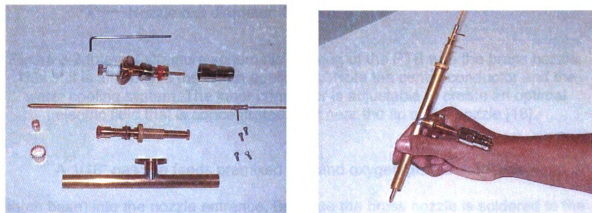


Figure 3.1 Left: photograph of disassembled PTB. Right: photograph of assembled torch demonstrating hand-held easiness.

Figure 3.2 is a schematic of the torch with dimensions. The outer conductor has an 11.1 mm inner diameter, and the inner conductor has an outer diameter of 4.75 mm. All major dimensions of the torch are listed in Table 3.1. The torch is designed so the inner conductor can slide through the outer conductor in axial adjustment (useful for assembly and tuning of the discharge inside the cylindrical cavity). It is centered with two teflon spacers. Fine tuning is available at the base of the torch with an adjustable microwave tuning short.

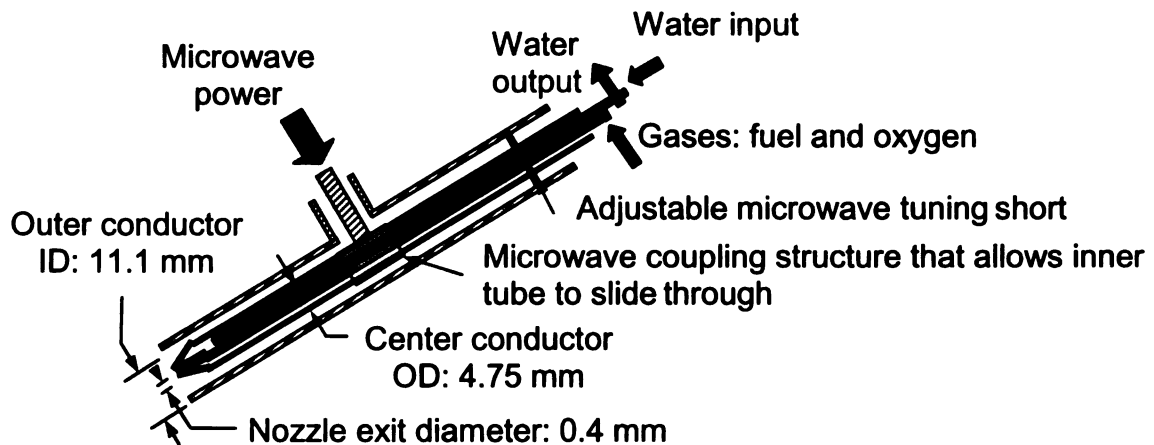


Figure 3.2 Internal structure schematic drawing of the PTB with the brass nozzle. This unit is also called the “torch applicator.” Note the center conductor and the water cooling system. The inner conductor is adjustable to create an optimal electric field that is concentrated at or near the tip of the nozzle [18].

A 1/16” gas line feeds premixed fuel and oxygen (mixed ~ 3 ft upstream of torch base) into the nozzle entrance. Because the brass nozzle is soldered to the inner conductor, flowing water prevents the solder from melting due to flame temperatures above 2000 K. The water inlet and outlet are at the base of the torch, and the water is allowed to circulate throughout the inner conductor. The

microwave current is fed into the torch by a 50-ohm coaxial cable with an N-type connection. The inner and outer conductors create an electrical field that ionizes the gases at or very near the tip exit of the nozzle.

**Table 3.1 Torch part dimensions in millimeters and inches.**

<b>Torch Dimension</b>	<b>Units</b>	
	<b>mm</b>	<b>inches</b>
Inner Conductor Length	197.488	7.775
Inner Conductor OD	4.763	0.188 (3/16)
Inner Conductor Thickness	0.356	0.014
Outer Conductor Length	148.590	5.850
Outer Conductor OD	12.70	0.5 (1/2)
Outer Conductor Thickness	0.813	0.032
Nozzle Inlet Diameter	3.340	0.132
Nozzle Exit Diameter	0.40	0.016
Microwave Input Coaxial Cable Diameter	6.350	0.25 (1/4)
Gas Line Diameter	4.234	0.167 (1/16)
Inlet Water Line Diameter	4.234	0.167 (1/16)
Outlet Water Line Diameter	4.234	0.167 (1/16)

The nozzle, like the rest of the torch, is made of brass, and was designed for relatively easy machining. Drawings of the nozzle can be seen in Figure 3.3, which shows gas/water lines and dimensions. The exit diameter is 0.4 mm. A second nozzle was made with a diameter of 0.2 mm; however, most experiments presented in this thesis are performed with the 0.4 mm-diameter nozzle.

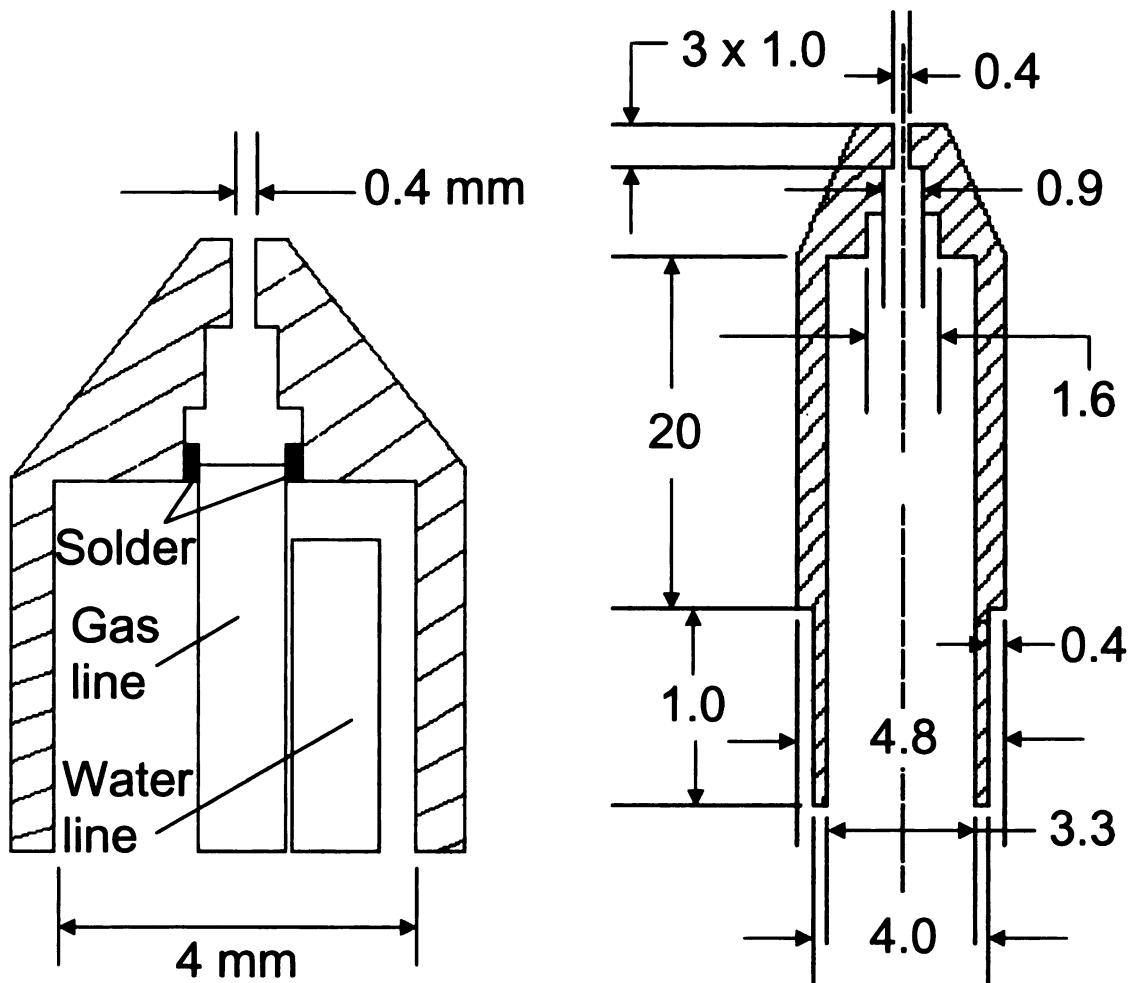


Figure 3.3 Left: cross section of nozzle with gas and water lines. The gas line is soldered to the wall of the nozzle. Water cooling is necessary to keep the solder from melting. Water enters the inside of the inner conductor near the tip of the nozzle and circulates throughout, and exits near the base of the conductor. Right: cross-sectional drawing of the nozzle with dimensions in millimeters.

### 3.2.1.2.1 Ceramic nozzle design and fabrication

Innovative design and fabrication of a second, ceramic nozzle are explored and experimentally tested. The original nozzle of the torch cannot withstand temperatures that the combustion flame produces, and also reflects poor flow geometry. This nozzle is made of brass and is soldered to the inner

conductor. To prevent the solder from melting and detaching from the torch, the inner conductor is water cooled.

Water circulates through the inner conductor to keep the nozzle at a relatively low temperature. A water-cooled nozzle causes the flame to stand off, forming a gap between the flame base and the nozzle exit. A detached flame is not desired because it is unstable and also loses heat energy to the cooled nozzle. In addition, the brass nozzle reflects poor fluid flow. The previous Figure 3.3 shows a drawing of the brass nozzle. The sharp corners induce flow separation and can cause considerable circulation patterns. To eliminate the necessity for water-cooling and to develop improved flow conditions, a smoothly-converging ceramic nozzle has been designed and fabricated. A sketch and photograph of a ceramic nozzle are shown in Figure 3.4.

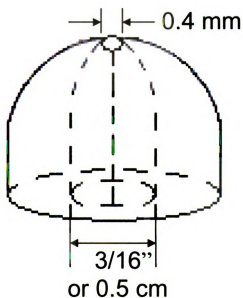


Figure 3.4 Left: sketch of ceramic nozzle showing smoothly converging path from nozzle inlet to exit, including diameter dimensions. Right: photograph of ceramic nozzle attached to the inner conductor. Note the gold-splattered coat on the ceramic.

The process for designing and fabricating a ceramic nozzle involved first shaping graphite “molds” to form the smoothly converging flow region, then preparing the powder used for pressing and sintering.

The design of the nozzle is developed from shaping graphite rods; no specific equation was developed for the converging shape. The graphite (ordered from McMaster Carr) is used to form the converging shape of the nozzle. Rods of 1/4” diameter and lengths varying from 1 - 4 inches are tumbled in bottles lined with sand paper of various grits. The tumbler or rolling machine can be seen in Figure 3.5. Rods are first tumbled inside a bottle (3” diameter) lined with 40-grit paper for 24 - 48 hrs. The ends of the rods become rounded, closely resembling a parabolic curve. This curve is manually plotted and curve-fitted using Excel. Spotlight, a software program developed by NASA, is also useful for such analysis, thus eliminating the time spent manually plotting points along the rod’s edge. These procedures demonstrate that the rods are nearly parabolic at the ends. These rods are then tumbled with 400 grit paper, and finally with 1200 grit paper for 12 - 24 hrs at a time. The higher-grit paper creates a polished, reflecting surface on the rod. The rods are then finely polished with a diamond paste. The ends of the rods (noses) are cut off with a low-speed diamond saw. The parabolic noses are used to press the ceramic powder into its nozzle shape.

The ceramic powder is made with 85% weight alumina ( $\text{Al}_2\text{O}_3$ ) and 15% weight zirconia. Alumina is affordable and offers a 99.9% purity level. It is the close packing of aluminum and oxygen atoms within the structure that leads to its good mechanical and thermal properties [20]. Zirconia is added for increased

strength. The powder is tumbled/mixed for 24 hrs to ensure a homogeneous mixture. Approximately 10 g of powder is axially pressed under 2000 psi using a cylindrical die after inserting the graphite tip. Figure 3.5 provides schematics of the pressing process.

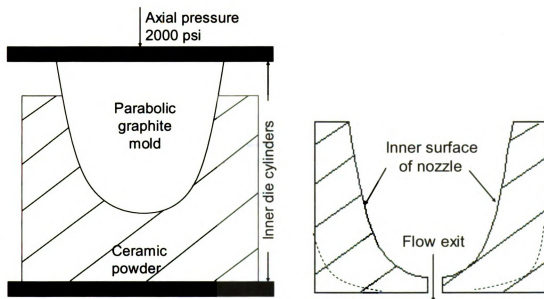


Figure 3.5 Schematic of ceramic nozzle. Left: ceramic powder being pressed axially by two cylinders at 2000 psi inside a cylindrical metal die and shaped by a parabolic graphite mold. Right: nozzle after pressing and drilling of exit pathway.

Note the outside corners of the nozzle are still square. Careful hand sanding rounds these corners (represented by dotted lines) so the flame does not sit on a radially-large surface.

The specimens are partially sintered at 800°C for 4 hrs using a heating rate and cooling rate of 5 °C min<sup>-1</sup> in a digitally controlled Carbolite RHF 1500 furnace with SiC heating elements, shown in Figure 3.6. Partial sintering hardens the material but also allows an opportunity for machining the ceramic. The exit diameter (~ 0.4 mm) is drilled and the tip of the outer shell is sanded to form a

rounded tip. The specimens are then fully sintered at 1475°C for 4 hrs. During this process the specimens decrease in size, approximately 17% less than the original diameter. The ceramic particles exhibit "necking" or bridging between surfaces of adjacent particles, creating a denser overall nozzle. After full sintering no machining is possible for the ceramic nozzle. The final outer diameter of the nozzle is ~8.5 mm.

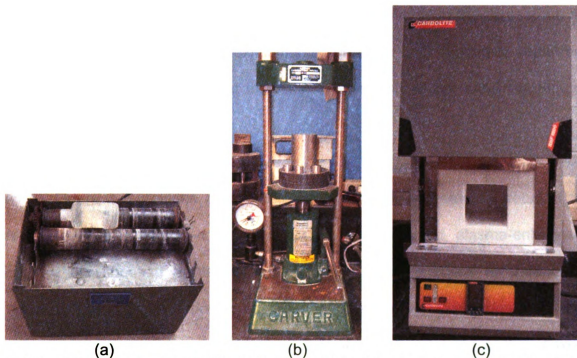


Figure 3.6 Photographs of: (a) tumbler used for mixing powders and for shaping graphite, (b) axial press used for pressing powder in the die, and (c) digitally controlled furnace used for sintering specimens.

Several nozzles have been fabricated. The nature of the fabrication process does not produce identical nozzles; each nozzle may be slightly different due to graphite shifting during pressing. Therefore, the best designs (axially aligned convergence path) are chosen for experimental analysis. The nozzle fits

snug onto the end of the inner conductor and epoxy glue is used as a sealer to prevent gas leakage. A photograph of a ceramic nozzle attached to the torch is shown in Figure 3.4.

An optional step in the manufacturing process of the ceramic nozzle includes gold coating or sputtering of the ceramic's outer surface. The ceramic seems to absorb the microwaves that the flame should absorb. Therefore, sputtering the ceramic nozzle with a metal (gold in this case because of its high temperature endurance) cause the microwaves to converge in the flame zone at the exit of the nozzle. An approximately 20  $\mu\text{m}$ -thick gold coating is sputtered onto the surface using a sputter machine. The ceramic nozzle shown in Figure 3.4 is sputtered with gold.

### **3.2.2 Electrical network and cavity**

Figure 3.7 provides a schematic of the overall experimental setup. The torch operates in plasma-only, combustion-only, and hybrid, plasma-enhanced combustion modes. For plasma production, power is supplied by 2.45 GHz microwave energy. The power absorbed by the system is measured by the difference between incident and reflected power, and is defined at the coaxial input line termination of the PTB. Both incident and reflected power are measured by 50-dB and 30-dB directional couplers, respectively, and are read using HP 435A power meters connected to HP 8481A thermistor power sensors. The reflected signal is fed into a 50-ohm matched load or dummy load (coaxial resistor model 8201).

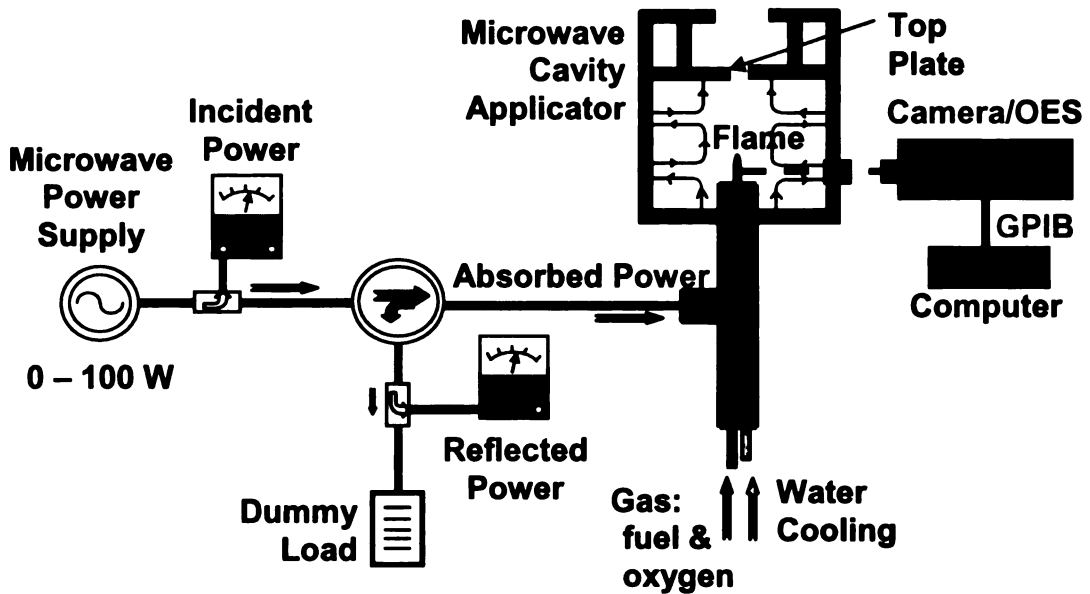


Figure 3.7 Overall experimental setup, including electrical circuit, torch and cavity, gas system, and diagnostic setup [3].

The microwave input power is side-fed into the torch applicator. The system is optimally tuned by repositioning the torch so the reflected power reads zero. Therefore, under these conditions, the incident power equals the power absorbed inside the cavity. The outer conductor and the inner conductor are independently adjustable. Tuning is also available by moving the top plate of the cavity in the vertical direction (see Figure 3.8). The coaxial inner and outer brass conductors allow an electric field to form in the pattern of a  $TM_{012}$  (transverse magnetic) mode inside the cavity (also shown in Figure 3.8) [18]. As a result of optimal tuning, the nozzle tip is positioned so the flame burns in a concentrated area of the electric field while absorbing microwaves. The cavity is sealed for safety to eliminate microwave radiation to the environment. The two viewing windows are covered with metal screening.

Figure 3.8 shows a schematic of the torch inside the cavity. The torch is placed vertically inside the cavity and held in place by finger stock. The cylindrical cavity is 7 inches (17.78 cm) in diameter, with a maximum height of 23 cm. The optimal operating height for this project's experiments is 14.2 cm. Eleven millimeters of the outer conductor is inside the cavity and an additional 7 mm of the inner conductor is also inside the cavity, as shown in Figure 3.8. However, constant tuning of the torch/cavity is necessary for optimal interaction of microwaves and flame; as a result, these dimensions are not always exact for optimized interaction (i.e. zero reflected power). This inconsistency is caused by varying flame size, power input, and power-meter drifting.

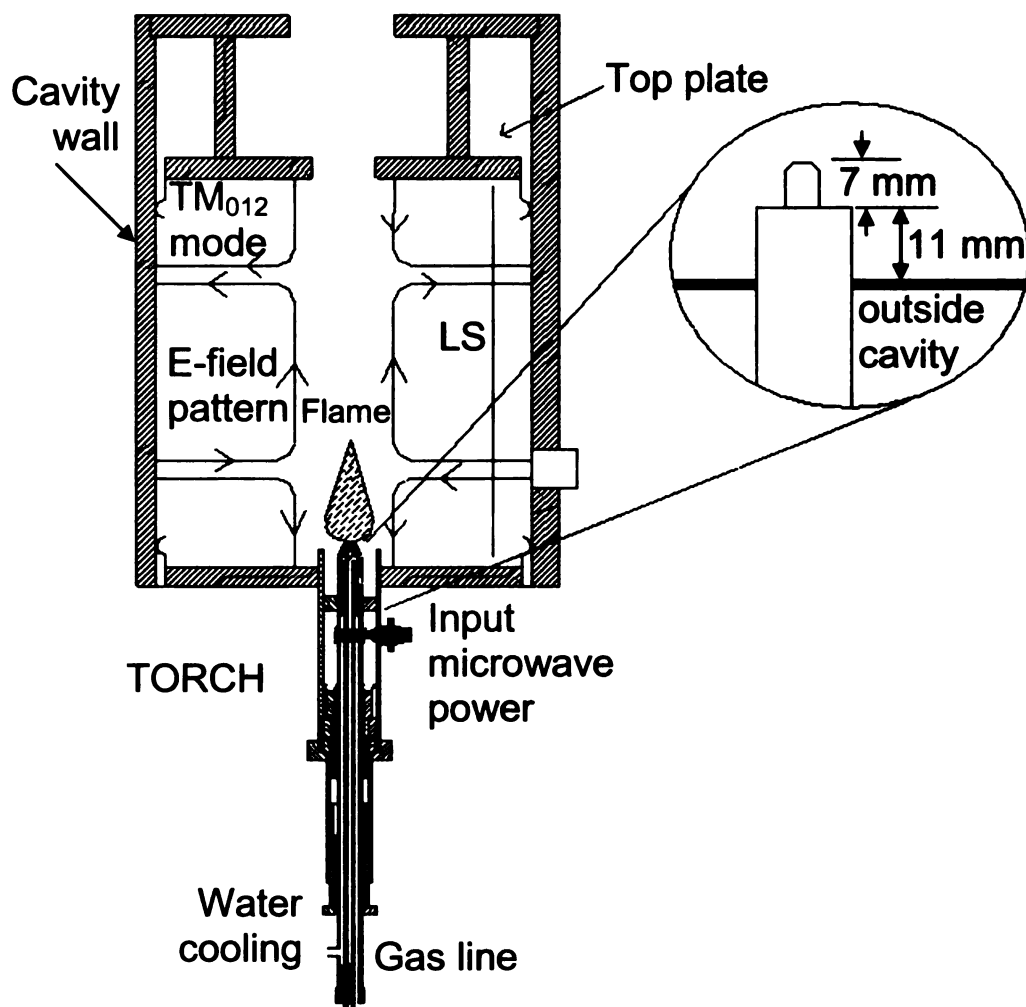


Figure 3.8 PTB and microwave cavity setup, including details of the cavity and the electrical field pattern and wave modes. The torch is placed vertically in the cavity and tuned so the flame interacts with the microwaves, creating a plasma-enhanced hybrid flame. The dimensions of the cavity-penetrated torch are given.

### 3.2.3 Gas system

The gases used for combustion are methane ( $\text{CH}_4$ ) and oxygen ( $\text{O}_2$ ). Methane in  $\text{O}_2$  produces a relatively high theoretical adiabatic flame temperature ( $T_{\text{ab}} \approx 3000 \text{ K}$ ), and yet is safer than hydrogen. It is readily available as “house gas” in the lab. Oxygen, as opposed to air, is used to produce a hotter, more

concentrated flame. The fuel and oxygen are premixed approximately 3 ft. before the nozzle exit plane.

The gas flow is controlled by MKS digital mass flow controllers (MFC). The MFCs are calibrated for each type of gas, and the readout is  $\pm 0.001$  sccm accurate. A schematic of the gas system is shown in Figure 3.9. Gas flows from pressurized tanks to the MFCs through 1/4" flexible metal gas lines using VCR connectors.

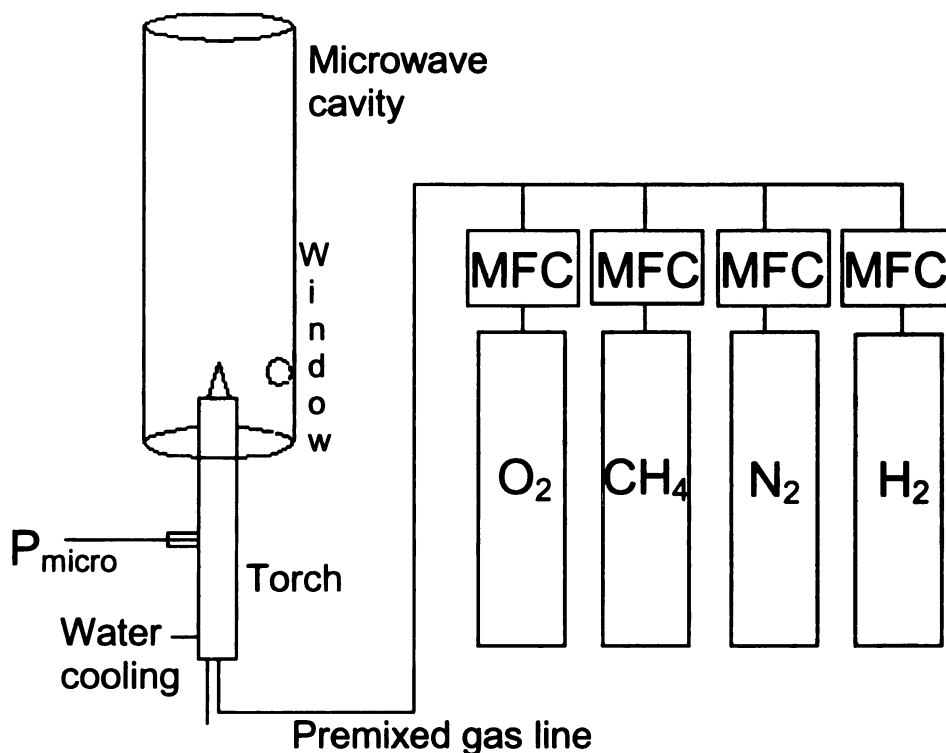


Figure 3.9 Schematic of the gas setup. Gas flows from the compressed tank, through MFCs. It is then premixed before entering the torch. Methane (CH<sub>4</sub>) and oxygen (O<sub>2</sub>) are the primary gases used in the experiments. The microwave power is fed through the side of the torch applicator (P<sub>micro</sub>) and the water cooling lines are also shown.

The gases are mixed downstream of the MFCs where a single 1/4" plastic tube replaces the multiple gas lines. This single gas line is fitted to a 1/16" plastic tube which is connected using epoxy glue to the torch gas inlet (1/16" brass tube) at the base. Gas then flows through the inner conductor to the nozzle and is ignited at the exit of the nozzle using a standard butane lighter. Flow rates from the nozzle range from 15 sccm to 309 sccm (2 m/s - 41 m/s) at the nozzle exit for the 0.4 mm-diameter brass nozzle. Reynolds numbers range from 1 to 50, using a constant O<sub>2</sub> kinematic viscosity of 4 cm<sup>2</sup>/s (value interpolated at 2000 K). Table 3.2 lists the maximum flow rates in volumetric units (sccm) and length units (m/s) for each nozzle type. The ceramic nozzle allows a slightly higher maximum flow rate than the brass nozzle of the same diameter. This is most likely due to stand-off and temperature gradients between the flame and the nozzle.

Table 3.2 Nozzle flow limits. Maximum flow rates for each type of nozzle, in sccm and m/s. Note the ceramic nozzle allows a higher maximum flow rate than the brass nozzle with the same diameter.

<b>Nozzle Type</b>	<b>Brass 0.2mm diameter</b>	<b>Brass 0.4mm diameter</b>	<b>Ceramic 0.4mm diameter</b>
<b>Max Total Flow Rates (sccm or m/s)</b>	75,10	309,41	321,43

### 3.3 Diagnostics and measurement techniques

Experimental techniques used to measure temperature and diagnose the hybrid flame/discharge include: 1) optical emission spectroscopy (OES), used for identifying species and for calculating average rotational temperatures; 2) an infrared (IR) camera, used to examine *relative* temperature values and contours;

and 3) a type K thermocouple with a data acquisition system used to find local temperatures across the flame. The first two methods are most useful for the hybrid experiments because they do not perturb the flame since there is no physical contact. Even though a thermocouple is useful for obtaining point temperature measurements, it interferes with the electric field created by the microwave system. The cavity has two windows that are used for viewing and diagnostics.

### **3.3.1 Optical emission spectroscopy (OES)**

OES is used to measure and analyze the photons or light emitted by the flame/discharge. Its primary function for this project is to calculate the gas temperature of a particular gas-phase species, nitrogen and carbon rotational temperatures in this case, which has been performed in a number of previous experiments [21,22,23,24]. The rotational temperature is essentially a measure of the energetic level of the molecule at which all rotational modes of the molecule are fully engaged. The theory of gas kinetic temperature is explained in Chapter 4. This temperature is a line-of-sight, average temperature. Flame species can also be identified using OES since different atoms and molecules emit unique wavelengths in the spectrum; however, a quantitative value (i.e. emission intensity) is not known from this spectrometer.

The McPherson Model 216.5, 0.5 meter, f/8.7, plane grating monochromator is the OES system used. The operating wavelength range is 1050 Å – 5000 Å, from a grating of 2400 grooves/mm. A schematic of the setup is shown in Figure 3.10. Light is emitted from the flame/discharge and focused by

a biconvex lens (focal length of 5 cm) into the spectrometer. The adjustable entrance slit is set to a width of 50  $\mu\text{m}$ .

The monochromator diffracts the incoming light. Since the angle of diffraction varies with wavelength, only specific wavelengths exit and are measured. The monochromator is manually set to a specific wavelength by rotating the diffraction grating about the axis at a specific angle. The signal of species present (light based on wavelength) is amplified by a photomultiplier and read by the picoammeter to certify that ample signal is being captured. The system is covered by a black cloth to reduce any external light signal, thus enhancing the signal-to-noise ratio.

The spectrometer is connected to a computer by a GPIB (general purpose interface bus) cable and data is collected from a Quick Basic program written by Jayakumaran Sivagnaname [22] to extract wavelengths of various flame/discharge species.

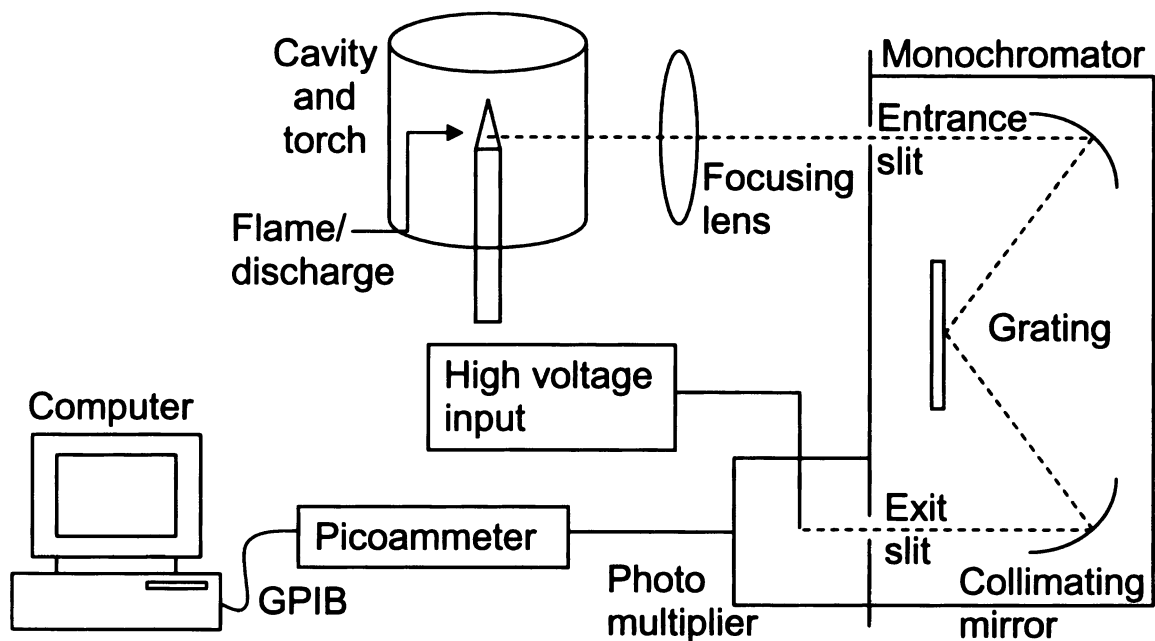


Figure 3.10 Schematic of OES system. Light is emitted from discharge, analyzed in the monochromator, and collected and organized in the computer.

The system (particularly the torch and lens) is aligned so a maximum signal is fed into the entrance slit. The entire image of the flame is focused through the lens, supplying data for an average overall flame temperature. Rotational temperatures calculated from the OES method come from  $C_2$  and  $N_2$  emissions.

### 3.3.2 Infrared camera

Infrared (IR) cameras are useful for nonintrusively measuring temperatures without directly contacting the sample (i.e. flame), unlike intrusive thermocouples that can cause flame perturbations and conduct heat away from the flame. A major obstacle or limitation of the IR temperature analysis, however, is the inability to measure the flame while inside the cavity. The cavity's viewing window is protected with a metal screen, to prevent microwave leakage. The

camera cannot bypass this; because it measures the first object in sight, the cooler metal screen is detected rather than the flame inside the cavity.

A metal stand or platform was built to prop the torch in either the vertical or horizontal direction, for operation outside the cavity. With the torch in an open, unprotected atmosphere, the disadvantage is it cannot be optimally tuned to couple the microwaves with the flame due to leakage. IR measurements were collected from the flame while the torch was outside the cavity.

The camera measures the radiation an object emits, since an object, not at absolute zero temperature, will always emit or absorb energy in the form of electromagnetic radiation. A blackbody, the ideal object with an emissivity ( $\epsilon$ ) of unity, absorbs and emits energy with no reflection. Examples include the sun, a candle flame, and even the flame of a welding torch! Even though torch flames have almost identical properties and characteristics as the flame used in this research, the process for measuring temperature with the IR camera is not so simple ( $\epsilon \neq 1$ ). Because there are hot gases surrounding the flame, the emissivity is no longer unity; it is a function of temperature,  $\epsilon(T)$ , and in addition the temperature varies with location. Thus, IR measurements of gas temperatures are much more complicated than surface temperature measurements.

The Stefan-Boltzmann law, defined in Equation (3.1) below, is used to measure the energy,  $R(T)$ , emitted from a surface relative to a black body, where the energy is a function of temperature and proportionally related to the Stefan-Boltzmann constant,  $\sigma_{SB}$ , defined in Equation (3.2).

$$R(T) = \epsilon \sigma_{SB} T^4 \frac{W}{m^2} \quad (3.1)$$

$$\sigma_{SB} = \frac{2\pi^5 k_B^4}{15h^3 c^2} = 5.67 \times 10^{-8} \frac{W}{m^2 K^4} \quad (3.2)$$

The Stefan-Boltzmann constant is defined as a combination of three other universal constants, the Boltzmann constant,  $k_B$ , Planck's constant,  $h$ , and the speed of light,  $c$  [25].

IR detectors are commonly used to measure temperature because for objects at temperatures of 10-5000 K, the radiation predominantly occurs between wavelengths of 0.2-500  $\mu\text{m}$  in the IR spectrum. IR cameras monitor the temperature from an array of IR sensors, and each sensor represents a pixel in an acquired thermal image [26].

The IR camera used for this research comes from Mid-range Merlin from Indigo Systems Company, a division of Flear International. It has interchangeable 25 mm and 50 mm lenses, has focal length adapters for distant viewing, and contains filters used for higher temperatures. Windows 2000 and Thermagram make up the computer's operating system and software. Further specifications are available at <http://www.indigosystems.com/product/merlin.html>.

The camera uses a cooled InSb detector array and is designed for use with 3-5  $\mu\text{m}$  wavelengths, corresponding to temperatures of approximately 273-1000 K. The temperatures of the flame/discharge studied in this project produce a temperature beyond that range (2000-3000 K); therefore, only *relative*

temperatures are extracted from the analysis, used to compare combustion-only and hybrid flames. Temperature contours throughout the flame body are also obtained.

### 3.3.3 Thermocouple

A type K thermocouple is used to measure flame temperature (combustion only). Type K Chromel-Alumel thermocouples are rated for a long range capacity of 173-1643 K. As mentioned previously, combustion produces a much hotter flame than the thermocouple is capable of measuring. Therefore, the solution to the transient heat conduction equation, assuming the lumped heat capacity method (Biot number < 0.1), was used to calculate temperature based on time-step iterations, and can be seen in Equation (3.3) below. Here  $T(t)$  is the temperature as a function of time,  $T_0$  is the initial temperature (room temperature in this case),  $T_S$  is the surface temperature,  $h$  is the heat transfer coefficient,  $A$  is the cross-sectional area,  $\rho$  is the density,  $c_p$  is the specific heat, and  $V$  is the volume, all with respect to the thermocouple material or junction.

$$\frac{T(t) - T_S}{T_0 - T_S} = \exp\{-(hA / \rho c_p V)t\} \quad (3.3)$$

The thermocouple is welded together to form a spherical junction. It must be noted that the junction is not shielded (may account for inaccuracies in results). Because the sphere is so small (1.7 mm diameter), the lumped capacity method is implemented. The heat transfer coefficient is calculated based on the Whitaker Nusselt ( $Nu$ ) number correlation for a sphere, seen in Equation (3.4)

and a general definition in Equation (3.5) below. This correlation is valid for Reynolds numbers between 3.5 and  $7.6 \times 10^4$  and Prandtl numbers ranging from 0.71 to 380 [25]. The Reynolds number is denoted by  $Re$ , where  $Re = Ud/\nu$  and  $U$  is flow velocity,  $d$  is diameter, and  $\nu$  is kinematic viscosity. The Prandtl number,  $Pr$ , is defined as  $Pr = \nu/\alpha$  where  $\alpha$  is thermal diffusivity. Dynamic viscosity,  $\mu$ , is the viscosity of the fluid at  $T_\infty$ , and  $\mu_s$  is the dynamic viscosity of the fluid at the surface evaluated at the film temperature,  $T_f$ , the average temperature of the solid and fluid,  $L$  is the characteristic length, and  $k_f$  is the thermal conductivity of the fluid ( $O_2$  gas in this case). All parameters, except  $\mu_s$ , are evaluated at  $T_\infty$ .

$$Nu_{avg} = 2 + (0.4 Re^{0.5} + 0.06 Re^{2/3}) Pr^{0.4} (\mu / \mu_s)^{0.25} \quad (3.4)$$

$$Nu_{avg} = \frac{hL}{k_f} \quad (3.5)$$

An Excel spreadsheet is created with known constants and used to calculate the temperature for a 0.5-second time step. Reynolds numbers ranged from 3-375, based on a constant 3.5 m/s flame speed (calculated from cone angle) and temperature-dependent  $O_2$  kinematic viscosities. This spreadsheet is found in Appendix A.

A motorized device built enables the thermocouple to sweep through the flame at a constant speed, while the data acquisition system reads the voltage difference and converts to temperature. A Hewlett Packard (model # 3852A) data acquisition system/control unit, connected to a computer with a GPIB cable, is used. The time delay for this system is 0.1 s. Photographs of the control unit and motorized device are shown in Figure 3.11.

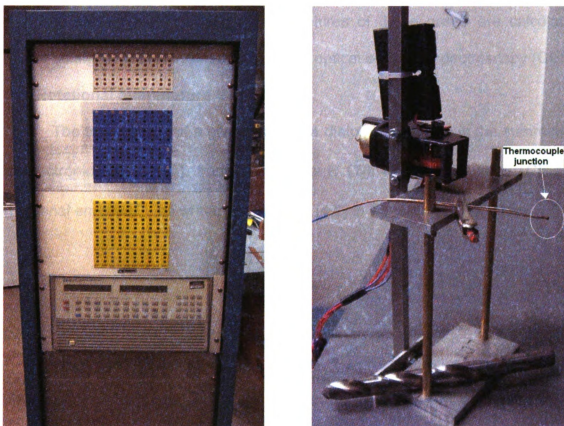


Figure 3.11 Left: photograph of the data acquisition system used to measure temperature with a Type K thermocouple. System is connected to a computer with a GPIB cable. Right: device built to sweep thermocouple through flame at a constant speed. Note the spherical thermocouple junction.

## Chapter 4

# Theory and Background of Gas Rotational Temperatures

### 4.1 Introduction

Flame/discharge temperatures can be approximated by measuring gas temperatures. The gas temperatures are calculated by measuring the rotational energy levels of various molecules present in the flame/discharge. The homonuclear, diatomic molecules that are measured in this study are nitrogen ( $N_2$ ) and carbon ( $C_2$ ). Rotational temperatures of these gases are calculated based on signal (wavelength) measured by optical emission spectroscopy (OES).

### 4.2 Rotational temperature theory

The total energy of a given state of a diatomic molecule is the summation of electronic energy ( $T_e$ ), translational energy ( $T_t$ ), vibrational energy ( $G$ ), and rotational energy ( $F$ ), as written in Equation (4.1) in wave-number units.

$$T = T_e + T_t + G + F \quad (4.1)$$

In general, rotational energy changes in a given vibrational and electronic state are small compared with the thermal translational energy, therefore making  $F$  a small number. Conversely, gas molecule collisions produce changes in the vibrational or electrical quantum numbers much less frequently than in rotational quantum numbers precisely because the rotational energies are lower than the others and changes are easier to excite [27]. The rotational temperature is a reliable measure of the gas kinetic temperature because the rotational population

distribution in a sufficiently long-lived vibrational state has a Boltzmann distribution [27,28,29,22].

The rotational energy listed in Equation (4.1) is defined in Equation (4.2) below in terms of  $J$ , the rotational quantum number which takes the values 1, 2, 3, ...,  $B_v$ , the rigid rotator rotational spacing or rotation radius, and  $D_v$ , the first anharmonic correction to the rotational spacing.

$$F = B_v J(J+1) - D_v J^2(J+1)^2 + \dots \quad (4.2)$$

In addition, there are nonrigid rotator corrections to both  $B_v$  and  $D_v$ . These corrections are defined in Equations (4.3) and (4.4) below, where  $v$  is the vibrational frequency,  $B_e$  and  $D_e$  are constants that correspond to the equilibrium separation, and  $\alpha_e$  and  $\beta_e$  are the first anharmonic corrections. Constants for the first order rotational energy are listed in Table 4.1 below for  $N_2$  and  $C_2$  [27, 22].

$$B_v = B_e - \alpha_e \left(v + \frac{1}{2}\right) + \dots \quad (4.3)$$

$$D_v = D_e + \beta_e \left(v + \frac{1}{2}\right) + \dots \quad (4.4)$$

Table 4.1 Rotational constants for the electronic states of nitrogen and carbon.

State	$B_e$	$\alpha_e$
$N_2$ ( $C^3P_u - B^3P_g$ )	1.8259	0.0197
$C_2$ ( $d^3P_g - a^3P_u$ )	1.7527	0.01608

Each molecule is denoted by a specific quantum state. For this research the Second Positive System ( $C^3P_u \rightarrow B^3P_g$ ) is used for  $N_2$  values and the Swan System ( $d^3P_g \leftrightarrow a^3P_u$ ) is used for  $C_2$  values. These systems are now explained. The upper (u) and lower (g) states may have different electronic angular momenta,  $\Lambda$ . Therefore, two or three series of lines or branches may appear: the P, Q, and R branches. Shown in Figure 4.1 are these three branches, which result from transitions in vibrational and rotational energy levels.

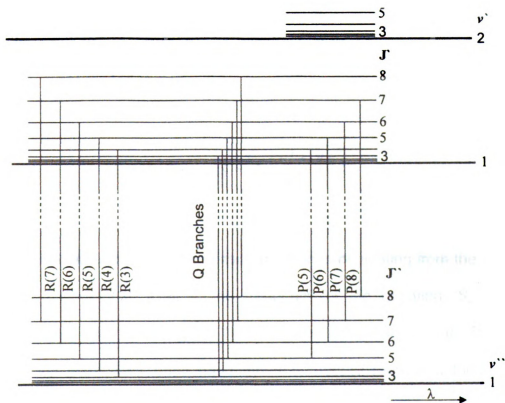


Figure 4.1 Energy level diagram for a band with P, Q, and R branches, relative to wavelength ( $\lambda$ ), rotational energy levels ( $J$ ), and vibrational levels ( $v$ ) [27].

For both N<sub>2</sub> and C<sub>2</sub>,  $\Delta\Lambda = 0$  because the angular momentum at both the upper and lower electronic states is zero; therefore, the  $\Delta J = 0$  transition is forbidden and it follows that  $\Delta J = \pm 1$ . The R branch is associated with  $\Delta J = +1$  and the P branch is associated with  $\Delta J = -1$ . The Q branch is not present for N<sub>2</sub> and C<sub>2</sub> because  $\Delta\Lambda = 0$ . It is important to note, however, that all branches may be present for a specific electronic transition with a different angular momentum, as shown in Figure 4.1 [27].

Generally, emission methods, as opposed to absorption methods, are suited for measuring the temperature in a Boltzmann distribution. The relative emission intensity ( $I$ ) of rotational lines is described as Equation (4.5) by [30]. This intensity is not related to size.

$$I = K\nu^4 S_{J',J''} \exp\left(-\frac{B_{\nu'} J'(J'+1)hc}{kT_r}\right) \quad (4.5)$$

The intensity is defined by:  $K$ , the constant for all lines originating from the same electronic and vibrational level;  $\nu$ , the frequency of the radiation;  $S_{J',J''}$ , the appropriate Hönl-London factor;  $B_{\nu'}$ , the molecular rotational constant for the upper vibrational level;  $J$ , the rotational quantum number ( $J'$  represents the upper energy level and  $J''$  represents the lower level) ;  $h$ , Planck's constant;  $c$ , the speed of light;  $k$ , the Boltzmann constant; and  $T_r$ , the rotational temperature.

It is seen from Equation (4.5) that the intensity is proportional to the frequency,  $\nu$ , to the fourth power and also to the exponential ratio of rotational temperature,  $T_r$ . As the wavelength of an emitted species decreases, the

intensity increases to the fourth power; frequency is defined as the speed of light divided by wavelength,  $\nu = c/\lambda$ . As temperature increases, so does the intensity exponentially.

The Hönl-London factor describes the line strength of rotational spectra, and it is dependent on  $J$ . The Hönl-London formula is defined in Equation (4.6) for emission associated with the R branch, where  $\Delta\Lambda = 0$ , [27].

$$S = \frac{(J'+\Lambda'+1)(J'-\Lambda'+1)}{J'+1} \quad (4.6)$$

Since  $\Delta\Lambda = 0$ , Equation (4.6) reduces to Equation (4.7) below.

$$S = J'+1 \quad (4.7)$$

The experimental data is fitted to the expression  $I \sim S_{JJ'} \exp\{-B_v J'(J'+1)hc/(kT_r)\}$ , using several (11 or more) R-branch emission lines to determine the rotational temperature,  $T_r$ . The plot of  $\ln(I/S)$  is a linear function of the upper rotational energy for the diatomic molecules used in this study. Chapter 3 describes the experimental procedure for measuring the spectra of various flame/discharge species, which are used for the temperature calculation. Figure 4.2 pictorially shows how the light signal is emitted from the flame/discharge, and then focused through a lens into the spectrometer.

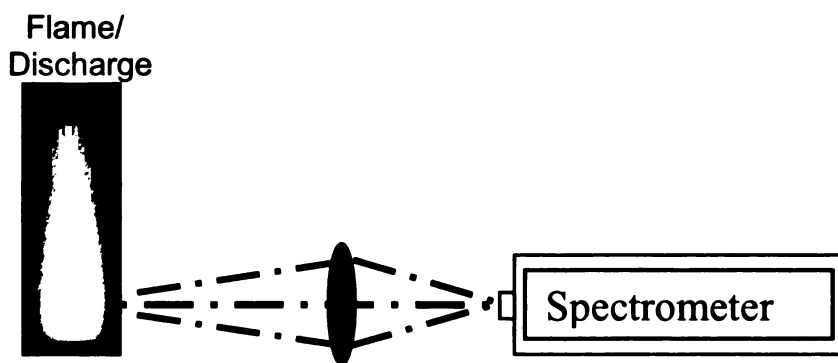


Figure 4.2 Laboratory process for temperature calculations: light is emitted from the flame/discharge and focused by a lens into the spectrometer, where intensities and wavelengths are recorded.

### 4.3 Gas temperature of $N_2$

Rotational temperatures are first calculated based on the  $N_2$  spectrum, since this molecule has been extensively measured [21]. Nitrogen is measured in two different sources. In the first set of experiments, only methane and oxygen serve as the feed gases;  $N_2$  is detected from the atmosphere (air) as the flame/discharge reacts. In a second set of experiments, a small amount ( $\sim 2\%$ ) of  $N_2$  is fed into the incoming methane and oxygen streams. Parameters that are varied in each experiment include microwave input power and gas flow rate. The system currently operates at atmospheric pressure.

The Second Positive System (SPS) is used to determine the  $N_2$  rotational temperatures. The SPS describes the energy level transition from  $C^3P_u$  to  $B^3P_g$ . Figure 4.3 is a plot of an  $N_2$  spectrum, measured in the laboratory, identifying 11 emission lines ( $R_{20} - R_{30}$ ) in the spectrum range  $3758 \text{ \AA} - 3783 \text{ \AA}$  of the (2,0) transition in the SPS.

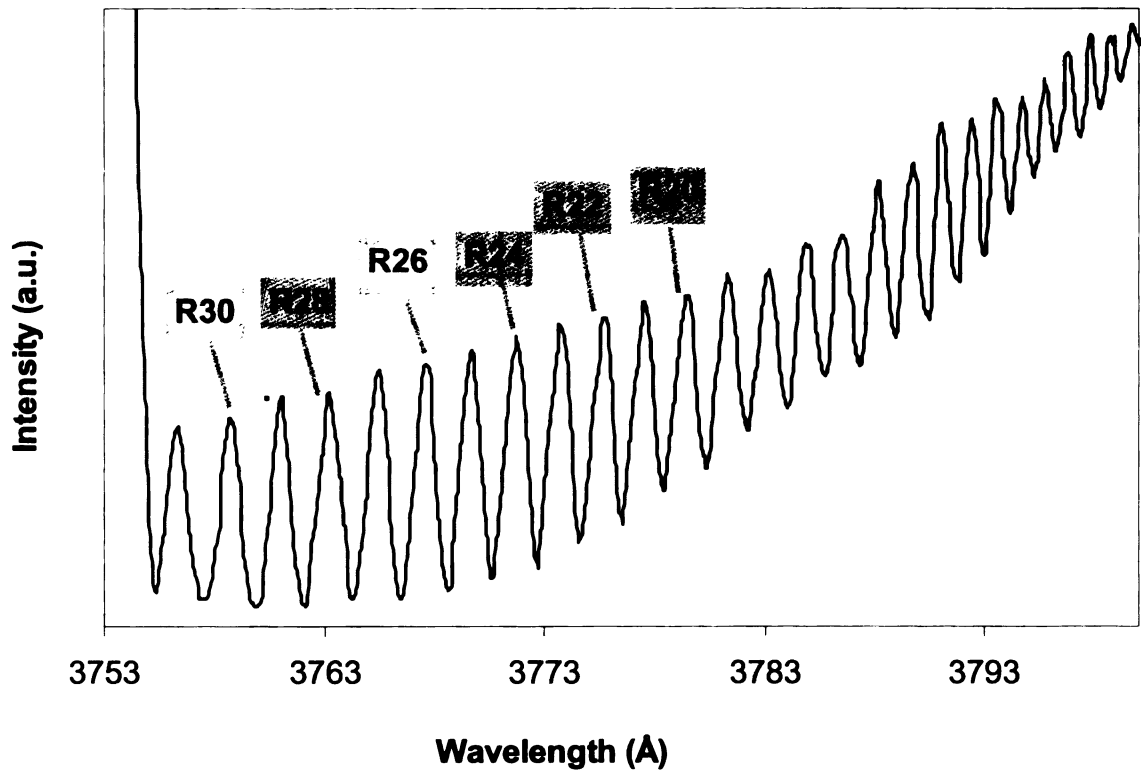


Figure 4.3 Plot of intensity (or current since the units are arbitrary) versus wavelength for the  $N_2$  spectrum, commonly used for rotational temperature calculations.  $R_{20} - R_{30}$  list the order of the rotational bands.

Table 4.2 provides values used in the rotational temperature calculations. These values include the rotational lines/bands ( $R_{20} - R_{30}$ ), wavelengths recorded from text (the wavelengths gathered from the experiments of this thesis are compared to book values to ensure accuracy), relative upper-level energies calculated from Equation (4.2), and the Hönl-London factor calculated from the corresponding rotational band.

Table 4.2 Values used for the N<sub>2</sub> rotational temperature calculations for the R branch of the (2,0) SPS.

Rotational Line	Wavelength (Å)	Relative upper-level energy (cm <sup>-1</sup> )	S
R20	3780.44	837.76	19.80
R21	3778.58	917.42	20.81
R22	3776.66	1000.67	21.82
R23	3774.68	1087.51	22.83
R24	3772.64	1177.95	23.83
R25	3770.53	1271.97	24.84
R26	3768.37	1369.57	25.85
R27	3766.14	1470.76	26.85
R28	3763.86	1575.51	27.86
R29	3761.51	1683.84	28.86
R30	3759.11	1795.74	29.87

The natural log of the ratio, I/S, is plotted against the relative upper-level energy, and the gradient of a linearly-fitted line is used to calculate the rotational temperature in Equation (4.5). Figure 4.4 displays an example of a Boltzmann plot for the R<sub>20</sub> – R<sub>30</sub> bands. This plot is created from a set of experimental flame/discharge data with a methane/oxygen flow rate of 80/160 sccm combined with 40 W microwave input power. Rotational excitation N<sub>2</sub> temperatures are calculated even though N<sub>2</sub> is not present in the gas flow; the flame reacts with N<sub>2</sub> found in the surrounding air, similar to a diffusion flame.

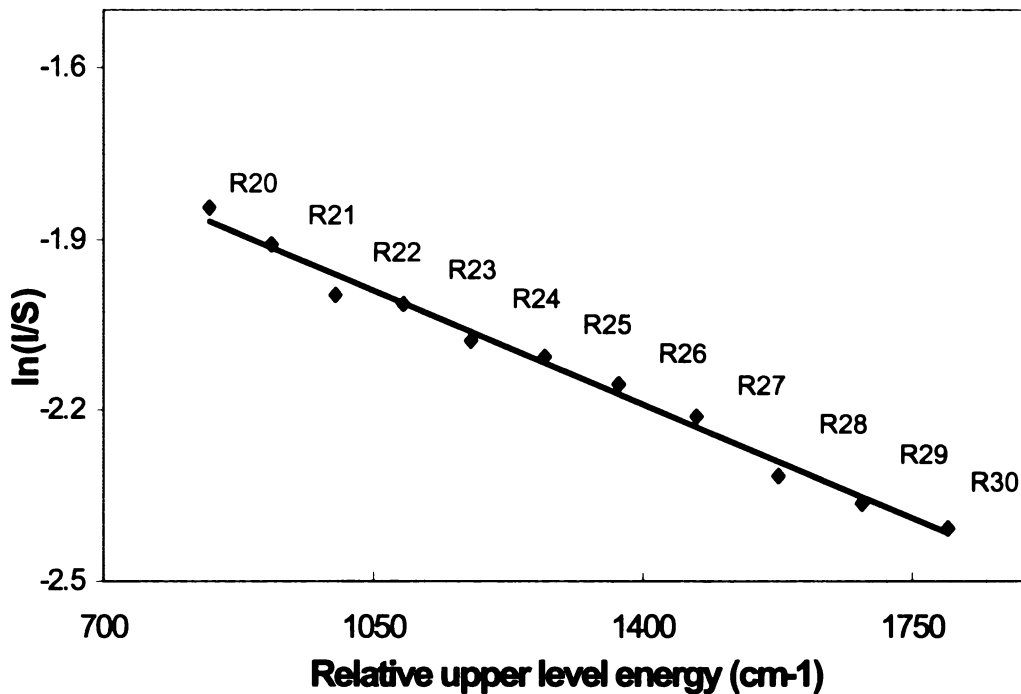


Figure 4.4 Boltzmann plot for the bands R<sub>20</sub> – R<sub>30</sub> of the N<sub>2</sub> spectrum.

The accuracy of rotational temperature is within  $\pm 100$  K, as estimated from the reproducibility of the data obtained.

#### 4.4 Gas temperature of C<sub>2</sub>

Rotational temperatures of C<sub>2</sub> are calculated in a fashion similar to N<sub>2</sub> rotational temperatures. The carbon source is methane, CH<sub>4</sub>, the fuel used for combustion in this thesis. The light emitted from the breakdown of CH<sub>4</sub> eventually to C<sub>2</sub> and the subsequent C<sub>2</sub> excitation is processed in the spectrometer and the wavelengths and intensities of the C<sub>2</sub> spectrum are extracted and plotted.

The Swan System ( $d^3p_g \leftrightarrow a^3p_u$ ) is used for calculating the C<sub>2</sub> rotational temperatures [24]. The emission intensity is measured using the (0,0) band head, with an intensity of 513 nm. Figure 4.5 is a plot of a C<sub>2</sub> spectrum, identifying 21

emission lines ( $R_{25} - R_{45}$ ) in the spectrum range 5028 Å – 5089 Å of the (0,0) transition in the Swan System.

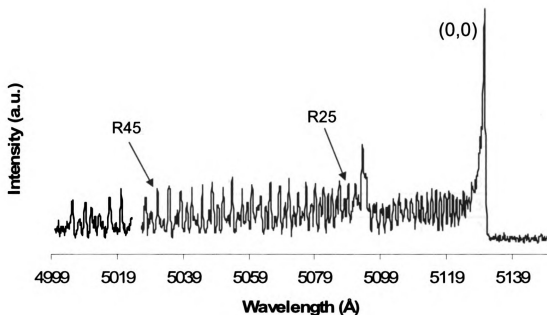


Figure 4.5  $C_2$  spectrum of a Swan System, identifying the bands  $R_{25} - R_{45}$ .

Values used to calculate  $C_2$  rotational temperatures are listed in Table 4.3 and are obtained as described in Section 4.3 for  $N_2$  rotational temperature. Note the difference in the Hönl-London factor, defined previously by Equation (4.6), takes a new definition for the  $C_2$  analysis [24], written in Equation (4.8) below.

$$S = \frac{(J'+1)(J'-1)}{J'} \quad (4.8)$$

Table 4.3 Values used for C<sub>2</sub> rotational temperature calculations for the R branch of the (0,0) Swan System. Note the change in the Hönl-London factor.

Rotational Line	Wavelength (Å)	Relative upper level energy (cm <sup>-1</sup> )	S = (J'+1)(J'-1)/J'
R25	5089	564.40	24.96
R26	5086	609.55	25.96
R27	5084	656.44	26.96
R28	5081	705.07	27.96
R29	5079	755.43	28.97
R30	5076	807.53	29.97
R31	5074	861.36	30.97
R32	5071	916.94	31.97
R33	5068	974.24	32.97
R34	5066	1033.29	33.97
R35	5063	1094.07	34.97
R36	5060	1156.59	35.97
R37	5057	1220.84	36.97
R38	5054	1286.84	37.97
R39	5051	1354.56	38.97
R40	5047	1424.03	39.98
R41	5045	1495.23	40.98
R42	5042	1568.17	41.98
R43	5038	1642.84	42.98
R44	5035	1719.25	43.98
R45	5031	1797.40	44.98

As with the N<sub>2</sub> calculations, the natural logarithm of I/S is plotted against the relative upper-level energy and is linearly fit to extract a rotational temperature from the slope of the line. An example of this plot is shown in Figure 4.6, gathered from experimental data using the ceramic nozzle, having methane/oxygen flow rates of 60/180 sccm, and no microwave power present. This is a pure flame, not a flame/discharge. The uncertainty of the measured gas temperature is approximately 100 K based on reproducibility.

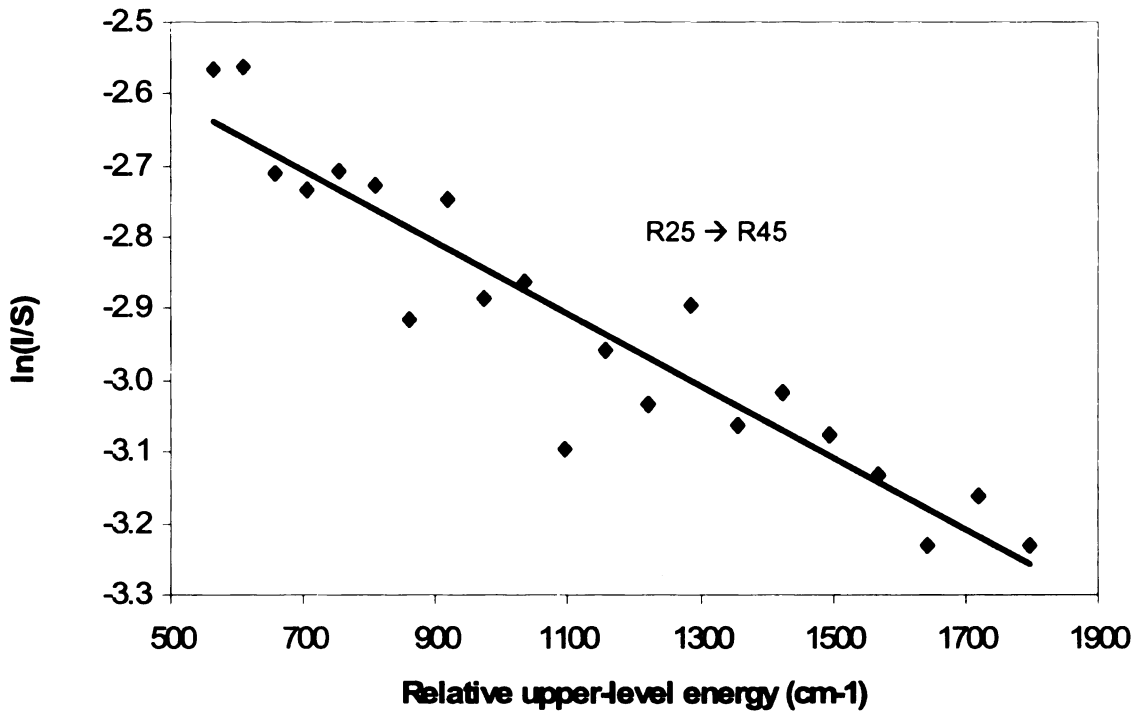


Figure 4.6 Boltzmann plot for the bands R<sub>25</sub> – R<sub>45</sub> of the C<sub>2</sub> spectrum, for the 180/60 sccm O<sub>2</sub>/CH<sub>4</sub> pure flame.

Results from OES measurements of the rotational temperatures for N<sub>2</sub> and C<sub>2</sub> molecules are tabulated and discussed in Chapter 5 of this thesis.

## **Chapter 5**

### **Results and Discussion**

#### **5.1 Introduction**

The results in this thesis are collected primarily from experimental procedures. Much preliminary work was done building an expandable foundation for this research because plasma-enhanced combustion is not a fully developed and clearly understood area of research. The research takes two approaches: 1) studying the fundamental concepts of plasma-enhanced combustion phenomena and understanding the underlying effects of such a hybrid system; and 2) engineering a practical torch/burner to be used in industry.

Results collected and evaluated include flame/discharge photographs, geometric measurements which account for flame speed and power density calculations and non-dimensional power plots, extinction (blow-out) data, species data from OES, and temperature measurements using different methods. Data are collected from both brass and ceramic nozzles; however, focus is on data from the 0.4 mm-diameter brass nozzle. Where the nozzle is not specified, it is safe to assume the 0.4 mm-diameter brass nozzle is used. Images in this thesis are presented in color.

#### **5.2 Flame/discharge photographs**

The torch has gas flow limitations it cannot exceed to produce a flame, depending on which nozzle is used. Table 5.1 lists the maximum total flow rates for three nozzles: 1) 0.2 mm-diameter brass nozzle; 2) 0.4 mm-diameter brass nozzle; and 3) 0.4 mm-diameter ceramic nozzle. These limitations are recorded

based on stoichiometric (2:1 sccm) methane/oxygen flow rates, stoichiometric referring to the ideal combustion process during which a fuel is burned completely. The minimum flow rates are not measurable due to limitations of the mass flow controllers (MFCs) i.e. the flame is maintained at a low flow rate of 18/9 sccm O<sub>2</sub>/CH<sub>4</sub>, and when the rate falls to 9 sccm and below the MFCs do not measure accurately.

Table 5.1 Gas flow limitations for three nozzles with units in sccm and m/s.

<b>Nozzle Type</b>	<b>Brass 0.2mm diameter</b>	<b>Brass 0.4mm diameter</b>	<b>Ceramic 0.4mm diameter</b>
<b>Max Total Flow Rates (sccm or m/s)</b>	75 , 10	309 , 41	321 , 43

Several photographs are taken, using a digital Nikon D70 Outfit camera, of flame configurations using the three nozzles mentioned earlier. Figure 5.1 includes photographs of pure combustion flames with varying flow rates, using the 0.4 mm-diameter brass nozzle. As the O<sub>2</sub> flow rate increases for a fixed fuel rate, the flame decreases in length. The length is increased with a higher overall CH<sub>4</sub> flow rate, but still follows the trend that as O<sub>2</sub> increases, flame length decreases. Table 5.2 lists the flame lengths for each flow rate. The stoichiometric flame parameters are highlighted in the table. As the overall stoichiometric flow rate increases, the flame length also increases from 3.7 cm, to 5.0 cm, and finally to 6.5 cm. As the total flow rate increases by 33% from 200 sccm to 300 sccm, the length increases by 43% from 3.7 cm to 6.5 cm. The flame length increases almost linearly with an increase in total stoichiometric flow rate, yielding a coefficient of determination (R<sup>2</sup> value) of 0.9903. Notice that as the fuel rate

exceeds the  $O_2$  rate, the flame front increases in size. The flame front is the outline of the white inner core of the overall flame. The blue volume beyond the flame front is the heat released from the chemical reaction.

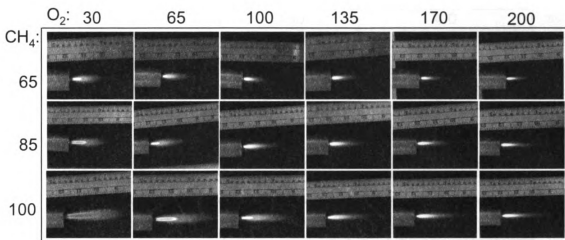


Figure 5.1 Photographs of pure combustion flames with varying flow rates, measured in sccm. The 0.4 mm-diameter brass nozzle is used.

Table 5.2 Lengths of flames with varying flow rates, corresponding to Figure 5.1. The shaded cells highlight stoichiometric flow rates.

Mass flow rate (sccm)		Length of Flame (cm)
Methane (CH <sub>4</sub> )	Oxygen (O <sub>2</sub> )	
65	30	5.0
65	65	4.5
65	100	4.0
65	135	3.7
65	170	3.2
65	200	3.1
85	30	6.5
85	65	6.0
85	100	5.7
85	135	5.2
85	170	5.0
85	200	4.7
100	30	9.6
100	65	8.4
100	100	8.0
100	135	7.5
100	170	7.2
100	200	6.5

Figure 5.2 provides photographs of a pure plasma made from 200 sccm argon (Ar<sub>2</sub>). The plasma discharge is much smaller in length and diameter than a pure combustion flame. The temperature is also much lower than a flame temperature (~1800 K vs. ~3000 K), as will be discussed later in this chapter. Notice that the torch is not confined within the microwave cavity. Microwaves do not escape the torch when the inner conductor is kept inside the outer conductor and the microwave power is held at a relatively low value (10 – 40 W). The plasma discharge, when inside the cavity, can become very long (> 10 cm) when the torch is tuned and the microwave power is increased.

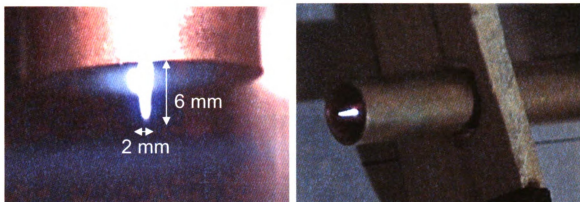


Figure 5.2 Photographs of a pure plasma discharge, with a flow rate of 200 sccm argon and 30 W microwave power. Note that the torch is not confined within the cavity.

Photographs in Figure 5.3 show how a pure combustion flame is affected or altered by the presence of microwaves. A stoichiometric flow of 40/20 sccm  $O_2/CH_4$  is burned as 40 - 100 W microwave power is added, shown in the bottom row of photographs. As 40 W microwave power is added to the flame, the torch is adjusted and tuned inside the microwave-sealed cavity (the metal screen used to prevent microwave leakage from the cavity's window is visible in the photographs) to trigger optimal flame/microwave interaction. The flame transforms into a hybrid discharge as it changes color and increases in size (four times its size from pure combustion to a 100 W-hybrid flame/discharge). The position of this optimal tuning is referred to as the "sweet spot," where also the reflected power of microwaves is zero.

The top row of photographs in Figure 5.3 shows flame/discharges with a flow rate of 40/0 sccm  $O_2/CH_4$  and with 40 - 100 W microwave power. In other words, an oxygen plasma is present. Once the flame transforms from the pure combustion form into a hybrid flame/discharge, the fuel is reduced to zero flow.

The fuel-free flame/discharge is smaller (5 mm shorter in length at 100 W) than that which burns fuel.

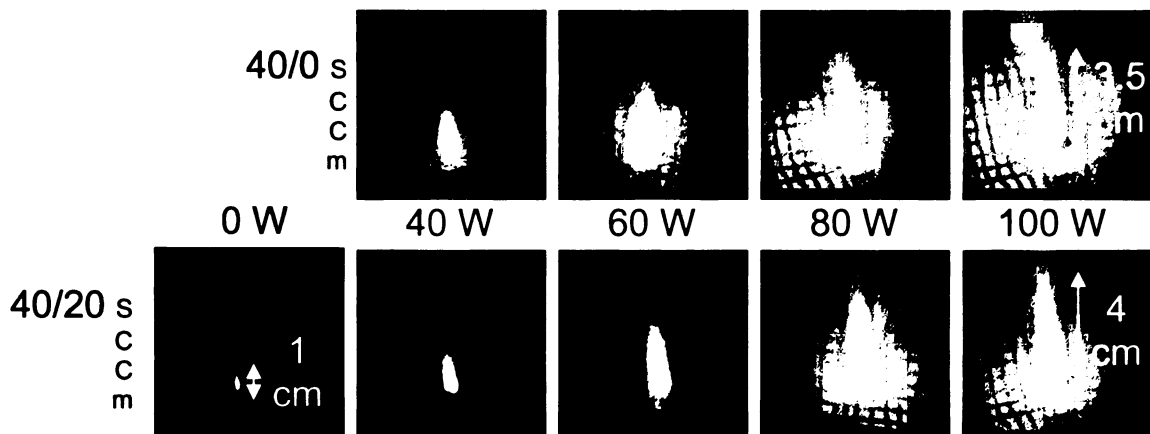


Figure 5.3 Photographs of flame/discharges inside the cavity as 40-100 W microwave power is added. The 0.2 mm-diameter brass nozzle is used. The flow rate for the top set of photos is 40/0 sccm  $O_2/CH_4$ , i.e. no fuel is present. The flow rate for the bottom set is 40/20 sccm  $O_2/CH_4$ , a stoichiometric ratio. Scales are provided for flame dimensions. Camera speed and aperture are 1.6 and 3.5, respectively.

Photographs of a pure combustion flame and microwave-induced flame/discharges formed by a ceramic nozzle are shown in Figures 5.4 and 5.5. The flow rate of the flames in Figure 5.4 is 200/100 sccm  $O_2/CH_4$ , and 20 W, 40 W, and 80 W microwave power is added. The photographs do not show evidence of a plasma-enhanced combustion flame; the color, shape, and size of the original flame are not affected by microwaves even with fine adjustment (zero reflected microwave power), from what the human eye can detect. However, OES measurements show that the flame is indeed altered by microwaves and will be discussed later in this chapter.

The ceramic nozzle may absorb the majority of the microwaves, rather than the flame, or the gases might be excited by the microwaves upstream the nozzle. At this point an explanation is uncertain. Figure 5.5 shows that even though the flame is not physically altered by microwave power, the flame increases in length as the total flow rate increases.

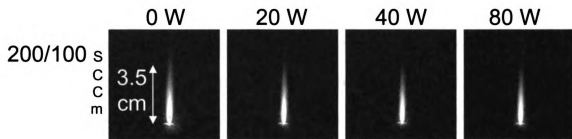


Figure 5.4 Photographs of flame/discharges inside the cavity as microwave power is added, 20-80 W. The 0.4 mm-diameter ceramic nozzle is used. The flow rate is 200/100 sccm  $O_2/CH_4$ , a stoichiometric ratio. A scale is provided for flame dimensions. Camera shutter speed and aperture are 1.6 s and 3.5, respectively.

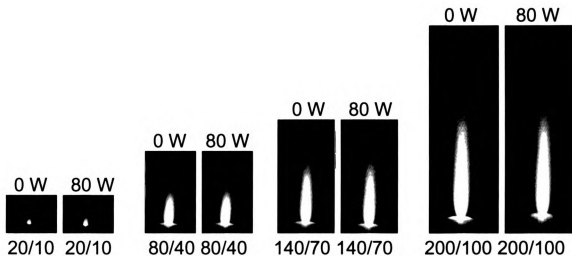


Figure 5.5 Photographs of flame/discharges inside the cavity with a ceramic nozzle comparing 0 W to 80 W of microwave power.

The sets of photographs in Figure 5.6 show very clearly how the microwaves alter a pure combustion flame, formed with the 0.4 mm-diameter brass nozzle. The flow rates are listed in the figure for each set, and a scale is provided to estimate flame/discharge dimensions. It appears that the microwaves start to dominate after 30 – 40 W microwave power is added to the flame.

To further investigate, photographs are taken at 1-Watt increments from 31 W to 40 W, and then again from 39 W down to 33 W, shown in Figure 5.7. As power increases the flame transforms at 38 W; however, as power decreases, a major change does not occur until 35 W. A hysteresis is present. There appears to be a delay in the change of state (transition from hybrid form to combustion form) when the power is decreased. Further theoretical investigation for an explanation of this behavior is advised.

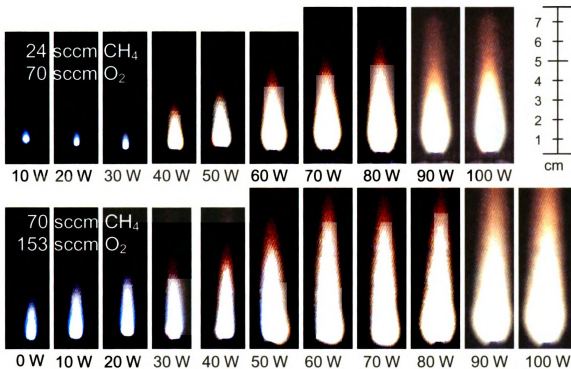


Figure 5.6 Photographs of flame/discharges inside the cavity as microwave power is added, 10-100 W. The 0.4 mm-diameter brass nozzle is used. The flow rate for the top set is 70/24 sccm  $O_2/CH_4$ . The flow rate for the bottom set is 153/70 sccm  $O_2/CH_4$ . A scale is provided for flame dimensions. Camera shutter speed and aperture are 1/30 s and 3.5, respectively.

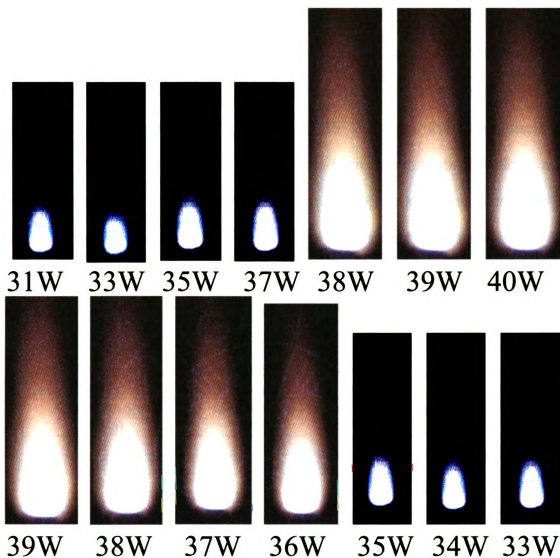


Figure 5.7 Additional photographs from Figure 5.6. The flow rate is 70/24 sccm  $O_2/CH_4$  and all other conditions are the same as listed in Figure 5.6. The top sequence shows the flame/discharge as microwave power increases; the bottom sequence is power decreasing. This intermediate behavior gives rise to a hysteretic affect.

Flame velocity, or flame propagation speed, is calculated from the geometry of a flame. The cone angle,  $\alpha$ , is the angle between the center of the flame and an edge, when the flame is modeled as a two-dimensional cone and assumed axisymmetric. This angle is measured, and along with the flow rate of gases that is measured,  $u$ , these measurements are used to calculate flame

speed,  $S_L$ , as defined in Equation (5.1). Flame speeds are calculated for the flames in Figure 5.7, as the microwave power decreases from 39 W to 33 W, and are listed in Table 5.3. As microwave power decreases, the flame speed also decreases. Significant change occurs at 35 W when the flame/discharge transforms from hybrid form to combustion form. Most probably microwaves excite the species in the combustion process at a higher level and accelerate the radicals/ions at higher rates. Typical book-value flame speeds for an  $O_2/CH_4$  flame are  $\sim 100$  cm/s.

$$S_L = u \sin \alpha \quad (5.1)$$

Table 5.3 Flame speeds calculated for flames shown in Figure 5.7 as power decreases from 39 W to 33 W. Calculations are based on Equation (5.1).

<b>Cone Angle (Deg)</b>	<b>Microwave Power (W)</b>	<b>Flame Speed, <math>S_L</math> (cm/s)</b>
12	39	259
12	38	259
9	37	195
9	36	195
3	35	65
3	34	65
2	33	44

### 5.3 Geometric analysis

Along with flame speeds, deduced from flame geometry are quantities such as power density and non-dimensional power as a function of flame height. Power density is calculated first by modeling the flame/discharge as a cone to calculate a volume; it is defined here as the addition of microwave power and combustion power of a flame/discharge divided by the volume of the corresponding flame/discharge. Combustion power is approximated using the

higher heating value (HHV) tabulated in text for gaseous methane, based on stoichiometric combustion with air, a value of 55,528 kJ/kg, and a CH<sub>4</sub> density of 0.68 kg/m<sup>3</sup> [31]. Values of combustion power in this research range from 10 – 40 W.

Power densities are plotted against non-dimensional power in Figure 5.8 for the two sets of data shown in Figure 5.6. Non-dimensional power is defined as  $P_P/(P_P + P_C)$ , where  $P_P$  is microwave (plasma) power and  $P_C$  is combustion power ( $P_C$  is provided in the figure for each flow rate). With the absence of microwaves, power density is greater for the flame with a lower total flow rate, which is also slightly more fuel-lean. The flame volume is significantly larger for the second set of data (153/70 sccm O<sub>2</sub>/CH<sub>4</sub>).

The power density is greatest just before the flame transforms in size and color, suggesting the flame/discharge of highest intensity is formed when ~ 30 W microwave power interacts with the flame. An intense and highly concentrated discharge is desired, but temperature must also be considered. As microwave power increases, temperature increases, as discussed in Section 5.5.

Figure 5.9 shows how the power (both microwave and combustion) physically alters the flame in terms of geometry. Flame height is plotted against non-dimensional power. An exponential growth in flame height occurs as microwave power is added to the flame, for both sets of data.

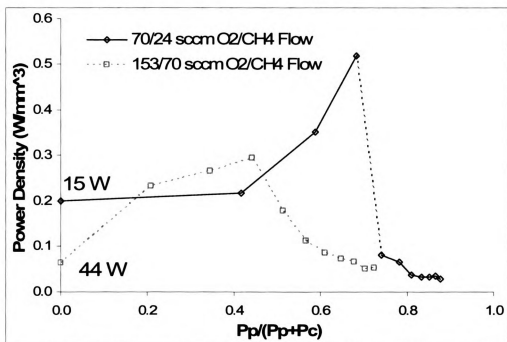


Figure 5.8 Power density as a function of non-dimensional power, evaluated from flame/discharge geometries shown in Figure 5.6, with flow rates of 70/24 sccm O<sub>2</sub>/CH<sub>4</sub> and 153/70 sccm O<sub>2</sub>/CH<sub>4</sub>. The powers of combustion are provided: 15 W for the first flow and 44 W for the second flow.

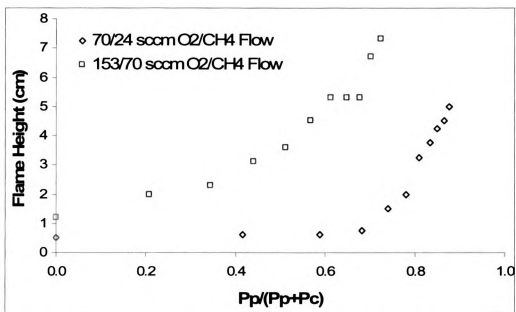


Figure 5.9 Flame height as a function of non-dimensional power, evaluated from flame/discharge geometries, shown in Figure 5.4, with flow rates of 70/24 sccm O<sub>2</sub>/CH<sub>4</sub> and 153/70 sccm O<sub>2</sub>/CH<sub>4</sub>.

It is possible to deduce that the combustion-like flame transforms to the hybrid flame/discharge form as the microwave power exceeds the power produced by the combustion process. The combustion power of the flame for the set of data with a flow rate of 153/70 sccm O<sub>2</sub>/CH<sub>4</sub> is calculated as 44 W. The photographs in Figure 5.6 show that between 30 W and 40 W microwave power, the flame dramatically changes in appearance, to what resembles more closely a plasma than a flame. However, the combustion power for the second set of data (70/24 sccm O<sub>2</sub>/CH<sub>4</sub>) is ~ 16 W, but the flame does not transform at a microwave input power near this value.

It must also be noted that the torch is very sensitive to positioning/tuning. The “sweet spot” is dependent on several factors: 1) cavity height; 2) inner conductor position relative to outer conductor position; 3) outer conductor position inside cavity; 4) gas flow rate; and 5) microwave input power. Because all these factors must be considered, there are no exact measurements for factors 1, 2, and 3. The experimentalist has a feel and general idea of how each should be positioned; however, fine tuning is always required at the start of each experiment to find the sweet spot.

#### **5.4 Impact of microwaves on combustion**

To further show how microwaves impact a combustion flame, a flame extinction (or blow-out) plot is created and several OES scans of the flame/discharge are made.

Flame extinction plots are powerful for analyzing combustion efficiency in terms of fuel efficiency. An extinction plot is made to show that, with the addition

of microwaves, a flame is maintained burning less fuel than is required when no microwaves are present. Figure 5.10 is an extinction plot of experimental data showing this very effect. The figure plots the equivalence ratio versus total volumetric flow rate. The equivalence ratio,  $\phi$ , is a combustion term, defined as  $\phi = (V_F/V_{Ox})/(V_F/V_{Ox})_{Stoich}$ , where  $V$  is the volumetric flow rate in sccm;  $\phi = 1$  is the case for stoichiometric flow,  $\phi > 1$  represents fuel-rich flow, and  $\phi < 1$  represents fuel-lean flow, the range plotted in Figure 5.10. The figure includes values of combustion power for each gas flow rate.

The data is collected by first creating a stoichiometric flame, lowering the fuel slowly (considering delay of MFC responses) until the flame blows out, and then recording the flow rates at the point of extinction. The data points in the figure are the values of total flow rates at the point where the fuel flow rate causes flame extinction, while holding  $O_2$  flow constant. The equivalence ratio is calculated based on the fuel flow rate when blow out happens. The experiment is run several times to ensure accuracy of results; accuracy ranges from  $\pm 1$  sccm.

Three extinction curves are plotted: 1) combustion-only data; 2) hybrid data with 10 W microwave power; and 3) hybrid data with 20 – 100 W microwave power. With the addition of a minimal amount of microwaves (10 W), the flame continues to burn at a lower fuel flow, a flow that is not possible without the presence of microwaves. The average fuel flow rate reduction is 9%, ranging from 5 - 12%, not including the first data point in the first two curves. The sweet spot cannot be (easily) located at such a low flow rate; as a result, the microwaves do not affect the blow-out curve. At 10 W microwave power, the

flame/discharge does not completely transform in size and color as seen in previous data. Although no physical alterations are evident, the flame is affected by microwaves.

When 20 - 100 W of microwave power is added to the flame, a physical transformation takes place and a “discharge” is maintained with no fuel present. The third curve in Figure 5.10 reflects this behavior.

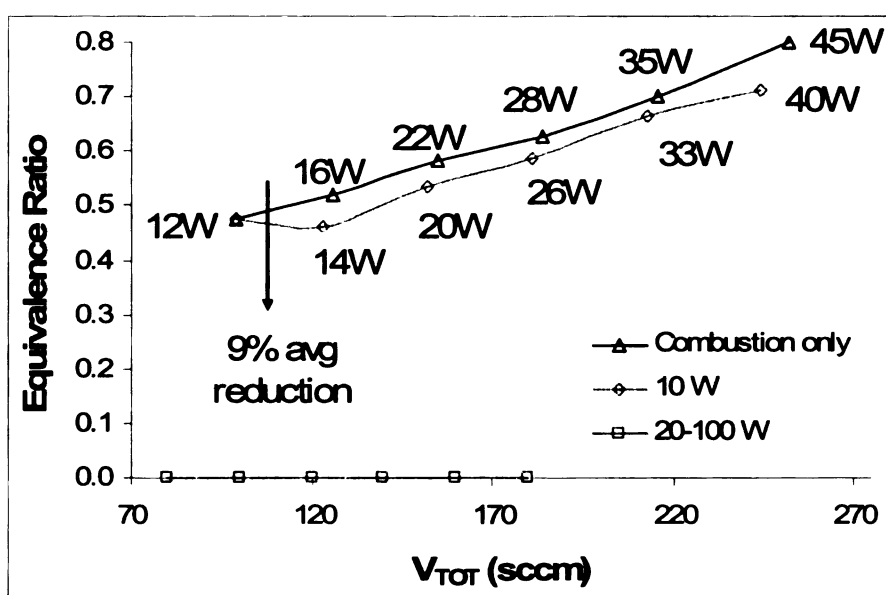


Figure 5.10 Flame extinction or blow-out plot of equivalence ratio versus total volumetric flow rate,  $V_{TOT}$ . Each data point is provided with the combustion power of the flame at a particular flow rate, where fuel is present. Note that a discharge is maintained with no fuel when 20-100 W of microwave power is added. A spreadsheet of raw data can be seen in Appendix B.

#### 5.4.1 Optical emission spectroscopy (OES)

OES is used to detect species present in the flame/discharge, leading to gas temperature calculations, and is used as a tool to gain perspective on how microwaves affect a flame. The molecules/radicals scanned in this research include  $N_2$ ,  $C_2$ ,  $O_2$ ,  $OH$ , and  $CH$ , all commonly found in hydrocarbon combustion

processes. The OES equipment used in this research is not capable of measuring quantitative values of intensity inferring the amount of CH, for example, present (arbitrary units, a.u., are labeled in plots; the scale could be labeled as current rather than intensity); however, relative intensities provide insight.

Photographs in Figures 5.4 and 5.5 in 5.2 show that a combustion flame formed by a ceramic nozzle is not physically altered by the presence of microwaves. OES analysis provides evidence that the flame may in fact be altered. Figure 5.11 is a plot of C<sub>2</sub> emission spectra, detected in a combustion-only flame and also in a hybrid flame/discharge with 40 W microwave power. All variables but microwave power are held constant. After 40 W microwave power is added to the flame, the C<sub>2</sub> emission intensity increases. Figure 5.24 in this section supports these results. The plot provides wide-range spectra for a combustion flame and a hybrid flame/discharge. Again, the intensity is greater with the presence of microwaves, suggesting the microwaves excite these molecules/radicals at higher levels.

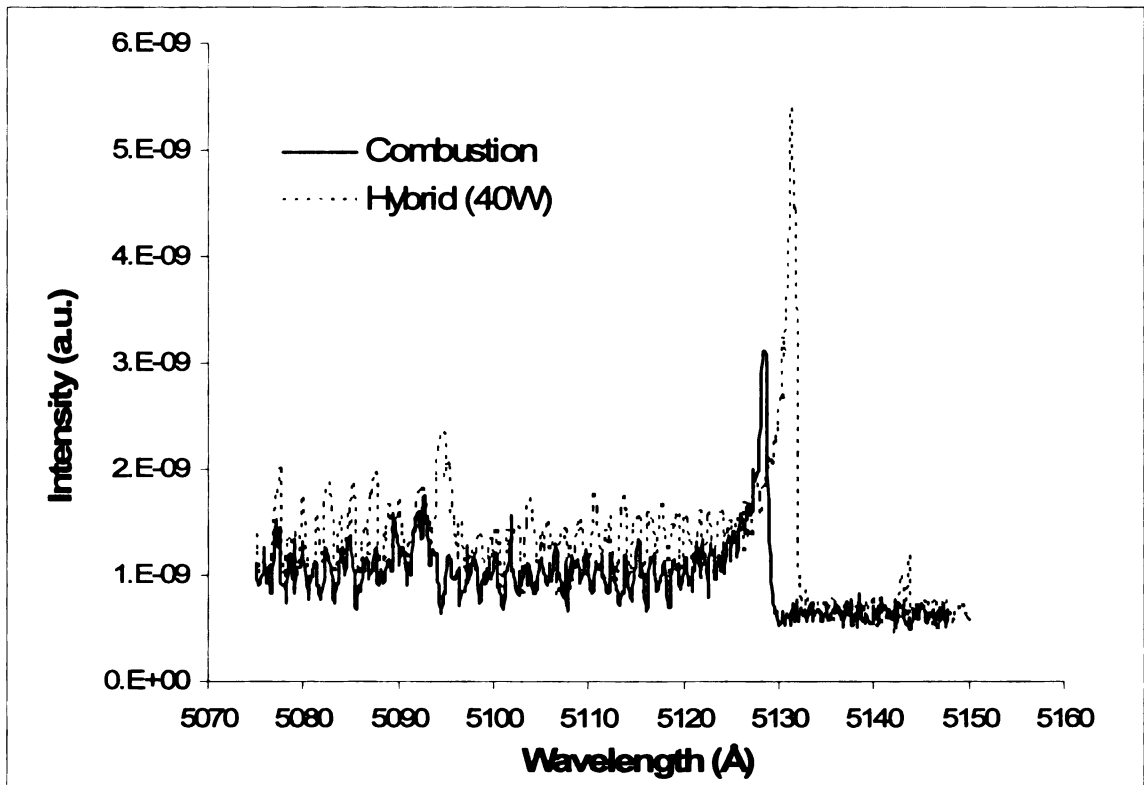


Figure 5.11 OES scan of C<sub>2</sub> in a stoichiometric (200/100 sccm O<sub>2</sub>/CH<sub>4</sub>) combustion flame and hybrid (combustion plus 40 W microwave power) discharge using a 0.4 mm-diameter *ceramic* nozzle.

The next set of plots, Figures 5.12 – 5.14, show N<sub>2</sub> emission spectra in combustion flames and hybrid flame/discharges. The general trend follows that as microwave power increases, N<sub>2</sub> emission intensity increases. Three independent sets of data are presented to show consistency within experimental results. Figure 5.14 shows intensities resulting from an N<sub>2</sub>-injection flame (N<sub>2</sub> is flowed into the gases upstream ignition). Peak intensities vary in all three experiments; this is probably caused by alterations in the experimental setup, i.e. the distance between the lens and flame may differ, or the torch may not be tuned exactly the same each time.

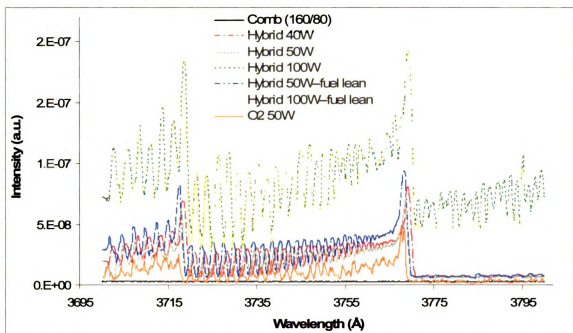


Figure 5.12 OES scan of N<sub>2</sub> in a stoichiometric (160/80 sccm O<sub>2</sub>/CH<sub>4</sub>) combustion flame and hybrid (combustion plus 40, 50, 100 W microwave power) discharge using the 0.4 mm-diameter brass nozzle. "Fuel lean" is a flow rate of 160/54 sccm O<sub>2</sub>/CH<sub>4</sub>. The last set of data is from a discharge of only 160 sccm O<sub>2</sub> and 50 W of microwave power (no fuel is present). Data from 30 W of microwave power and below show no N<sub>2</sub> signal, similar to the combustion-only case, and therefore are excluded from the plot.

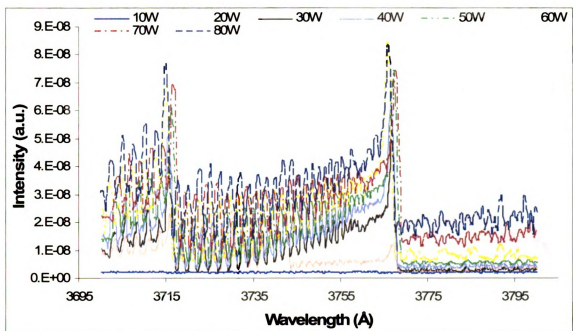


Figure 5.13 Second set of data: OES scan of  $N_2$  in a hybrid (160/80 sccm  $O_2/CH_4$  combustion plus 10-80 W microwave power) flame/discharge using the 0.4 mm-diameter brass nozzle.

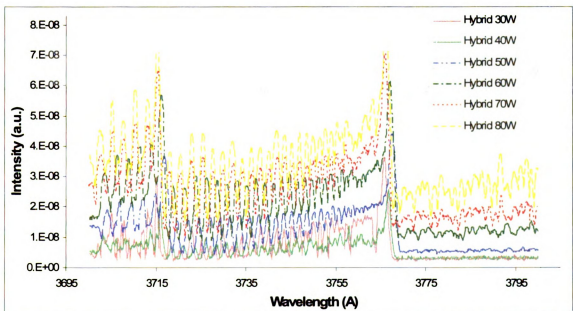


Figure 5.14 OES scan of  $N_2$  in a hybrid flame/discharge with a flow rate of 160/80/10 sccm  $O_2/CH_4/N_2$  with varying microwave power, 30-80 W. Note that  $N_2$  is injected upstream into the flow of gases,  $CH_4$  and  $O_2$ .

Figures 5.15 and 5.16 show  $C_2$  emission spectra in combustion flames and hybrid flame/discharges. The general trend follows that as microwave power increases,  $C_2$  emission intensity increases. Two sets of data are recorded to show consistency in experimental results.

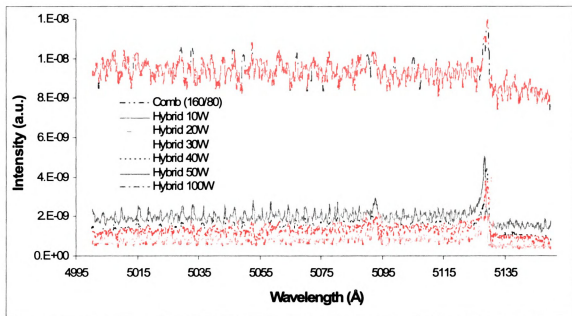


Figure 5.15 OES scan of  $C_2$  in a stoichiometric (160/80 sccm  $O_2/CH_4$ ) combustion flame and hybrid (combustion plus 10-100 W microwave power) discharge using the 0.4 mm-diameter brass nozzle. "Fuel lean" has a flow rate of 160/54 sccm  $O_2/CH_4$ .

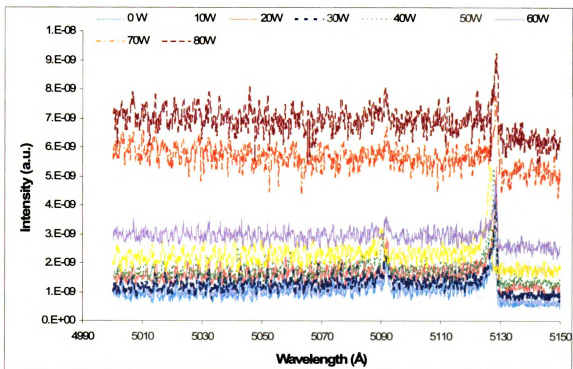


Figure 5.16 Second set of data: OES scan of C<sub>2</sub> in a combustion (160/80 sccm O<sub>2</sub>/CH<sub>4</sub>) and hybrid (combustion plus 10-80 W microwave power) flame/discharge using the 0.4 mm-diameter brass nozzle.

Emissions of O<sub>2</sub>, OH, and CH are also recorded in Figures 5.17 – 5.19. As seen for N<sub>2</sub> and C<sub>2</sub>, a general trend follows that as microwave power is added to a stoichiometric flame, the emission intensity increases.

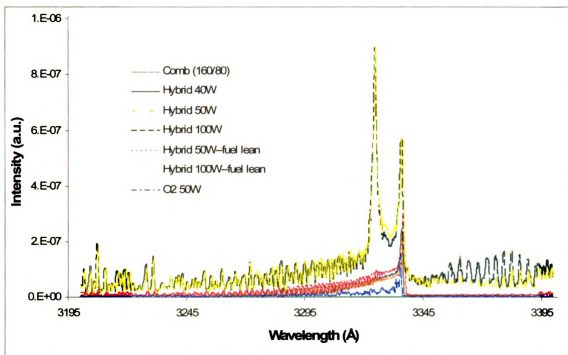


Figure 5.17 OES scan of O<sub>2</sub> in a stoichiometric (160/80 sccm O<sub>2</sub>/CH<sub>4</sub>) combustion flame and hybrid (combustion plus 40, 50, 100 W microwave power) discharge using the 0.4 mm-diameter brass nozzle. “Fuel lean” is a flow rate of 160/54 sccm O<sub>2</sub>/CH<sub>4</sub>. The last set of data is from a discharge of only 160 sccm O<sub>2</sub> and 50 W of microwave power (no fuel is present). Data from 30 W of microwave power and below show no O<sub>2</sub> signal, similar to the combustion-only case, and therefore are excluded from the plot.

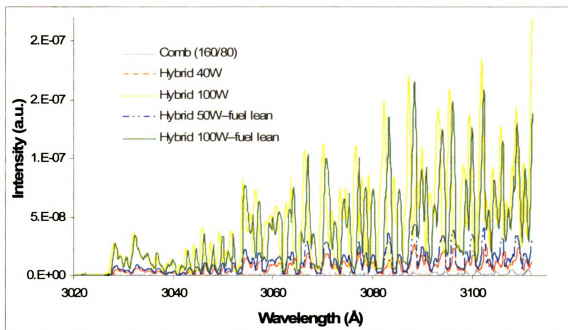


Figure 5.18 OES scan of OH in a stoichiometric (160/80 sccm  $O_2/CH_4$ ) combustion flame and hybrid (combustion plus 40, 50, 100 W microwave power) discharge using the 0.4 mm-diameter brass nozzle. "Fuel lean" is a flow rate of 160/54 sccm  $O_2/CH_4$ . Data from 30 W of microwave power and below show no OH signal, similar to the combustion-only case, and therefore are excluded from the plot.

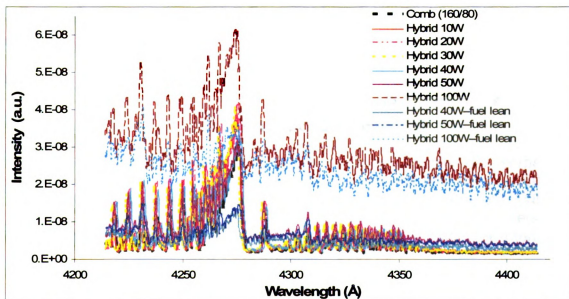


Figure 5.19 OES scan of CH in a stoichiometric (160/80 sccm  $O_2/CH_4$ ) combustion flame and hybrid (combustion plus 10-100 W microwave power) discharge using the 0.4 mm-diameter brass nozzle. "Fuel lean" is a flow rate of 160/54 sccm  $O_2/CH_4$ .

The peak intensities from each scan ( $N_2$ ,  $C_2$ ,  $O_2$ , and  $CH$ ) are plotted against absorbed microwave power. Figures 5.20 – 5.23 contain data from multiple sets of experiments, i.e. independent experiments, to show consistency within data. Aside from a scattering of data points due to variations in each independent experiment, the trend follows that intensity increases as microwave power increases.

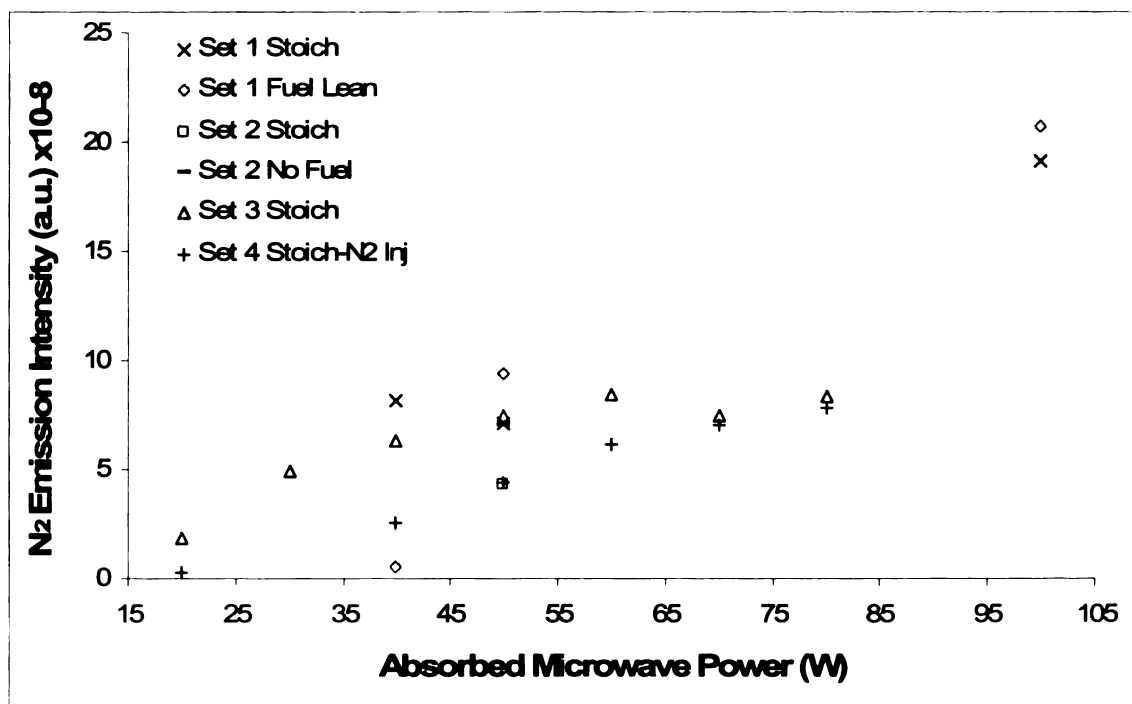


Figure 5.20 Relative intensities of  $N_2$  emissions as a function of absorbed microwave power, measured from flame/discharges with flow rates of 160/80 sccm, 160/54 sccm, and 160/0 sccm  $O_2/CH_4$ , and also a flow rate of 160/80/10 sccm  $O_2/CH_4/N_2$  with  $N_2$  injection. Intensities are recorded from four sets of experiments to show consistency, and values are recorded from peak intensities, at a wavelength of  $\sim 3769 \text{ \AA}$ .

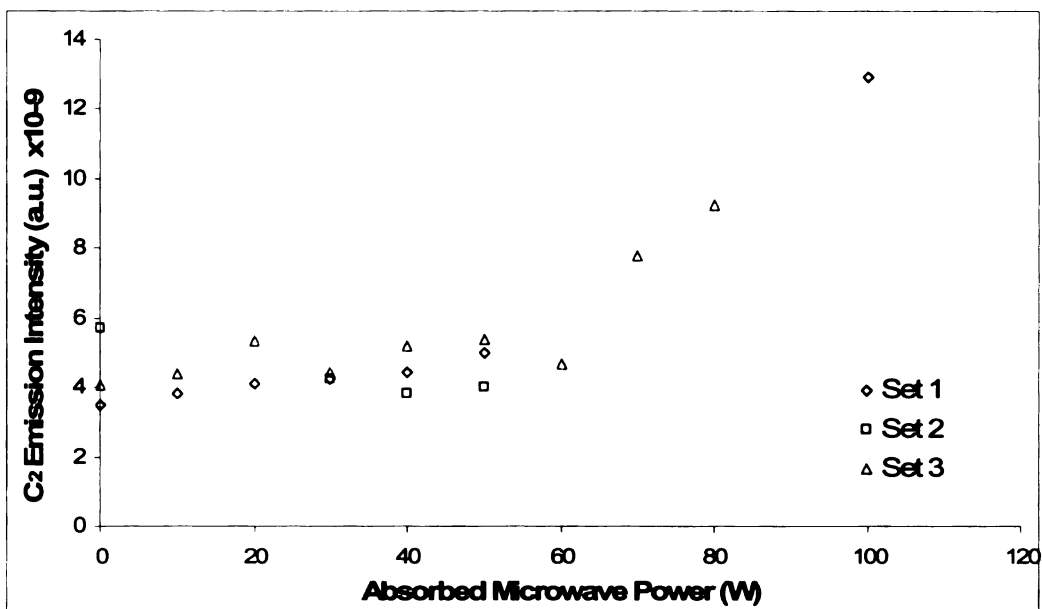


Figure 5.21 Relative intensities of C<sub>2</sub> emission as a function of absorbed microwave power, measured from a stoichiometric flame/discharge with a flow rate of 160/80 sccm O<sub>2</sub>/CH<sub>4</sub>. Intensities are recorded from three sets of experiments to show consistency, and values are recorded from peak intensities, at a wavelength of ~ 5130 Å.

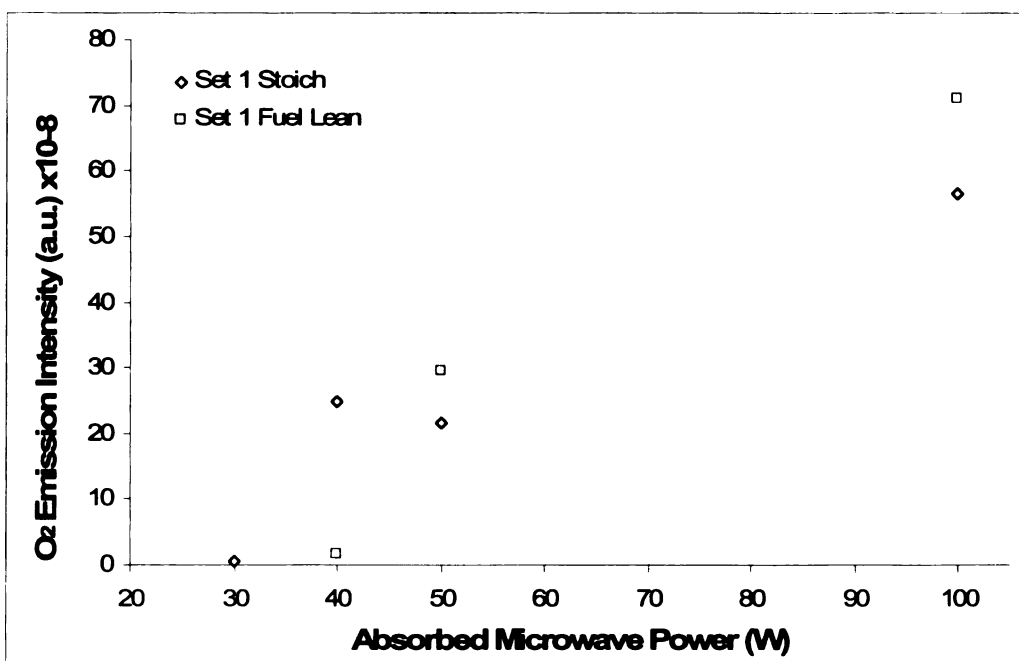


Figure 5.22 Relative intensities of O<sub>2</sub> emission as a function of absorbed microwave power, measured from flame/discharges with flow rates of 160/80 sccm O<sub>2</sub>/CH<sub>4</sub> and 160/54 sccm O<sub>2</sub>/CH<sub>4</sub>. Intensities are recorded from one set of experiments, and values are recorded from peak intensities, at a wavelength of ~ 3340 Å.

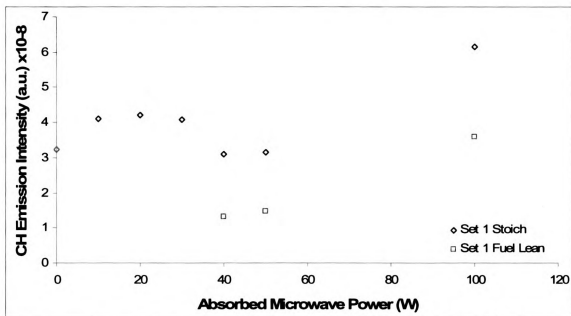


Figure 5.23 Relative intensities of CH emission as a function of absorbed microwave power, measured from flame/discharges with flow rates of 160/80 sccm O<sub>2</sub>/CH<sub>4</sub> and 160/54 sccm O<sub>2</sub>/CH<sub>4</sub>. Intensities are recorded from one set of experiments, and values are recorded from peak intensities, at a wavelength of ~4270 Å.

A wide-range scan including spectra of all species mentioned in this section is shown in Figure 5.24. The plot provides a clear, overall summary of how microwaves alter a combustion flame at a micro-scale level, not detectable by the human eye. The spectra of N<sub>2</sub> and C<sub>2</sub> are used to calculate gas temperatures which approximate flame/discharge temperatures, discussed in the next section.

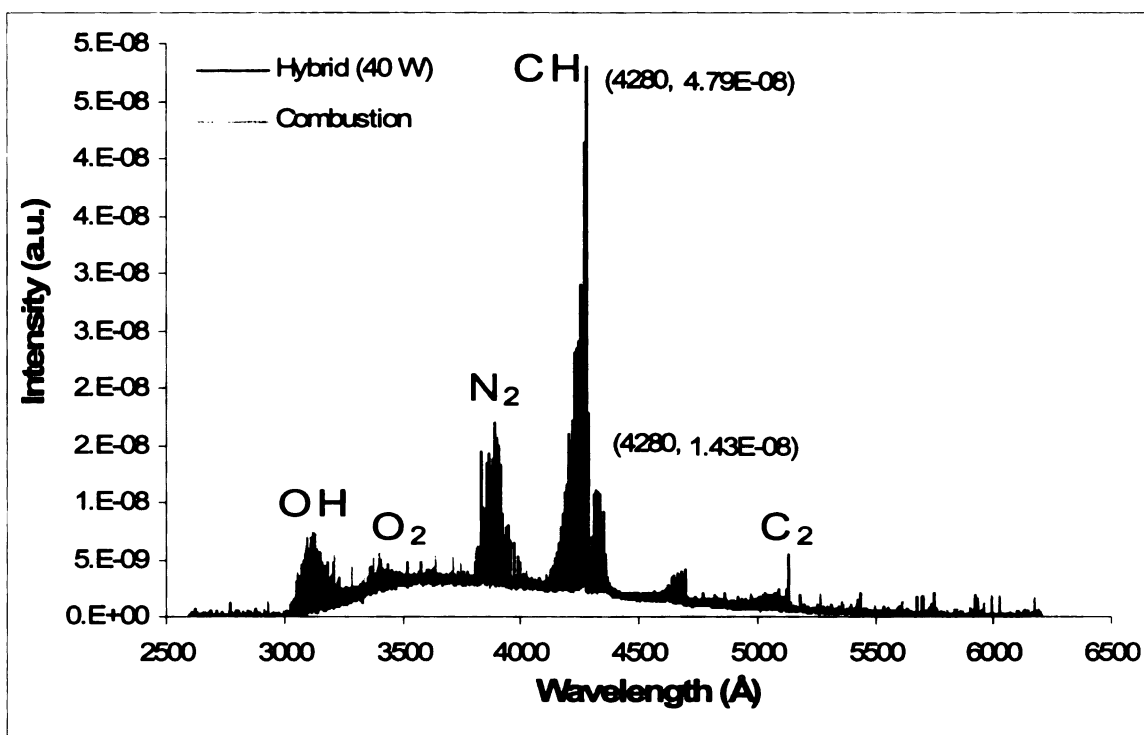


Figure 5.24 OES scan of combustion flame (160/80 sccm O<sub>2</sub>/CH<sub>4</sub>) and hybrid flame/discharge (addition of 40 W microwave power) for an entire range of visible emission spectra. The wavelength and relative intensities are given at the peak ( $\lambda = 4280 \text{ \AA}$ ) for each set of data. Molecules and radicals are listed next to their visible spectra. A 0.4 mm-diameter *ceramic* nozzle is used for this data.

### 5.5 Flame/discharge temperatures and profiles

Data for flame/discharge temperature are gathered with three different diagnostic techniques using: 1) a thermocouple; 2) OES; and 3) an IR camera. The experimental method for each technique is provided in Chapter 3.

As discussed previously, the thermocouple is capable of measuring a pure combustion flame temperature only because the metal interferes with the electrical field produced by microwaves. Figure 5.25 presents a temperature profile through the width of a stoichiometric flame, using a type K thermocouple. The photograph in the figure shows where the thermocouple collects data through the flame. From a time-step iterative algorithm, the maximum flame

temperature calculated is 2253 K. Adiabatic flame temperature for methane/oxygen flames, found in text [25], is approximately 3000 K. The theoretical curve drawn in Figure 5.25 is not plotted with theoretical data; it is a qualitative curve used for illustrative purposes. The 750 K difference in temperatures is most likely due, in majority, to heat loss. The thermocouple is not shielded, leading to radiation loss. Furthermore, the flame is not confined or insulated; much heat is lost to the environment. It is also important to mention that thermocouples are used to calculate point temperatures, whereas adiabatic flame temperatures tabulated are average temperatures of the entire flame.

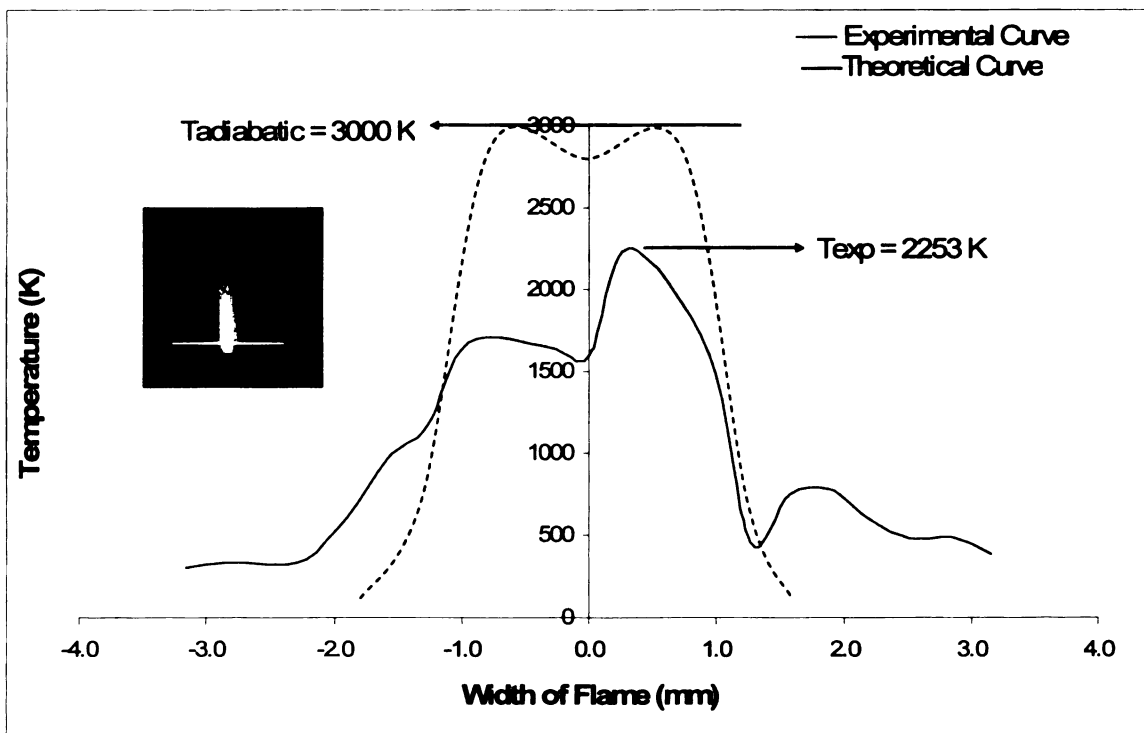


Figure 5.25 Temperature profile of a stoichiometric CH<sub>4</sub>/O<sub>2</sub> flame from a type K thermocouple. Photograph of the flame shows where the thermocouple scans the flame. The plot provides experimental data and also displays a qualitative example of a theoretical temperature distribution with an adiabatic flame temperature of 3000 K, taken as an average temperature.

Rotational temperatures of  $N_2$  and  $C_2$  are calculated for several sets of experiments, i.e. independent experiments. Figure 5.26 plots  $N_2$  rotational temperatures for three sets of stoichiometric flow rates. Note that  $N_2$  is added to the gas flow upstream the nozzle. It is shown that temperature remains constant for each stoichiometric flow rate, in agreement with theory. Possible outlier data in the plot is found at 70 W microwave power; the temperature spread is 652 K. Such a range may be caused by variations in the experimental setup, mainly tuning the torch to find the sweet spot. In addition, as the volume of the flame increases, so will the heat loss, causing a decrease in temperature. The temperature increases as microwave power increases,  $\sim 1200$  K from 30 W to 80 W.

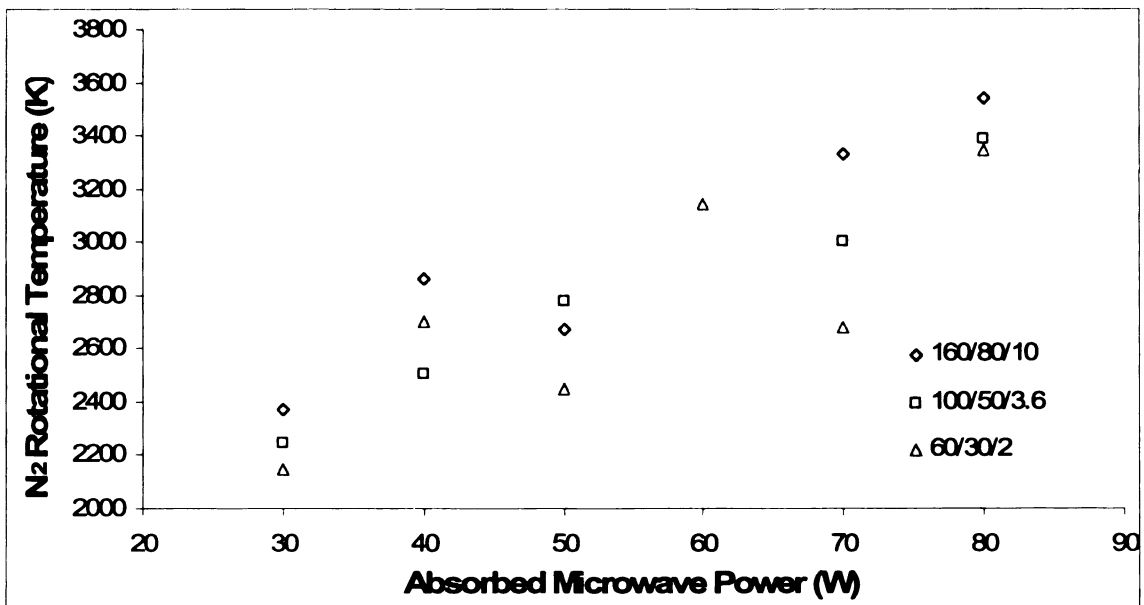


Figure 5.26  $N_2$  rotational temperature of a flame/discharge as a function of absorbed microwave power for data for three different flow rates: 160/80/10 sccm, 100/50/3.6 sccm, and 60/30/2 sccm  $O_2/CH_4/N_2$ .

Figure 5.27 graphs rotational temperatures of both  $N_2$  and  $C_2$  gases. Four independent experiments present data in this plot, the last set defined differently

because  $N_2$  is added to the gas flow. Data show a general increase in temperature as microwave power increases. The greatest increase occurs for  $N_2$  rotational temperatures (Set 1), with a temperature increase of 1489 K from 20 W to 80 W microwave power. The smallest increase occurs for  $C_2$  rotational temperature (Set 1), with a temperature increase of 95 K from 0 W to 80 W microwave power. Rotational temperatures of  $N_2$  and  $C_2$  in disagreement with each other does not infer that the temperature is miscalculated. Further investigation and research is required to know which rotational temperature, if either, best represents the flame temperature. Raw data from Figure 5.27 is listed in Appendix B.

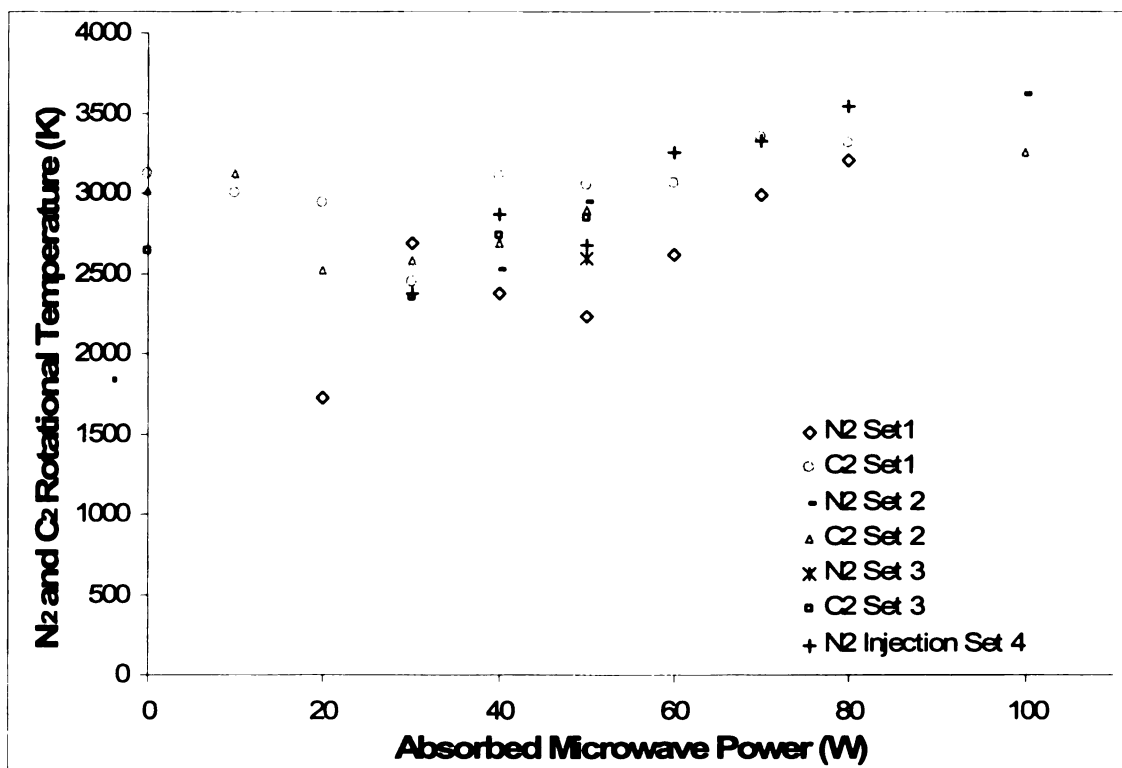


Figure 5.27  $N_2$  and  $C_2$  rotational temperatures of flame/discharges as a function of absorbed microwave power, for four sets of data (independent experiments). The flow rate for the first three sets is 160/80 sccm  $O_2/CH_4$ , and 160/80/10  $O_2/CH_4/N_2$  for the fourth set. Tables of raw data are found in Appendix B.

Flame and hybrid temperature greatly exceed those of pure plasma temperatures. Plasma temperatures measure  $\sim 1700$  K (measured from  $N_2$  gas temperatures) while combustion temperatures, measured by the same technique are close to double that.

### **5.5.1 Data collected from infrared (IR) camera**

Although quantitative temperatures cannot be measured with the IR camera at this time (another student's ongoing Ph.D. research), qualitative deductions are made. The images shown in Figure 5.28 are temperature profiles, created by the IR camera, of a stoichiometric flame as microwave power increases from 0 W to 40 W to 60 W. The emissivity is unity for all the results shown.

The flame analyzed in these images is not confined within the microwave cavity because the IR camera cannot bypass the metal screen in the cavity's windows. Therefore, the torch is not optimally tuned due to microwave leakage. Results do show, however, that the microwaves do indeed alter the flame. The center of the flame, the white temperature profile in Figure 5.28, is the hottest part of the flame, relative to all the profiles shown. As microwave power is added, this center section expands while the outermost sections contract. This behavior suggests that microwaves create a more intense flame/discharge by decreasing volume and increasing temperature. Figure 5.29 is a sketch of the first two IR images in Figure 5.28 against each other, to clearly show the change in volume.

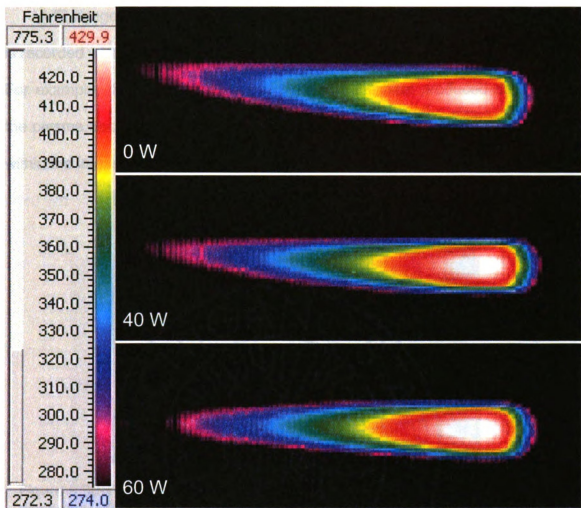


Figure 5.28 Temperature profile images from the IR camera of a flame as it is modified by microwave power, 40 W and 60 W. The flame is not confined within the cavity. The temperature scale is provided, but does not provide an accurate temperature reading. The gas flow rate is 200/100 sccm  $O_2/CH_4$ .

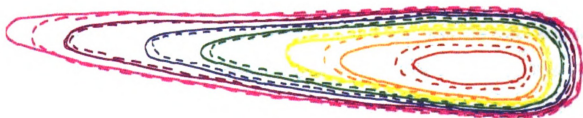


Figure 5.29 Temperature profiles sketched from the IR camera images (from Figure 5.28) for both a combustion flame (represented by the solid lines) and a hybrid flame/discharge with 40 W microwave power added (dashed lines).

IR images of a pure argon plasma are shown in Figure 5.30. Each image is recorded with a different filter, so as to highlight various sections of the plasma. For example, the bottom-right image highlights the heat produced downstream the plasma discharge, while the top-left image highlights the temperature profiles within the intense plasma itself.

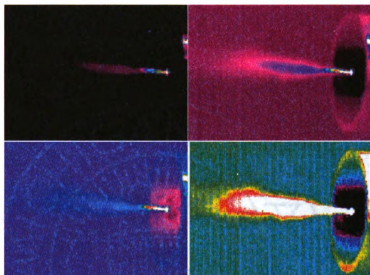


Figure 5.30 Temperature profile images from the IR camera for a plasma-only discharge: 200 sccm argon excited by 40 W microwave power. Each image is recorded with a different filter. The image in the bottom right corner shows the temperature profiles of the hot gases beyond the plasma.

Figure 5.31 shows IR images of a flame produced by a ceramic nozzle. An interesting observation is the temperature profiles of the ceramic. The center of the nozzle, where the flame sits, appears much hotter than the outer edges. Further study of ceramic temperature profiles should be carried out. This IR camera is capable of accurately measuring temperatures of solid surfaces, and it is also capable of recording time-dependent temperatures.

Time-dependent temperature measurements of a gold-sputtered ceramic nozzle are made with the IR camera. Unfortunately visual results of this experiment are not reported in this thesis because the only current recorded format is an avi file (video file). In summary, the gold-sputtered ceramic generates higher temperature profiles than the ceramic with no gold coating and does not cool down as fast as the ceramic with no coating.

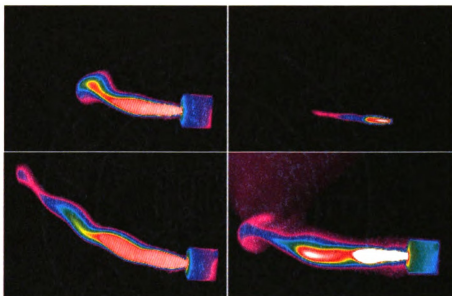


Figure 5.31 Temperature profile images from the IR camera for a stoichiometric combustion flame formed by a ceramic nozzle. Different camera filters are used to highlight different sections of the flame. The temperature profiles of the nozzle are also illustrated.

## **Chapter 6**

### **Summary and Recommendations**

#### **6.1 Summary of results**

An extensive experimental study of microwave plasma-enhanced combustion concludes that microwaves do in fact alter a combustion flame. Physical alterations of the flame are made in color and geometry, as color changes from a blue flame to a white/yellow hybrid discharge with the addition of microwaves, and flame lengths and diameters grow in size. Alterations at the micro-scale level are also made in flame species. Molecules and radicals detected in the flame/discharge become more intense, or more accelerated, by the presence of microwaves. In addition, temperatures increase with the addition of microwaves, as hypothesized.

One question that remains asks what exactly is desired by adding microwaves to a flame. Is it desirable to create a completely transformed flame that changes in color and increases in size, thus raising temperature but lowering power density; or is it more desirable to add just enough microwave power (10 – 30 W) so the power density rises exponentially without physically changing the appearance of the flame. The trade-off is temperature. More microwave power yields higher flame temperatures.

These questions may be more easily answered when considering the applications of such a hybrid technology. Industry may be interested in a small-scale, easily handled, clean torch used for welding, surface treatment, or localized heating. In these cases, a higher-temperature flame/discharge is

desired. When considering cutting comparable to laser technology, geometry is a major factor considered. The more concentrated and more intense the discharge is, the more precise the cut will be. Geometry also becomes a critical factor when considering medical applications, such as surgery.

Other applications include engines, both jet engines and automotive engines. Results in this thesis show that, with the presence of microwaves, a flame is maintained with lower fuel consumption than would be possible without microwaves. Fuel-efficient engines are driving the automotive industry today. Both higher temperatures and larger geometries may be desired for this application.

Motivation behind this research includes improving the combustion process by creating more efficient combustion with the addition of microwaves. Results support the hypothesis that microwaves do improve the combustion process. Flame stability and fuel-efficient combustion are enhanced in this hybrid system. It is yet to be shown in this research if cleaner combustion results from the addition of microwaves. Researchers at the Los Alamos National Laboratory have shown that a slightly different plasma-enhanced hybrid system increases combustion efficiency by reducing the amount of unburned hydrocarbon (propane) emissions and also reduces toxic  $\text{NO}_x/\text{SO}_x$  emissions [1].

It appears that the presence of microwaves accelerates the combustion reaction, reflected in flame velocities calculated from measured flame angles. Flame speed more than doubles with the addition of microwaves when the physical transformation takes place.

## 6.2 Recommendations

Further investigation and study of the ceramic nozzle is encouraged. In terms of manufacturing, an improved method for attaching the ceramic nozzle to the brass inner conductor should be sought. Currently the nozzle is glued with epoxy to the inner conductor. This becomes a problem when microwaves are present. The electrical energy is drawn to this epoxy material, thus retracting from the flame itself. Additional temperature measurements made with the IR camera could provide insight as to whether the ceramic is or is not absorbing microwaves.

An improved design of the microwave cavity would attract the torch to industry. The cavity is big and bulky. Designing a much smaller and compact cavity to allow an intense formation of an electric field is critical. Temperature measurements of the flame/discharge inside the cavity using the IR camera would also provide insight for what is happening to temperature as microwaves greatly transform the flame.

If time and funds allow, more detailed diagnostic measurements should be made including cavity ring-down spectroscopy (CRDS) and laser-induced fluorescence (LIF) to determine the influence of plasma enhancement on the distributions of CH, C<sub>2</sub> and OH. OES used for the research in this thesis provides profitable results in terms of qualitative analysis. For quantitative analysis, however, the suggested CRDS and LIF techniques are preferred.

CRDS is an absorption technique where pulsed laser light is coupled into an optical cavity formed by highly reflecting mirrors. It is a sensitive

technique because the optical path length is made long by the highly reflecting mirrors, and it is convenient because the quantity being measured is the decay time of the light intensity, not the absolute intensity of the light as needed for direct absorption spectroscopy measurements. CRDS works at both atmospheric pressure and low pressures (5 – 30 Torr), suggested working conditions for future experimental work. LIF is a high-spatial-resolution technique but can be more difficult to calibrate and work with.

One final suggestion considers a numerical study. A computational simulation can be created by factoring into a full flame chemistry simulation the electronic or plasma reaction component. Full flame chemistry simulations are developed and available as commercial software. The suggested hybrid simulation has yet to be fully developed. Such a simulation would provide validation for experimental results and provide a deeper understanding of the research.

## **APPENDICES**

## Appendix A

Table A.1 Values for thermocouple temperature measurements.

Time Step	Width of Flame (mm)	Measured T(t) (degC)	Measured Previous T (degC)	$\rho_{solid}$ (kg/m <sup>3</sup> )	$c_{p_{solid@20C}}$ (J/kg-K)	$\mu$ (N-s/m <sup>2</sup> )	$\mu_s$ (N-s/m <sup>2</sup> )
1	-3.158	24.4		8600	523	2.00E-05	2.00E-05
2	-2.842	26.5	24.4	8600	523	2.02E-05	2.02E-05
3	-2.526	28	26.5	8600	523	2.22E-05	2.03E-05
4	-2.211	31.1	28	8600	523	2.16E-05	2.05E-05
5	-1.895	51.6	31.1	8600	523	2.33E-05	2.18E-05
6	-1.579	101.2	51.6	8600	523	3.48E-05	2.45E-05
7	-1.263	167.4	101.2	8600	523	4.64E-05	2.75E-05
8	-0.947	274.2	167.4	8600	523	5.26E-05	3.23E-05
9	-0.316	382.9	274.2	8600	523	6.70E-05	3.62E-05
10	0.000	473.8	382.9	8600	523	6.62E-05	3.91E-05
11	0.316	615.7	473.8	8600	523	6.46E-05	4.37E-05
13	0.947	1297.6	1285.9	8600	523	2.18E-04	6.40E-05
14	1.263	1196.2	1297.6	8600	523	6.51E-05	6.11E-05
15	1.579	1096.2	1196.2	8600	523	2.81E-05	5.83E-05
16	1.895	985.2	1096.2	8600	523	3.93E-05	5.51E-05
17	2.211	893.2	985.2	8600	523	4.03E-05	5.24E-05
18	2.526	818.5	893.2	8600	523	3.43E-05	5.03E-05
19	2.842	753.3	818.5	8600	523	2.93E-05	4.82E-05
20	3.158	712.5	753.3	8600	523	2.97E-05	4.68E-05
$\mu/\mu_s$	$k_{fluid-O_2}$ (W/m-K)	Pr	$v_{fluid}$ (m <sup>2</sup> /s)	Re	h (W/m <sup>2</sup> K)	Calculated T-flame (degC)	Calculated T-flame (K)
1.000	0.02532	0.74036	1.61E-05	375.15 5	170.31	27.00	300.00
1.002	0.02553	0.74000	1.74E-05	348.54	166.14	58.25	331.25
1.094	0.02807	0.73563	1.98E-05	306.07	175.16	49.47	322.47
1.056	0.02736	0.73685	1.91E-05	316.92	172.25	76.25	349.25
1.071	0.02954	0.73311	2.12E-05	285.99	177.89	340.37	613.37
1.423	0.04968	0.70553	5.65E-05	107.11	207.29	697.37	970.37
1.688	0.06884	0.72788	1.21E-04	50.01	225.12	897.52	1170.52
1.626	0.08008	0.73307	1.65E-04	36.62	234.90	1400.86	1673.86
1.852	0.11066	0.71217	3.14E-04	19.29	270.49	1371.83	1644.83
1.691	0.10889	0.71338	3.05E-04	19.83	265.17	1318.27	1591.27
1.478	0.10564	0.71560	2.89E-04	20.91	256.70	1979.69	2252.69
1.312	0.14582	0.68814	4.85E-04	12.49	303.49	6685.03	6958.03
3.411	0.43163	0.49279	1.87E-03	3.23	716.22	1334.39	1607.39
1.065	0.10662	0.71493	2.94E-04	20.57	247.25	182.38	455.38
0.483	0.03806	0.71882	3.45E-05	175.70	159.48	480.65	753.65
0.714	0.05721	0.71431	8.19E-05	73.94	185.62	511.00	784.00
0.769	0.05884	0.71621	8.74E-05	69.30	189.02	323.78	596.78
0.682	0.04879	0.70449	5.35E-05	113.11	182.42	206.73	479.73
0.607	0.04002	0.71555	3.75E-05	161.38	168.80	216.29	489.29
0.634	0.04079	0.71426	3.87E-05	156.38	171.15	114.35	387.35

## Appendix B

Table B.1 Values used for flame extinction plot in Chapter 5.

<b>Combustion Only (0.4 mm brass)</b>		<b>Combustion+Microwaves</b>		
<b>Blowout</b>		<b>10 W</b>	<b>20-100 W</b>	
<b>V<sub>O2</sub> (sccm)</b>	<b>V<sub>CH4</sub> (sccm)</b>	<b>V<sub>CH4</sub> (sccm)</b>	<b>V<sub>CH4</sub> (sccm)</b>	<b>% Fuel Reduction</b>
180	72	64	0	11
160	56	53	0	5
140	44	41	0	7
120	35	32	0	9
100	26	23	0	12
80	19	19	0	0

<b>Combustion Only (brass, 0.4)</b>		<b>Combustion+10W</b>		<b>Combustion+20-100W</b>	
<b>Equivalence Ratio</b>	<b>V<sub>TOT</sub> (sccm)</b>	<b>Equivalence Ratio</b>	<b>V<sub>TOT</sub> (sccm)</b>	<b>Equivalence Ratio</b>	<b>V<sub>TOT</sub> (sccm)</b>
0.80	252	0.71	244	0.00	180
0.70	216	0.66	213	0.00	160
0.63	184	0.59	181	0.00	140
0.58	155	0.53	152	0.00	120
0.52	126	0.46	123	0.00	100
0.48	99	0.48	99	0.00	80

Table B.2 Values found in temperature plots in Chapter 5.

<b>Methane/Oxygen Mixture (160/80 sccm), Set 1</b>									
<b>Microwave Power (W)</b>	0	10	20	30	40	50	60	70	80
<b>Rotational Temperature (K) N2</b>	N/A	N/A	1717	2682	2368	2223	2609	2991	3206
<b>Rotational Temperature (K) C2</b>	3124	2994	2935	2441	3111	3049	3057	3350	3318

<b>Methane/Oxygen Mixture (160/80 sccm), Set 2</b>							
<b>Microwave Power (W)</b>	0	10	20	30	40	50	100
<b>Rotational Temperature (K) N2</b>	N/A	N/A	N/A	N/A	2524	2934	3612
<b>Rotational Temperature (K) C2</b>	3016	3115	2516	2584	2687	2886	3254

<b>Methane/Oxygen Mixture (160/80 sccm), Set 3</b>				
<b>Microwave Power (W)</b>	<b>0</b>	<b>30</b>	<b>40</b>	<b>50</b>
<b>Rotational Temperature (K) N2</b>	N/A	N/A	N/A	2589
<b>Rotational Temperature (K) C2</b>	2637	2352	2738	2849

<b>Methane/Oxygen Mixture (160/80/10 sccm), Set 4</b>						
<b>Microwave Power (W)</b>	<b>30</b>	<b>40</b>	<b>50</b>	<b>60</b>	<b>70</b>	<b>80</b>
<b>Rotational Temperature (K) N2</b>	2368	2863	2674	3258	3329	3542

## BIBLIOGRAPHY

- [1] L. A. Rosocha, Y. Kim, S. Stange, V. Ferreri, D. M. Coates, and D. Platts, "Plasma-enhanced combustion of propane using a silent discharge," *Plasma Physics Research Highlights*, Los Alamos National Laboratory.
- [2] N. Chintala, R. Meyer, A. Hicks, B. Bystricky, J. W. Rich, W. R. Lempert, and I. V. Adamovich, "Non-thermal ignition of premixed hydrocarbon-air and CO-air flows by nonequilibrium RF plasma," *42<sup>nd</sup> AIAA Aerospace Sciences Meeting and Exhibit*, Reno, NV, 2004.
- [3] K. W. Hemawan, C. L. Romel, S. Zuo, I. S. Wichman, T. A. Grotjohn, J. Asmussen, "Microwave plasma-assisted premixed flame combustion," *International Workshop on Micro-plasma*, Greifswald, Germany, 2005.
- [4] S. Whitehair, L. L. Frasch, and J. Asmussen, "Experimental performance of a microwave electrothermal thruster with high temperature nozzle materials," *19<sup>th</sup> AIAA/DGLR/JSASS International Electric Propulsion Conference*, Colorado Springs, CO, 1987.
- [5] A. Yu. Starikovskii, "Plasma supported combustion," *30<sup>th</sup> International Symposium on Combustion*, Chicago, IL, 2004.
- [6] S. M. Starikovskaia, I. N. Kosarev, A. V. Krasnochub, E. I. Mintoussov, A. Yu. Starikovskii, "Control of combustion and ignition of hydrocarbon-containing mixtures by nanosecond pulsed discharges," *43<sup>rd</sup> AIAA Aerospace Sciences Meeting and Exhibit*, Reno, NV, 2005.
- [7] J. W. Dold, R. W. Thatcher, A. Omon-Arancibia, and J. Redman, "From One-Step to Chain-Branching Premixed Flame Asymptotics," *Combustion Institute*, 29:1519-1526 (2002).
- [8] N. Peters, *Turbulent Combustion*, Cambridge University Press, 2000.
- [9] A. Linan and F. A. Williams, *Fundamental Aspects of Combustion*, Oxford University Press, New York, 1993.
- [10] J. Buckmaster, *Annu. Rev. Fluid Mech.* 25:21-53 (1993).
- [11] P. Pelce, *Dynamics of Curved Fronts*, Academic Press, London, 1988.
- [12] G. I. Sivashinsky, *Annu. Rev. Fluid Mech.* 15:179-199 (1983).
- [13] F. A. Williams, *Combustion Theory*, Benjamin/Cummings, San Francisco, 1985.

- [14] J. D. Buckmaster and G. S. S. Ludford, *Theory of Laminar Flames*, Cambridge University Press, 1982.
- [15] Ya. B. Zeldovich, G. I. Barrenblatt, V. B. Librovich, and G. M. Makhviladze, *The Mathematical Theory of Combustion and Explosions*, Consultants Bureau, New York, 1985.
- [16] I. K. Puri, *Environmental Implications of Combustion Processes*, CRC Press, Boca Raton, Florida, 1993, Chapter 5 by I. S. Wichman.
- [17] S. Zuo, K. Hemawan, J. J. Narendra, T. A. Grotjohn, and J. Asmussen, "Miniature microwave plasma torch applicator and its characteristics," *IEEE Conference on Plasma Science*, 5A3, 2004.
- [18] K. W. Hemawan, Numerical Analysis and Experimental Measurements of Material Loading in Cylindrical Microwave Cavity Applicators, M.S. Thesis, Michigan State University, 2003.
- [19] K. W. Hemawan, S. Zuo, C.L. Romel, T. A. Grotjohn, I. S. Wichman, E. Case, and J. Asmussen, "Exploring microwave plasma-assisted combustion," *International Conference on Plasma Systems (ICOPS)*, Monterey, CA, 2005.
- [20] J. B. Wachtman, Jr., Mechanical Properties of Ceramics, John Wiley and Sons, Inc., New York, 1996.
- [21] J. Zhang, L. Liu, T. Ma, and X. Deng, "Rotational temperature of nitrogen glow discharge obtained by optical emission spectroscopy," *Spectrochim. Acta A*, 58, 1915-1922, 2002.
- [22] J. J. Narendra, Characteristics and Modeling of Miniature Microwave Plasma Discharge Created with Microstripline Technology, M.S. Thesis, Michigan State University, 2004.
- [23] E. Stoffels, A. J. Flikweert, W. W. Stoffels, And G. M. W. Kroesen, "Plasma needle: a non-destructive atmospheric plasma source for fine surface treatment of (bio) materials," *Plasma Sources Sci. Technol.*, 11, 383-388, 2002.
- [24] W. Huang, Microwave Plasma Assisted Chemical Vapor Deposition of Ultrananocrystalline Diamond Films, Ph.D. Dissertation, Michigan State University, 2004.
- [25] F. P. Incropera and D. P. Dewitt, Introduction to Heat Transfer, John Wiley and Sons, New York, 2002.

[26] J. L. Short, A New System Developed to Characterize Thermoelectric Devices for Power Generation Applications, M.S. Thesis, Michigan State University, 2005.

[27] G. Herzberg, Molecular Spectra and Molecular Structure. I. Spectra of Diatomic Molecules, D. Van Nostrand Co., Inc., Princeton, 1950.

[28] S. N. Suchard and J. E. Melzer, Spectroscopic Data 2: Homonuclear Diatomic Molecules, IFI/Plenum, New York, 1976.

[29] G. L. King, Temperature and Concentration of Ionic and Neutral Species in Resonant Microwave Cavity Plasma Discharges, Ph.D. Dissertation, Michigan State University, 1994.

[30] B. C. Wadell, Transmission Line Design Handbook, Artech House, Inc., Norwood, 1991.

[31] S. R. Turns, An Introduction to Combustion, The McGraw-Hill Companies, Inc., Boston, 2000.

MICHIGAN STATE UNIVERSITY LIBRARIES



3 1293 02736 8749